# Investigation of Azimuthal Asymmetries in Charged and Strange Particle Distributions from CERES

**Jovan Milošević**

**Physikalisches Institut der Universität Heidelberg**

**2005**

**Dissertation**
**submitted to the**
**Combined Faculties for the Natural Sciences and for Mathematics**
**of the Ruperto-Carola University of Heidelberg, Germany**
**for the degree of**
**Doctor of Natural Sciences**

**presented by**

**MSc in physics Jovan Milošević**

**born in Vršac, Serbia**

**Oral Examination: 14.02.2006**

# Investigation of Azimuthal Asymmetries in Charged and Strange Particle Distributions from CERES

**Referees:** **Prof. Dr. Johanna Stachel**

**Prof. Dr. Norbert Herrmann**

Diese Doktorarbeit stellt die Messung des anisotropen transversalen Flusses $v_2$ geladener und seltsamer Teilchen mit dem CERES Spektrometer vor. Gezeigt werden die elliptischen Fluss Messungen der Teilchen $\Lambda$, $K_S^0$, $\pi^\pm$ und $p$ in Pb-Au Kollisionen bei höchsten SPS Energien. Mit einem Pseudorapiditätsbereich von $\eta = 2.05 - 2.70$ bei voller azimuthaler Akzeptanz und mit einer $p_T$ Sensitivität von bis zu 4 GeV/c können mit den CERES Daten hydrodynamische Modelle getestet werden. $v_2$ wird als Funktion der Zentralität, Rapidität, Pseudorapidität und des Transversalimpulses für die verschiedenen Teilchensorten diskutiert. Die Messungen werden mit Ergebnissen des NA49 Experimentes und mit hydrodynamischen Rechnungen verglichen. Ferner werden Vergleiche zu den STAR und RHICH Beobachtungen angestellt. Bei kleinem $p_T$ wird der Massenordnungseffekt $v_2(\Lambda) < v_2(K_S^0) < v_2(\pi^\pm)$ beobachtet. Ein entgegengesetztes Verhalten zeigt sich bei hohem $p_T$. Um ein tieferes Verständniss für die Ursachen des Skalenverhaltens des kollektiven Flusses mit der Anzahl an Konstituentenquarks und mit der transversalen Rapidität zu erhalten, wird die von der Hydrodynamik vorhergesagte $y_T^{f_s}$-Skalierung durchgeführt. Vergleiche differentieller Flussmessungen verschiedenster Teilchen mit verschiedenen Szenarien an Skalenverhalten ermöglicht eine Aussage über die Ursachen des Flusses, sowie über die frühesten Stadien der Kollision.

In this thesis the anisotropic transverse flow $v_2$ of charged and strange particle species measured by the CERES experiment is investigated. The $\Lambda$, $K_S^0$, $\pi^\pm$ and proton elliptic flow measurements from Pb+Au collisions at the highest SPS energy are presented. The data, collected by the CERES experiment which covers $\eta = 2.05 - 2.70$ with full $2\pi$ azimuthal acceptance and $p_T$ sensitivity up to 4 GeV/c, is used to test hydrodynamical models. The value of $v_2$ as a function of centrality, rapidity, pseudorapidity and $p_T$ is presented for different particle species. The obtained measurements are compared with results from the NA49 experiment and with hydrodynamical calculations. Also the results are compared with $v_2$ values observed with STAR at RHIC. The mass ordering effect was observed: $v_2(\Lambda) < v_2(K_S^0) < v_2(\pi^\pm)$ at small $p_T$, while at high $p_T$ it is opposite. In order to get better insight into the origin of the collective flow scaling to the number of the constituent quarks and the transverse rapidity $y_T^{fs}$ scaling predicted by hydrodynamics were performed. Testing the differential flow measurements of different particle species against different scaling scenarios may yield additional information about the origin of flow as well as about the early stage of the collision.

# Acknowledgments

To my son and wife, to my parents, to my brother and his family for their love and support that keeps me going.

To all my professors at the Physikalisches Institut in Heidelberg, at the Institute of Physics and the Faculty of Physics in Belgrade; thank you for teaching me so much and for making me realize there is so much more to learn.

I am grateful to Ana Marín who was willing to read my thesis and to give useful remarks in order to make it better. Also I would like to thank to Wilrid Ludolphs who provided me a code for the secondary vertex reconstruction which was used in the $K_S^0$ elliptic flow analysis.

And thank to my friends here at the Physikalisches Institut and at the Gesellschaft für Schwerionenforschung who were helping me to finish this thesis.

# Contents

# List of Figures

# List of Tables

# Chapter 1

# INTRODUCTION

## 1.1 Quark-Gluon Plasma

The experimental study of nuclear matter exposed to extremely high temperatures and densities offers a unique opportunity for obtaining information concerning strongly interacting many-body systems. Most important is the searching for the predicted phase transition to Quark-Gluon-Plasma (QGP) [7]. QGP is defined as a (locally) thermally equilibrated state of matter in which quarks and gluons are deconfined from hadrons, so that color degrees of freedom become manifest over nuclear, rather than merely nucleonic, volumes. In nature, a transition from QGP to hadronic matter has probably undergone $10^{-6} - 10^{-5}$ s after Big Bang [8, 9]. Now, the above mentioned systems probably exist in astrophysical objects, like neutron stars and collapsing supernovae [10–12]. In that new state of matter the chiral symmetry is restored. From all written above it is clear that the study of the QGP is of common interest to particle and nuclear physics, as well as for astrophysics and cosmology.

## 1.2 Experimental Search for the QGP

In the laboratory, strongly interacting many-body systems at extreme conditions can be produced and investigated using heavy-ion collisions at high colliding energies. Due to that such collisions are investigated already three decades. To study in a systematic way systems created in such collisions many experiments were designed and built. It started with accelerating of relatively light projectiles as He, C, Ne up to Ar at BEVALAC in Berkeley, the USA, and in the USSR started to work the LHE synchrophasotron in the Laboratory for High Energies at the Joint Institute for Nuclear Research (JINR) in Dubna. These experiments continued in the eighties with accelerating of heavier nuclei with the SchwerIonen-Synchrotron (SIS) at the Gesellschaft für Schwerionenforschung (GSI) in Darmstadt (Germany) and the Alternating Gradient Synchrotron (AGS) in the Brookhaven National Laboratory (BNL) in the USA. At CERN (the acronym of *Conseil Européen pour la Recherche Nucléaire*) the Super Proton Synchrotron (SPS) was built. They were operating with an incident energy from several hundreds MeV/c (at BEVALAC) up to 200 GeV/c per nucleon (at SPS). Since that time many experiments used these facilities in investigations of the above mentioned physical systems. At incident energies between 1 and 200 GeV/c temperatures between 50 and 160 MeV are achieved and baryon densities up to 10 times higher than in the case of 'normal' nuclear matter ($\rho_0 = 0.167 fm^{-3}$) [13]. The needness for even higher colliding energies led to designing and building of a new accelerator, Relativistic Heavy Ion Colider (RHIC) in BNL which started to operate in the year 2000. Currently, under construction, is a new, most powerful Large Hadron Collider (LHC) at CERN.

The basic aim of current and future experiments with heavy-ion collisions is searching for signatures of the phase transition between the QGP and the hadronic matter and for the QGP itself. The information about the QGP formation in the early stage of the collision is carried by electromagnetic (thermal photons and dileptons) and hadronic (enlarged production of strangeness, suppressed $J/\Psi$ production and high $p_T$ jets) signatures. The next, but not less important task, is to answer the question which Equation of State (EoS) governs the behavior of matter in the QGP phase. Due to that, the investigation of collective effects in nucleus-nucleus collisions takes an important role. The high (spatially anisotropic) pressure created during the non-central collision results in later fast expansion of matter created in such a collision and in appearance of a collective flow.

Although different types of collective flow, as longitudinal, radial and anisotropic transversal flow are investigated separately, they are in fact interconnected and represent different manifestations of the same phenomenon - the collective expansion of matter created in the nucleus-nucleus collision. The longitudinal flow is an ordered expansion of the system along the beam axis and analysis of rapidity distributions can show its existence. The radial flow is introduced in order to explain the distributions *vs* transverse mass $m_T$ for different kinds of particles. The investigation of the radial flow can give the information about the temperature achieved in the system. The anisotropic transverse flow appears as a dominant emission of particles in a certain direction in the transverse plane of the collision.

One of the experiments which has been used in one of the facilities mentioned at the beginning of this Section is the ChErenkov Ring Electron Spectrometer (CERES) designed to measure low-mass $e^+e^-$ pairs created in proton-nucleus and nucleus-nucleus collisions at SPS [14–16]. Dileptons have a particular significance as a probe for hot and dense matter due to the fact that they, in contrast to the hadrons, interact only electromagnetically. Hence, they probe the early stage of the collision.

Beside the dilepton signals, the CERES experiment is also able to detect charged hadrons and to measure their momenta with high precision. This allowed to perform an investigation of another probe of the early stages of the heavy ion collisions - so called anisotropic transverse flow and especially, elliptic flow. The investigation of the elliptic flow of $\Lambda$, $K^0_S$, protons and pions will be the main aim of the analysis presented in this thesis. The elliptic flow itself appears as an azimuthally anisotropical emission of particles with respect to the reaction plane of the collision. This is a collective effect created due to an anisotropic pressure gradients built up as a consequence of a geometrically anisotropic shape of the overlapping zone of the colliding nuclei. The information which the elliptic flow can provide could be used to get some insight about the EoS of the nuclear matter under study [17].

## 1.3 Overview of this Thesis

In this thesis the analysis of the anisotropic transverse flow of charged ($\pi^{\pm}$ and protons) and strange ($\Lambda$ and $K^0_S$) particles emitted in Pb+Au collisions at the highest SPS energy (158 AGeV/c in the laboratory system) was performed.

This thesis is organized in the following way. In Chapter 2 are described the basic features of QGP as well as the signatures of the QGP. The special emphasis is set on the elliptic flow as a signature for the QGP. Chapter 3 gives an overview of methods developed and used in the anisotropic flow analysis starting from the oldest, and now an obsolete one, *sphericity tensor* method up to the newest one, the so called method of *Lee-Yang zeroes*. Chapter 4 describes the CERES experimental setup. In Chapter 5 is presented the *Flowmaker*, a Monte Carlo flow simulator, together with the results from the simulated data. The results from the analysis of the experimental data are presented in Chapters 6 - 8. In these, main Chapters of this thesis is described the analysis of the anisotropic transverse flow of charged ($\pi^{\pm}$ and protons) and strange ($\Lambda$ and $K^0_S$) particles. The obtained results are also compared to the hydrodynamical model and to the results on the flow analysis from the other experiments. These comparisons are the contents of Chapter 9. Chapter 9 also contains the results on the scaling properties of the elliptic flow obtained from the CERES data. Finally, Chapter 10 contains the conclusions and outlook.

# Chapter 2

# QGP AND HEAVY-ION COLLISIONS

## 2.1 The Lattice Quantum Chromo Dynamical Predictions

The phase diagram of strongly interacting bulk matter in the regime of high energy density and temperature should be described by Quantum Chromo Dynamics (QCD). In a simple picture of non-interacting massless quarks and gluons, the Stefan-Boltzmann (SB) pressure ($p_{SB}$) at zero chemical potential is given by the number of degrees of freedom [18]:

$$\frac{p_{SB}}{T^4} = [2(N_c^2 - 1) + \frac{7}{2}N_c N_f]\frac{\pi^2}{90} \tag{2.1}$$

where $N_c$ is the number of colors and $N_f$ is the number of quark flavors. Refinement to this basic picture incorporates color interactions on the partonic level, non-vanishing quark masses and finite chemical potential. In order to solve the problem, the QCD calculations are done on a spacetime lattice (LQCD). In order to extract predictions, the LQCD result had to be extrapolated to the continuum (lattice spacing $\rightarrow 0$), chiral (actual current quark masses) and thermodynamic (large volumes) limits. The LQCD investigations [19] show that matter with zero baryon density undergoes a phase transition at the critical temperature of $T_c = (173 \pm 15)$ MeV from a color-confined hadron resonance gas (HG) to a color-deconfined QGP. The critical energy density $\epsilon_c = 0.7\ GeV/fm^3$ roughly corresponds to the energy density in the center of a proton. Fig. 2.1 shows the normalized energy density $\epsilon/T^4$ and pressure $p/T^4$ *vs* temperature obtained from the LQCD for $0$, $2$, $3$ light and $1$ heavier (strange) quark flavor [19]. One can see that when the phase transition occurs the normalized energy density grows dramatically by roughly one order of magnitude over a rather narrow temperature interval, while the normalized pressure is continuous and grows more gradually. Both saturate at about $75 - 85\%$ of the Stefan-Boltzmann value for an ideal gas of non-interacting quarks and gluons. The energy density reaches the saturation value very quickly (at about $1.2\ T_c$) while the pressure grows slower and reaches the saturation at higher temperatures. The Lattice calculations show that for temperatures above $2\ T_c$, the EoS corresponds to the equation of state of an ideal gas of massless particles, i.e. $\epsilon = 3p$. For temperatures below $2\ T_c$, the deviation from the SB limit indicates substantial remaining interactions among the quarks and gluons in the QGP phase.

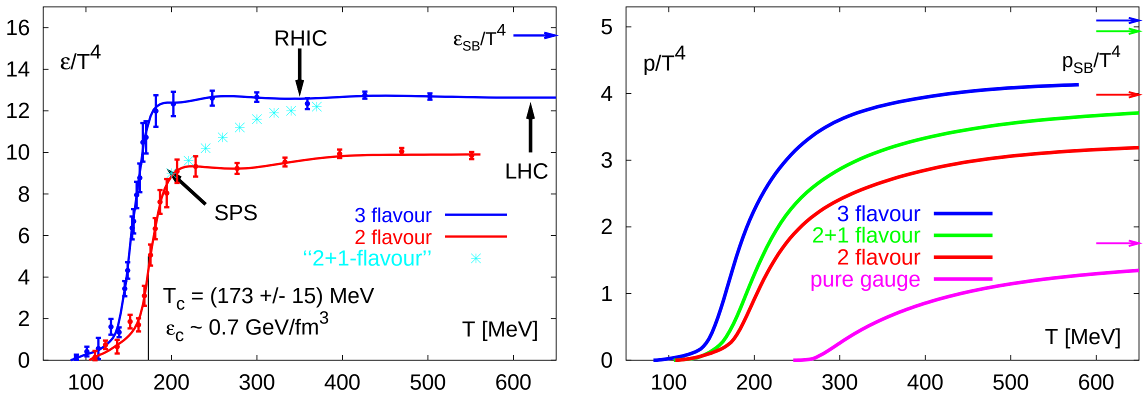

**Figure 2.1:** The normalized energy density $\epsilon/T^4$ and pressure $p/T^4$ *vs* temperature obtained from LQCD for $0$, $2$ and $3$ light quark flavors, as well as for $2$ light $+1$ heavier (strange) quark flavors. Horizontal arrows on the right show the corresponding values for Stefan-Boltzmann gas.

.

Beside the predictions described above, here below are listed the other LQCD predictions

1. Above the critical temperature the effective potential between a heavy quark-antiquark pair is a screened Coulomb potential with screening mass which rises with the temperature [20]. That is not in accordance with perturbative QCD expectations. The increasing of the screening mass leads to a shortening of the range of the $q\bar{q}$ interaction and to suppression of the charmonium production [21, 22].

2. The phase transition is also accompanied by a chiral symmetry restoration [23]. The reduction in the chiral condensate leads to variations in in-medium meson masses.

3. The kind of the phase transition strongly depends on the number of the dynamical quark flavors included in the calculation and on the quark masses [24]. The realistic calculations with two light quarks ($u$ and $d$) and one heavier ($s$) at zero chemical potential gives a crossover type of transition without discontinuities in thermodynamical observables.

4. The calculations at non-zero chemical potential suggest the existence of a critical point such as illustrated in Fig. 2.2 [1]. There is still considerable ambiguity about the value of $\mu_B$ (between $350$ and $700$ $MeV$) at which the critical point occurs in these calculations.

## 2.2 Geometry and Space-Time Evolution of a Heavy-Ion Collision

Nuclei which take part in a collision are objects of the finite volume and hence their geometry has an important role in the understanding of the heavy-ion collisions. Both

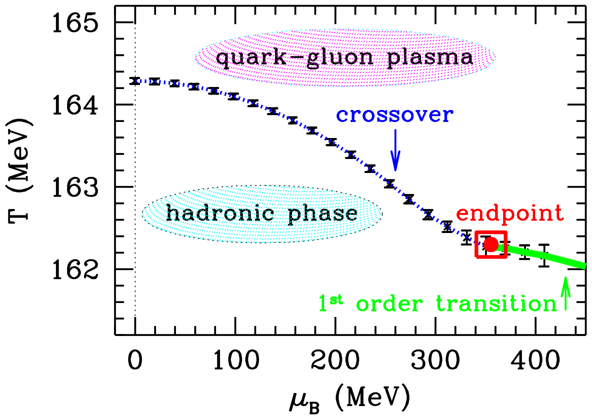

**Figure 2.2:** The LQCD results for non-zero chemical potential [1] suggest the existence of a critical point well above RHIC chemical potential values. The solid line represent a 1-st order phase transition, while the dotted one indicates a crossover transition between two phases.

nuclei are Lorentz contracted in the direction of their relative movement (usually z-axis of the experiment) what leads to a high baryon density. The impact parameter vector $\vec{b}$ connects, in the transverse $x-y$ plane, the center of the target with the center of the projectile and points from the target to the projectile. Its magnitude goes from 0 to $R_A + R_B$, where $R_A$ and $R_B$ are the radii of the colliding nuclei. According to the magnitude of the impact parameter vector one can distinguish peripheral (high magnitude of the vector $\vec{b}$) and central (small magnitude of the vector $\vec{b}$) collisions. In the case of peripheral collisions, the overlapping region between the nuclei is minimal, while in the case of

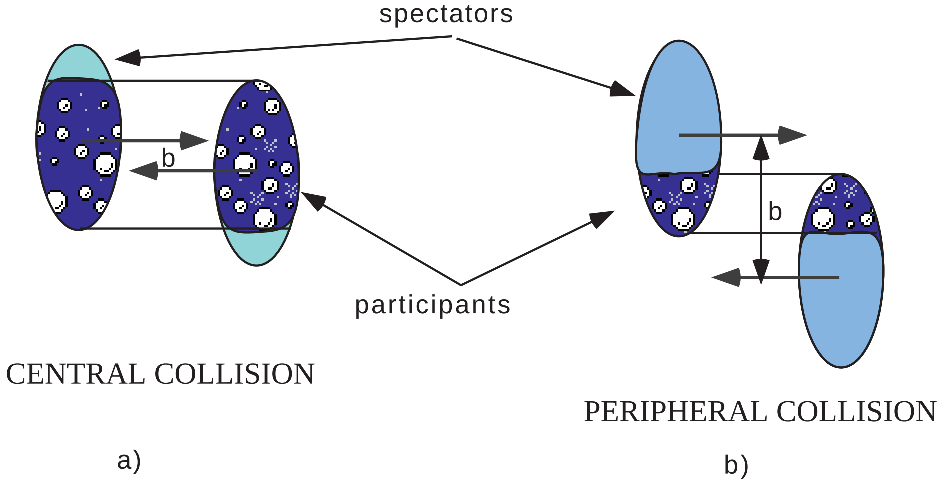

**Figure 2.3:** A cartoon presentation of a central (a) and a peripheral (b) collision in $x-z$ plane of the collision.

central collisions it is maximal. In between these two extreme classes of the collisions are so called semicentral collisions. As an example, Fig. 2.3 shows as a cartoon a central (a) and a peripheral (b) collision in $x-z$ plane of the collision.

Space-time evolution of a heavy-ion collision can be divided into three stages: The early stage of the collision, the stage of expansion and the freeze-out stage. An example

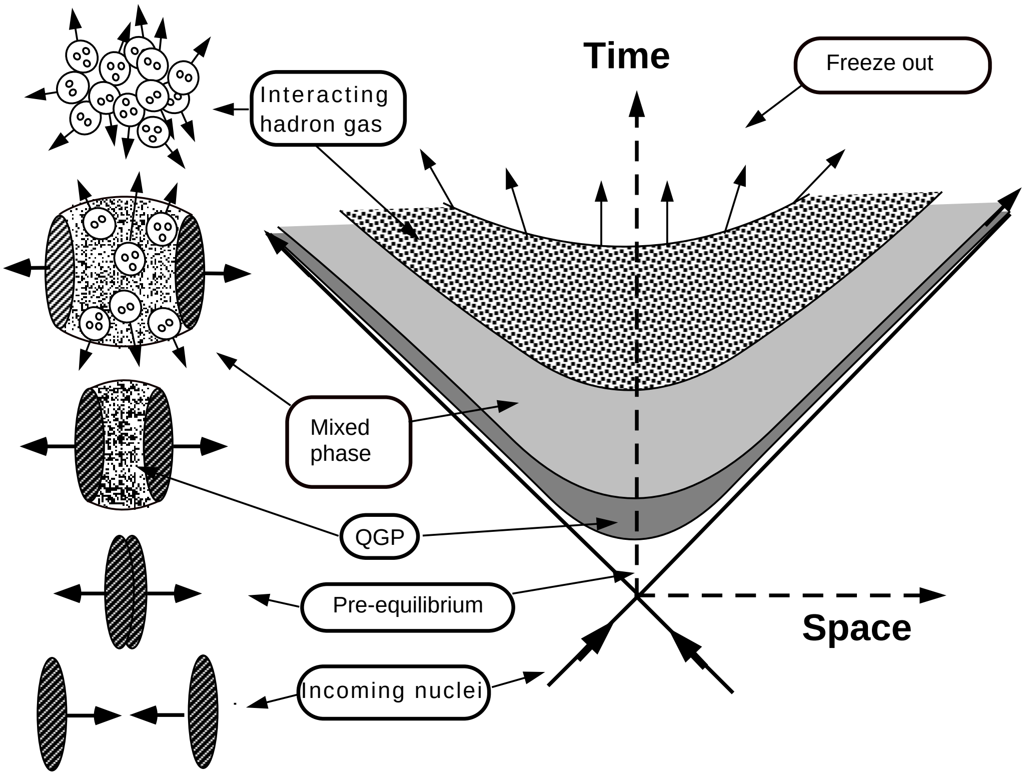

**Figure 2.4:** Schematic space-time evolution of a central heavy-ion collision with a QGP phase formed during the collision.

with the formation of the QGP is shown in Fig. 2.4.

1. *Early stage of the collision*

   Compression of matter in the early stage of the collision leads to increasing of energy density. A part of the incident energy of the colliding nuclei is redistributed into other degrees of freedom. A short time after the beginning of the collision from the highly excited QCD field appear secondary quarks. When a critical quark density $\rho_c$ is reached a transition from 'normal' hadron matter into a color deconfined matter and restoring of chiral symmetry occurs. The energy density of the produced medium is given by the Bjorken estimate [25]

   $$\epsilon = (\frac{dN}{dy})_{y=0} \frac{E_h}{\pi R_A^2 \tau_0} \tag{2.2}$$

   where $(\frac{dN}{dy})_{y=0}$ is the number of produced hadrons per unit rapidity at the midrapidity, $E_h$ is the average energy of produced hadrons, $R_A$ is the nuclear radius and $\tau_0$ is the formation time of the medium which is not known but approximately it is taken to be 1 fm/c. In the case of central Pb+Pb collisions at $\sqrt{s_{NN}} = 17$ GeV/c, the Bjorken estimate gives the initial energy density of 3.5 GeV/fm$^3$ [26] which is much higher than the LQCD prediction of $\approx$1.0 GeV/fm$^3$ where the phase transition to deconfined quark and gluons occurs.

Given these large densities, in the created system of partons[1]under certain conditions multiple parton-parton collisions can establish a local thermodynamical equilibrium. If the time necessary for the thermalization is small enough in comparison to the life of the system, the system can transit into a new phase, equilibrated QGP. The experiments with heavy-ion collisions should answer the following question: Are the interactions copious enough and rapid enough to thermalize the dynamic and expanding matter created in the laboratory?

2. *Stage of expansion*

   Regardless of whether QGP was formed or not, the high pressure built up in the collision will result in a fast expansion of the created system. If in the early stage of the collision the QGP was formed, during the expansion the temperature of the system will decrease and at the critical temperature $T_c$ will appear a transition into a mixed phase in which partons and hadrons exist together. In the mixed phase many partonic degrees of freedom are redistributed into a smaller number of hadronic degrees of freedom. In the hadronic phase, constituents of the system still interact and the system continues to expand. The temperature of the system in the hadronic phase is still very high (smaller than $T_c$ but higher than the freeze-out temperature $T_{fo}$).

3. *Freeze-out stage*

   With the expansion the mean free path of particles becomes larger. The freeze-out appears when the mean free path becomes large enough. Then, by definition, the strong interaction between the particles ceases and they continue to move freely.

Measuring observables as the phase-space distributions of the produced particles, the ratio of multiplicities between different particles species, the anisotropic transverse flow and the $n$-particle correlations ($n = 2, 3, ...$) one can get the information about different evolution stages in nucleus-nucleus collisions.

## 2.3 Heavy-Ion Collisions and Signatures of the QGP

Although in the theoretical treatment of the thermodynamic and hydrodynamic behavior of the QGP was done a lot, the complexity of heavy-ion collisions introduces significant quantitative ambiguities in deriving conclusions. Due to that one must identify the most striking qualitative predictions of the QCD theory, which are able to survive the quantitative ambiguities and to look for a congruence of different observables which support such predictions.

In Fig. 2.5 is shown the phenomenological phase diagram of strongly interacting matter [2, 27, 28] where different phases of the nuclear matter are present. In order to understand the nuclear EoS one has to measure parameters which govern the transition between

---

[1] Valence quarks, sea quarks and gluons have one common name *partons*.

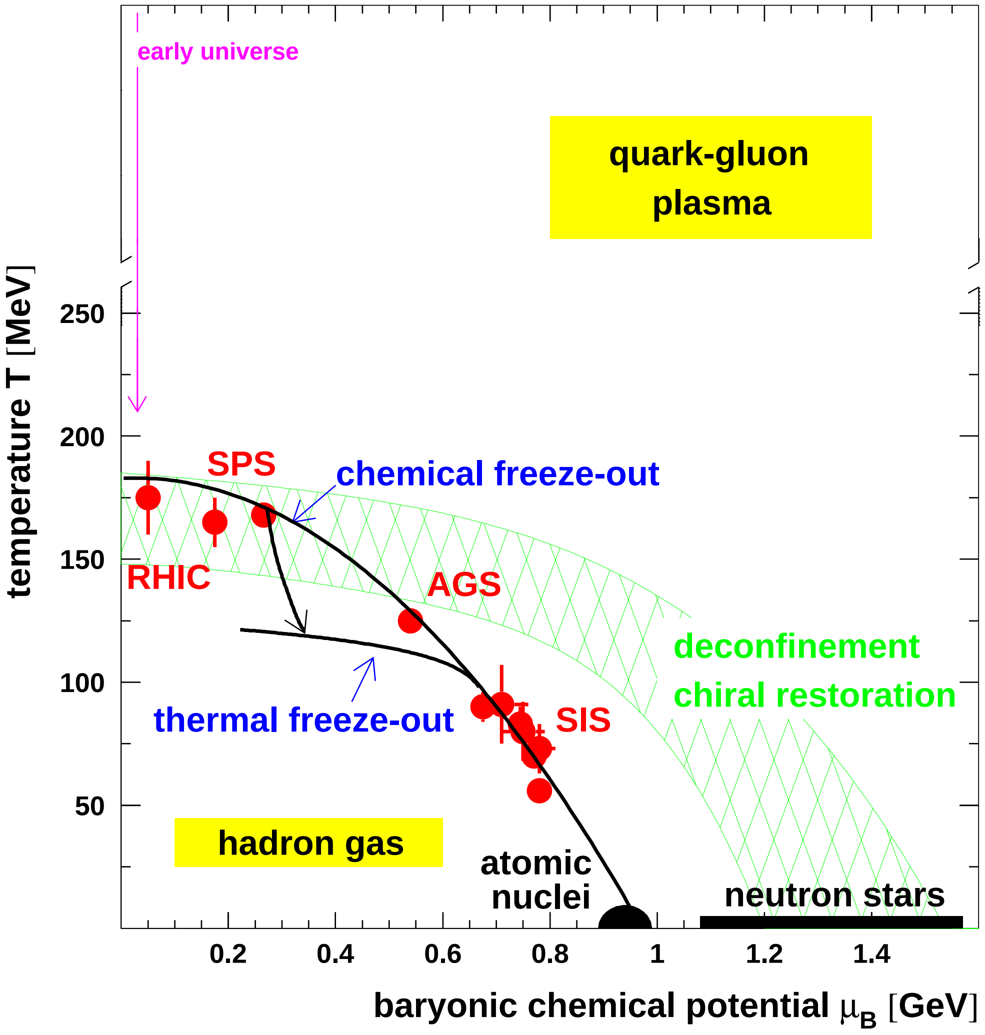

**Figure 2.5:** The QCD phase diagram of the hadronic matter [2]. The points show chemical freeze-out of hadrons extracted from different heavy-ion experiments.

different phases. The phase boundary can be constructing by equating chemical potential $\mu_B$ and pressure $p$ between two phases. The properties of the system at the freeze-out are well known from the systematic study of particle ratios. The extracted freeze-out temperatures and baryon chemical potentials from the experimental data with the incident energy beyond 10 AGeV are very close to the expected phase boundary.

## 2.4 Collective Flow as Signature of the QGP

Combining concepts from particle physics and nuclear physics gives a new approach in investigating the properties of matter and its interactions. In high energy physics ($E/m \gg 1$), *interactions* are derived from gauge theories, and the *matter* consists of partons [2]. In contrast, on nuclear physics scale, the strong interactions are shielded and can be derived only in phenomenological theories, whereas the matter consists of extended systems which show collective behavior.

If initial interactions among the constituents are sufficiently strong to establish local thermal equilibrium and to maintain it during a significant evolution time, then the resulting matter may be treated as a relativistic fluid undergoing collective, hydrodynamical flow. The hydrodynamical treatment for the description of fireballs formed in heavy-ion collisions has a long history [29–32]. The details of the hydrodynamical evolution are sensitive to the EoS of the flowing matter. Hydrodynamics cannot be applied to matter which is not in a local thermal equilibrium, hence it must be supplemented with a phenomenological treatment for early and late stages of the collisions. The motion of an ideal non-viscous fluid is completely described with the fluid velocity ($\vec{v}$), the pressure ($p$) and the energy and baryon density ($\epsilon$ and $n_B$). From the EoS $p = p(\epsilon, n_B)$ one can find the slope $\frac{\partial p}{\partial \epsilon}$ which gives the square of the velocity sound ($c_s^2$) exhibiting a high value (close to $1/3$) for the hadron gas and especially for the QGP, but has a soft point at the mixed phase [31]. This softening of the EoS during the assumed phase transition has consequences to the system evolution.

In non-central collisions, the reaction zone has an almond shape which results in an azimuthally anisotropic pressure gradients. It produces a non-trivial elliptic flow pattern. Experimentally it is usually measured via a Fourier decomposition of the transverse momentum distribution relative to the reaction plane which is defined with the beam direction and the impact parameter vector $\vec{b}$. The important feature of the elliptic flow is the ”self-quenching” [33, 34] because the flowing of matter, induced by pressure, tends to reduce spatial anisotropy and to increase momentum anisotropy. Due to that, the self-quenching makes the elliptic flow sensitive to early collision stages when the spatial anisotropy and pressure gradients are the biggest.

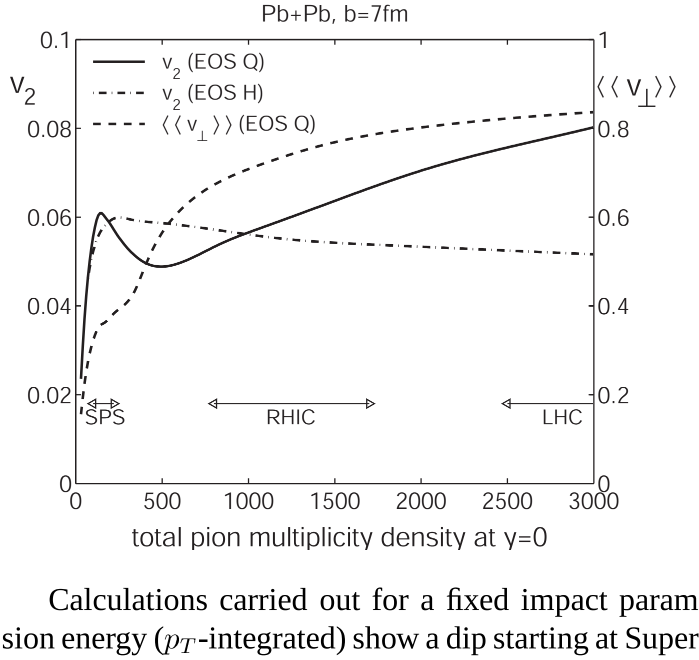

**Figure 2.6:** Hydrodynamical predictions of $v_2$ excitation functions (left axis) and radial flow velocity $\langle\langle v_\perp \rangle\rangle$ (right axis) for non-central Pb+Pb collisions [3].

Calculations carried out for a fixed impact parameter vector as a function of collision energy ($p_T$-integrated) show a dip starting at Super-Proton-Synchrotron (SPS) energy

---

[2] or hadrons if the energy is not large enough.

(Fig. 2.6 [3]). The existence of the dip reflects the softening of the EoS used. However, comparison of predicted (Fig. 2.6) with measured (Fig. 2.7 [4]) excitation functions for the elliptic flow are subject to ambiguity concerning where and when the appropriate conditions of initial local thermal equilibrium for hydrodynamic applicability are actually achieved.

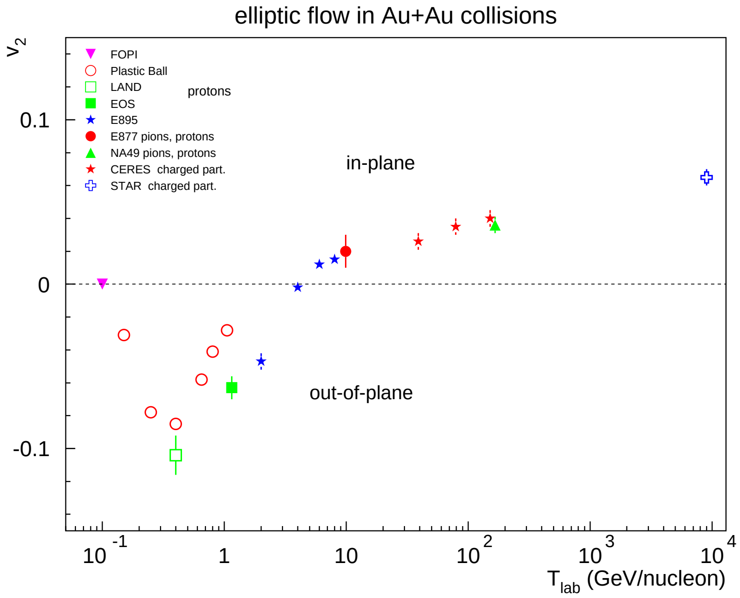

**Figure 2.7:** The beam energy dependence of the elliptic flow. The figure is taken from [4].

Another way to attain sensitivity of the elliptic flow to the EoS is the predicted elliptic flow magnitude on hadron $p_T$ and mass measured at a given collision energy and centrality. The mass dependence has a simple kinematic origin, but the flow magnitude depends on EoS's details. That is the reason why the pion, proton, $\Lambda$ and $K_S^0$ elliptic flow analysis was performed in this thesis. Another reason for the $\Lambda$ and $K_S^0$ elliptic flow measurement is that the elliptic flow of strange particles can give an insight into very early stages of the collisions.

Comparing the elliptic flow intensities between mesons and baryons one can have an insight into mechanisms which govern the hadronization of the dense matter created in the heavy-ion collisions. Certain scaling scenarios were developed in order to perform such kind of investigation.

The energy-, $p_T$- and mass-dependence of the elliptic flow is also affected by species-specific hadronic final state interactions close to the freeze-out where particles decouple from the system freely flying to the detector where hydrodynamics is not applicable anymore. A combination of macroscopic and microscopic models with hydrodynamics applied at the early partonic and mixed-phase stages and hadronic transport models such as RQMD [35] at the later hadronic stage may offer a more realistic description of the whole evolution than that achieved with a simplified sharp freeze-out treatment.

# Chapter 3

# METHODS IN FLOW ANALYSIS

In the investigations of the flow phenomena, different methods for the measurement of its magnitude were developed. First, quite shortly will be described two oldest methods, the *sphericity tensor* [36] and the *mean transverse momentum* in the reaction plane [37]. The concept of the *reaction plane* will be presented gradually in Section 3.2. That concept is necessary for the explanation of the two widely used methods in the flow analysis: the already mentioned mean transverse momentum and the *Fourier analysis* of the particle azimuthal distributions constructed with respect to the reaction plane [38–42]. The method of Fourier analysis will be described as a generalization of the mean transverse momentum method. The presentation of the methods in flow analysis will be continued with the method of *two-particle correlations* [43] which does not use the idea of the reaction plane for measuring the flow magnitude. In this thesis, for the Fourier analysis and for the two-particle correlations will be used a common name: the Standard Flow Analysis. The methods of the Standard Flow Analysis are mainly insensitive to the non-flow effects. In order to distinguish flow from the non-flow contributions, J.-Y. Ollitrault developed the *cumulant* method [44, 45] and the method of *Lee-Yang zeroes* [46, 47]. These methods will be presented in the last two sections of this Chapter.

## 3.1 Sphericity Tensor

As a first approach in the flow investigation appeared the method of the kinetic-energy flow tensor. This method is based on the construction of the second order spherical tensor $F_{\alpha\beta}$ (which will be shortly named as sphericity tensor) defined in the center-of-mass frame as

$$F_{\alpha\beta} = \sum_{i=1}^{M} p_{i\alpha} p_{i\beta}/2m_i, \qquad\qquad \alpha, \beta = x, y, z \tag{3.1}$$

Here, $p_{i\alpha}$ and $m_i$ are the momentum component and the mass of the $i$-th particle respectively. The sum goes over all particles $M$ detected in the collision. In that way, $F_{\alpha\alpha}$ represents the total kinetic energy in the non-relativistic limit. The orientation and the values of the principal axes could be obtained by diagonalization of the $F_{\alpha\beta}$. Thus, the event shape in momentum space could be presented by such an ellipsoid. The sphericity tensor method also gives the information about the direction of the total momentum flow. The angle between the beam axis and the eigenvector associated with the largest eigenvalue of this tensor defines the flow angle $\Theta_F$ which was used for quantifying the magnitude of the directed flow.

The sphericity tensor method was used for small colliding energies [36] while in the case of high energies it is not used because the flow angle $\Theta_F \approx \langle p_x \rangle / p_{beam}$ [1]is too small ($\ll 1$) and the information about the differential flow magnitude is not provided.

## 3.2 Mean Transverse Momentum in the Reaction Plane

The description of non-central collisions is more complicated than that of very central collisions because of presence of the azimuthal asymmetry in the initial state of the interaction. Nevertheless, two colliding nuclei obey a reflection symmetry with respect to the reaction plane. Although the structure of the colliding nuclei gets destroyed, the reflection symmetry which was present in their initial state should be preserved during the collision. The momentum distribution of nucleons in the nuclei is isotropic in the transverse $(x - y)$ laboratory plane. But the spatial distribution of matter does not have that property (for finite impact parameter $\vec{b}$). Due to that, the momentum distribution evolves from isotropy into an anisotropic shape but with an overall reflection symmetry. In Fig. 3.1 the spatial asymmetry is represented by an overlapping zone (red area). The natural tendency of the matter is to flow in the direction with the highest pressure gradient. That as a consequence produce a collective anisotropical expansion of particles preferentially emitted in the direction with the highest pressure gradient (Fig. 3.1 bottom). The transverse momentum

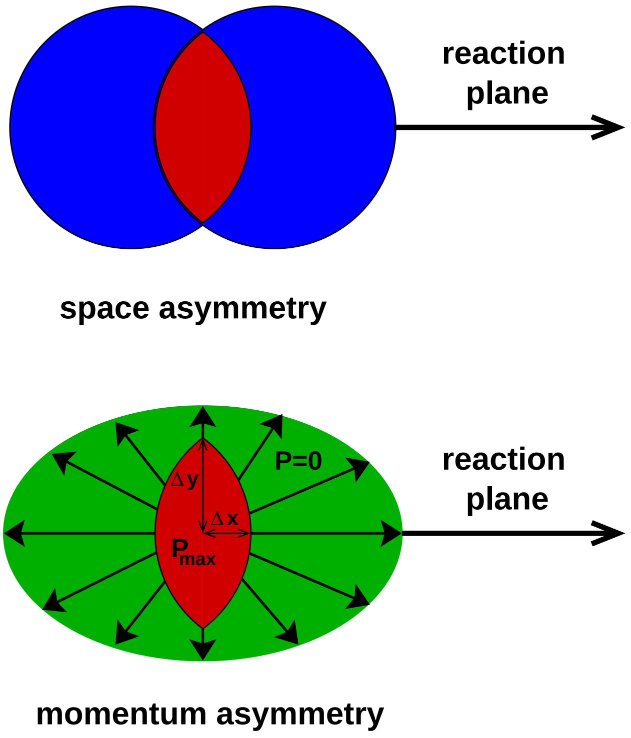

**Figure 3.1:** A schematic view of a collision of two nuclei in the transverse plane. The spatial asymmetry, showed at the top, is transformed into a momentum asymmetry, showed at the bottom, due to the pressure gradient which was built up during the collision.

---

[1] $\langle p_x \rangle$ will be defined in Section 3.2

method attempts to exploit and quantify possible anisotropies in the transverse momenta associated with the reaction plane. Therefore, every event should be analyzed with respect to this initial azimuthal asymmetry. This asymmetry is fully determined by the reaction plane and the magnitude of the impact parameter vector $\vec{b}$. In the literature, the reaction plane is also known as the event plane.

The reaction plane is defined by the impact parameter vector $\vec{b}$ and beam axis. If one assumes that the beam axis corresponds to the longitudinal ($z$) axis of the experiment then the reaction plane is determined by the angle $\Phi$ between the $\vec{b}$ and the $x$ axis of the experiment (which could be arbitrarily chosen).

The transverse momentum method was proposed by Danielewicz and Odyniec [37]. It was used over a wide range of colliding energies, from 25A MeV in the center-of-mass system [48] to above 60A GeV [49]. In the original Danielewicz&Odyniec approach, the underlying assumption is that particles are emitted in opposite direction in the forward ($y > y_{cm}$) and backward hemisphere ($y < y_{cm}$) owing to the momentum conservation. Then, the orientation of the reaction plane, i.e. the $\Phi$ angle, is determined by a vector $\vec{Q}$ constructed as

$$\vec{Q} = \sum_{i=1}^{M} w_i \vec{p}_{i,T}, \tag{3.2}$$

where the weight $w_i$ is $0$ for pions and midrapidity protons, $+1$ for protons emitted in the forward hemisphere ($y \geq y_{cm} + \delta$) and $-1$ for protons emitted in the backward hemisphere[2]($y \leq y_{cm} - \delta$). Such a choice of weights corresponded to the strong proton directed flow at low energies. The optimal value of $\delta$ could be determined by minimization of the error in the determination of the reaction plane.

This method has been applied to evaluate directed flow in terms of the mean transverse momentum of particles projected into the reaction plane $\langle p_x \rangle$ [37]. The obtained dependence on the rapidity has a characteristic S shape and the slope of that curve given by

$$F_y = \frac{d\langle p_x \rangle / A}{dy} \tag{3.3}$$

is used to quantify the strength of the directed flow. The normalization to the mass number transforms the momentum into a velocity and this makes different particle species comparable. In addition to this flow signal, a quantity $p_\alpha^{dir} = \sum_i^N w \cdot \vec{p}_{T,i} \cdot \vec{Q}/|\vec{Q}|$ is used to represent the total transverse momentum into the reaction plane.

### 3.2.1 The Reconstruction of the Reaction Plane

The orientation of the reaction plane is not known *a priori* and as a first step in the flow analysis it is necessary to reconstruct it. It can be reconstructed only if the outgoing particles retains some memory of the initial collision geometry. So, the method uses the anisotropic flow itself to determine it. As there are different types of anisotropic flow, it also means that the reaction plane can be determined independently for each harmonic of the anisotropic flow. The reaction plane vector $\vec{Q}_n$, which defines the reaction plane angle $\Phi_n$ from the $n$-th harmonic is defined by the equations

---

[2] The sign of the weight was arbitrarily chosen and it became a convention

$$
\begin{aligned}
X_n &\equiv Q_n \cos(n\Phi_n) = \sum_{i=1}^{M} w_i \cos(n\phi_i) \\
Y_n &\equiv Q_n \sin(n\Phi_n) = \sum_{i=1}^{M} w_i \sin(n\phi_i)
\end{aligned}
\tag{3.4}
$$

which give its components, or by

$$
\Phi_n = \frac{1}{n} \arctan\left(\frac{Y_n}{X_n}\right) \tag{3.5}
$$

Here, $\phi_i$ represents the azimuthal angle of each outgoing particle. The sums go over all particles $i$ used for the reaction plane determination while $w_i$ are their weights. The weights are chosen in a way to make the reaction plane resolution as good as possible. It could be done by selecting the particles of one particular type, or weighting with rapidity in the case of the directed flow or with transverse momentum in the case of the elliptic flow. Another way is to use the flow magnitude itself as a weight. It can be done in the following way. In the first iteration one can use the weights mentioned above to perform the flow analysis. Then, in the second iteration, the flow analysis will be repeated using the obtained flow intensities as weights. It is obvious that for $n = 1$ and $w_i = p_T$ Eq. (3.2) appears as a special case of the Eq. (3.4).

This is the general method for the reconstruction of the reaction plane orientation. In practice, several problems appear when one tries to use the reaction plane reconstructed with such method to calculate the flow. The reason is the following. The flow calculation is always based on a correlation between a given particle with the reconstructed reaction plane. When a particle has been used in the calculation of the reaction plane, an autocorrelation effect appears. That effect is in the following. Whenever one measures the particle azimuthal angle with respect to the reaction plane reconstructed with Eq. (3.4), an autocorrelation of the given particle with itself appears if that particle is included in sums of Eq. (3.4). In general, whenever one connects a particle with a construction in which that particle is used, the autocorrelation effect arises. The simplest way to remove such an effect is to exclude such a particle from the above mentioned sums. That could be easily done if one saves the sums of sines and cosines from Eq. (3.4), and subtracts the contribution of that particle from these sums. In case when one uses Eq. (3.2) for the reaction plane determination, the modified equation [50] is expressed by

$$
\vec{Q}_j = \sum_{(j\neq)i=1}^{M} w_i \vec{p}_{T,i}, \tag{3.6}
$$

In reality, e.g. in the case of electronic experiments, if one uses hits for the reaction plane reconstruction due to a possible hit splitting the above described method for removing the autocorrelation cannot help. One way to avoid the obstacle is to form tracks by matching hits from different detectors. The other way is to exchange the method. In Section 4.1 will be described so called slice method which is used in this analysis. Using that method the autocorrelation effect, even in case of existence of artificial hit splitting, could be removed completely.

Another effect, the correlation due to the momentum conservation which appeared in the directed flow analysis, could be removed already at the level of reconstruction of the reaction plane. At small energies, where this effect is rather strong, this could be done by redefining of the Eq. (3.6) in the following way [50]. The system that determines the reaction plane $\vec{Q}_j$ is moving in the transverse direction with a momentum $\vec{p}_T = -\vec{p}_{T,j}$. Applying a boost $\vec{v}_b$ to each particle $i$,

$$\vec{v}_b = \frac{\vec{p}_{T,i}}{m_{sys} - m_i} \tag{3.7}$$

means that the system used to evaluate $\vec{Q}_j$ has no net transverse momentum. In Eq. (3.7) $m_{sys}$ stands for the total mass of the system. Then Eq. (3.6) becomes

$$\vec{Q'}_j = \sum_{(j \neq) i=1}^{M} w_i (\vec{p}_{T,i} + m_i \vec{v}_b) \tag{3.8}$$

This procedure leads to a decreasing of the flow magnitude for $1/M$ relative to the flow magnitude obtained with Eq. (3.6) [51]. In Eq. (3.8) $M$ is the number of particles used in the reaction plane reconstruction.

### 3.2.2 Flattening of the $dN/d\Phi$ Distribution

Due to the random distribution of the vector $\vec{b}$ in the transverse $x - y$ plane, for an ideal detector the distribution of the azimuthal angle of the reaction plane $dN/d\Phi$ has to be flat. In reality, different detector effects like the efficiency in $\phi$ smaller than $100\%$, or the geometrical offset between the position of the beam and the center of the detector in the $x - y$ plane make the distribution $dN/d\Phi$ not isotropic. Such an effect should be removed before doing flow analysis. There are several methods to remove such an effect.

The first one is to recenter the $(X_n, Y_n)$ distributions by subtracting $(\langle X_n \rangle, \langle Y_n \rangle)$ values averaged over all events [52–54]. The main disadvantage of this method is that it is not sensitive to anisotropies caused by higher harmonics. If such harmonics are present one needs additional flattening of $\Phi_n$ distributions. In the second method, one can construct the laboratory particle azimuthal distributions for all events and to use the inverse of this as weights in the Eq. (3.4) [52, 53, 55]. The limitation of this approach is that it does not take the multiplicity fluctuations around the mean value into account. A third method, the method of mixed events [52,53,55] is the next one which could be used. The essence of the method is that one could divide the correlations of particles with respect to the non-flat (”raw”) reaction plane by the correlations of particles with respect to the reaction plane determined from another event. Such division can remove the correlations due to the acceptance. In the fourth method one can fit the non-flat distributions of the reaction plane angle $\Phi_n$ to a Fourier expansion and to apply an event-by-event shifting of the reaction planes in order to make the final distributions isotropic [52,53]. The equation for the shift is given by

$$\Delta\Phi_n = \frac{1}{n}\sum_{m=1}^{m_{max}} \frac{2}{m}[-\langle\sin(mn\Phi_n)\rangle\cos(mn\Phi_n) + \langle\cos(mn\Phi_n)\rangle\sin(mn\Phi_n)] \tag{3.9}$$

where $m_{max}$ is usually equal to 4.

In this analysis will be used the method of recentering and Fourier shifting subsequently. The first method will make the raw reaction plane distribution roughly flat. Subsequent applying the Fourier shifting will make the reaction plane distribution completely flat.

### 3.2.3 The Reaction Plane Resolution

Because the position of the true reaction plane is not known *a priori*, one can only perform Fourier decomposition of the invariant particle distribution $E\frac{d^3N}{d^3p}$ with respect to the reconstructed position of the reaction plane $\Phi_n$ where $n$ is the order of the harmonic from which this position is reconstructed. Due to the finite multiplicity, the difference between the true and the reconstructed reaction plane is not zero. So, the measured flow correlation has to be corrected for that *reaction plane resolution*. The reaction plane resolution is given by

$$\langle\cos[n(\Phi_n - \Phi)]\rangle \tag{3.10}$$

where $\Phi$ is the azimuthal angle of the true reaction plane. The resolution depends on the flow harmonic and the flow itself. In order to calculate the value given by (3.10) one constructs reaction planes from two random subevents $a$ and $b$. The two random subevents one gets by dividing the whole event into two pieces with very similar topology. In this case, the simple relation

$$\langle\cos[n(\Phi_n^a - \Phi_n^b)]\rangle = \langle\cos[n(\Phi_n^a - \Phi)]\rangle\langle\cos[n(\Phi_n^b - \Phi)]\rangle \tag{3.11}$$

is valid. An important assumption here is that there are no other correlations except the ones due to the flow. Eq. (3.11) allows to calculate the reaction plane resolution given by (3.10). For example, if one knows the correlations between two equal subevents then the resolution of each of them is

$$\langle\cos[n(\Phi_n^a - \Phi)]\rangle = \sqrt{\langle\cos[n(\Phi_n^a - \Phi_n^b)]\rangle} \tag{3.12}$$

If the two subevents are correlated, then the term inside the square-root in Eq. (3.12) is positive. In Eq. (3.12) one calculates the reaction plane resolution of a subevent. Taking into account that the multiplicity of the full event is twice larger than the one of a subevent then

$$\langle\cos[n(\Phi_n^a - \Phi)]\rangle = \sqrt{2\langle\cos[n(\Phi_n^a - \Phi_n^b)]\rangle} \tag{3.13}$$

## 3.3 Two-particle Correlations

Wang [43] proposed to use two-particle azimuthal correlations in order to investigate the anisotropic flow. The idea is based on the fact that if (in the case of flow) particles are correlated to the reaction plane, then they are also mutually correlated. So, in presence of non-zero flow, the $P_{corr}(\Delta\phi)$ distribution, constructed from two-particle correlations with respect to the relative angle $\Delta\phi = \phi_1 - \phi_2$ between two particles belonging to the same event, is not flat. In reality, due to incomplete $\phi$ acceptance in the detector or due to finite efficiency for detecting particles at different $\phi$'s one has also to construct a background $P_{uncorr}(\Delta\phi)$ distribution in the same way as $P_{corr}(\Delta\phi)$, where now $\Delta\phi$ is the difference between azimuthal angles of particles belonging to two different events. One then constructs the correlation function as a ratio

$$C(\Delta\phi) \equiv \frac{P_{corr}(\Delta\phi)}{P_{uncorr}(\Delta\phi)} \tag{3.14}$$

So, with this mixing technique the physical correlation between two particles is extracted with elimination of the 'detector' effects. In an ideal case, without non-flow effects, one has

$$C(\Delta\phi) = \sum_{n=0}^{+\infty} v_n^2 e^{in(\Delta\phi)} = \sum_{n=0}^{+\infty} v_n^2 \cos(n\Delta\phi) \tag{3.15}$$

a Fourier expansion of the measured correlation function $C(\Delta\phi)$ which gives the integrated flow $v_n$.

For the differential flow, $v_n^{diff}$, one has simply to replace $\phi_1$ with the azimuthal angle $\psi$ of a particle in a narrow phase space window, and $v_n^2$ in Eq. (3.15) is replaced with $v_n v_n^{diff}$.

The crucial limitation of the two-particle correlation method is the impossibility to separate the flow and non-flow correlations.

## 3.4 Fourier Analysis of the Azimuthal Distributions

The dependence on the particle emission azimuthal angle measured with respect to the (true) reaction plane angle ($\Phi$) could be written as a Fourier expansion [38–42] of the invariant particle distribution $E\frac{d^3N}{d^3p}$

$$E\frac{d^3N}{d^3p} = \frac{1}{2\pi}\frac{d^2N}{p_t dp_t dy}\left(1 + \sum_{n=1}^{\infty} 2v_n \cos[n(\phi - \Phi)]\right) \tag{3.16}$$

Sine terms vanish due to the reflection symmetry with respect to the reaction plane. The main advantage of the Fourier method, with respect to the sphericity method, is that the magnitude of the flow, which is characterized by the Fourier coefficients $v_n$, can be corrected for the reaction plane resolution, caused by the finite multiplicity of the event, by multiplying the observed value of $v_n$ with the inverse value of the reaction plane resolution given by (3.13). This correction increases the value of the observed Fourier coefficients. Only the Fourier coefficients corrected for the reaction plane resolution can be compared to the theoretical predictions, or to simulations filtered for the detector acceptance.

The Fourier coefficients in Eq. (3.16) are given by

$$v_n = \langle \cos[n(\phi - \Phi)] \rangle \tag{3.17}$$

where $\langle\rangle$ indicates an averaging over all particles of interest and over all events. A factor 2 in front of each $v_n$ in Eq. (3.16) is used in order to obtain a transparent physical meaning of the Fourier coefficients. In a coordinate system in which the $x$ axis corresponds to a projection of the reaction plane to the laboratory transverse plane are valid the following formulae

$$\cos(\phi - \Phi) = p_x/p_T, \qquad \sin(\phi - \Phi) = p_y/p_T \tag{3.18}$$

Then, according to Eq. (3.17), the coefficient $v_1$ is equal to $\langle p_x/p_T\rangle$ and $v_2$ is equal to $\langle (p_x/p_T)^2 - (p_y/p_T)^2\rangle$. Now, it is obvious that the coefficient $v_1$ corresponds to the directed flow, and $v_2$ to the elliptic flow.

## 3.5 The Cumulants

The reaction plane $\Phi$ cannot be measured directly. As the correlation between each particle and the reaction plane induces correlations among the particles themselves, $v_n$ coefficients could be experimentally measured from the azimuthal correlations between the outgoing particles. These correlations are called ”*flow correlations*”. Both methods, the reaction plane and two-particle correlations are in use at intermediate and ultrarelativistic energies, but in both methods one usually assumes that the only source of azimuthal correlations is the flow. However, this assumption especially is not valid at SPS energies, where ”*direct*”, non-flow two-particle correlations become of the same magnitude as the flow correlations itself. Standard methods extract flow from two-particle azimuthal correlations, either directly [43, 56], or through the correlation with respect to the reaction plane [37, 38, 41]. However, the correlation between two given particles is not only due to the flow but also due to the other sources of correlation as quantum Bose-Einstein effects, momentum conservation, resonance decays, jets, etc. When the flow is small, these effects may dominate the measured signal. The impact of the 'non-flow' correlations on the flow analysis might be minimized by cuts in phase-space which could be used to avoid the influence of quantum effects and resonance decays, while the contribution of momentum conservation can be calculated and subtracted *a posteriori* [57]. However, these various prescriptions require some *a priori* knowledge of non-flow correlations. So, it is necessary to assume that *all* such sources of correlations are known and accounted for, which may not be true. A new method of flow analysis, based on a cumulant expansion of multiparticle azimuthal correlations can overcome these difficulties [45]. The principle of the method is that when the cumulants of higher order are considered, the relative contribution of non-flow effects, and thus the corresponding systematic errors, decreases. Denote by $\phi_j$, where $j = 1, ..., M$, the azimuthal angle of the particle detected in an event with multiplicity $M$. Multiparticle azimuthal correlations could be generally written in the form $\langle e^{in(\phi_1+...+\phi_k-\phi_{k+1}-....-\phi_{k+l})}\rangle$, where $n$ is the Fourier harmonic under study and the brackets indicate an average over all possible combinations of $k+l$ particles detected in the same event and over all events. Correlations between $k+l$ particles could be decomposed into a sum of terms involving correlations between a smaller number of particles. For instance, two-particle correlations $\langle e^{in(\phi_1-\phi_2)}\rangle$ can be written as:

$$\langle e^{in(\phi_1-\phi_2)}\rangle = \langle e^{in\phi_1}\rangle\langle e^{-in\phi_2}\rangle + \langle\langle e^{in(\phi_1-\phi_2)}\rangle\rangle \tag{3.19}$$

where $\langle\langle e^{in(\phi_1-\phi_2)}\rangle\rangle$ is by definition the second order cumulant. In order to understand the physical meaning of the cumulant, consider a 'perfect' detector, i.e. a detector with an isotropic acceptance. Then, the average $\langle e^{in\phi_j}\rangle$ vanishes due to the symmetry since $\phi_j$ is measured in the laboratory, not with respect to the reaction plane. The first term in the right-hand side (r.-h.s.) of Eq. (3.19) vanishes and the cumulant reduces to the measured two-particle correlations. The importance of cumulants appears at a more realistic case of a non-perfect detector. Then the first term on the r.-h.s. of the Eq. (3.19) can be non-vanishing. But the cumulant vanishes if $\phi_1$ and $\phi_2$ are uncorrelated. Then the cumulant $\langle\langle e^{in(\phi_1-\phi_2)}\rangle\rangle$ isolates the physical correlation and disentangles it from trivial detector effects. There are several physical contributions to the correlations $\langle\langle e^{in(\phi_1-\phi_2)}\rangle\rangle$ which separate into flow and non-flow correlations. When the source is isotropic (there is no flow), only direct correlation remains. Direct correlation scales with the multiplicity $M$ like $1/M$ [57,58]. So, the correlation between two arbitrary pions is proportional to $1/M$. If there is a flow, a correlation between emitted particles and the reaction plane, it generates azimuthal correlations between any two outgoing particles, and gives a contribution $v_n^2$ to the second order cumulant. One can measure the flow using second order cumulant if this contribution dominates over the non-flow contribution, i.e. if $v_n \gg 1/\sqrt{M}$ [57,58]. This is the domain of validity of the standard flow analysis, which is based on two-particle correlations.

### 3.5.1 Integrated Flow

The main benefit of the use of cumulants is in construction of higher order cumulants and separation flow from non-flow correlations. To illustrate it consider a perfect detector and decompose the measured four-particle correlation as:

$$\begin{aligned}\langle e^{in(\phi_1+\phi_2-\phi_3-\phi_4)}\rangle = \langle e^{in(\phi_1-\phi_3)}\rangle\langle e^{in(\phi_2-\phi_4)}\rangle + \langle e^{in(\phi_1-\phi_4)}\rangle\langle e^{in(\phi_2-\phi_3)}\rangle \\ +\langle\langle e^{in(\phi_1+\phi_2-\phi_3-\phi_4)}\rangle\rangle \qquad (3.20)\end{aligned}$$

where two first terms in the r.-h.s. comes from possible two-particle combinations. The remaining term $\langle\langle e^{in(\phi_1+\phi_2-\phi_3-\phi_4)}\rangle\rangle$ is the fourth-order cumulant by definition. Although it is insensitive to two-particle non-flow correlations it could be sensitive to higher order non-flow correlations, i.e. direct four-particle correlations. Fortunately their probability is very small. Due to the symmetry between $\phi_1$ and $\phi_2$ ($\phi_3$ and $\phi_4$) the Eq. (3.20) can be rewritten as:

$$\langle e^{in(\phi_1+\phi_2-\phi_3-\phi_4)}\rangle = 2\langle e^{in(\phi_1-\phi_3)}\rangle^2 + \langle\langle e^{in(\phi_1+\phi_2-\phi_3-\phi_4)}\rangle\rangle \qquad (3.21)$$

So, in principle it is possible to construct an expression for the $4^{th}$ order cumulant which eliminates both detector effects and non-flow correlations.

#### Generating Functions

Even without assuming a perfect detector, cumulants could be expressed via generating functions. The generating function $G_n(z)$ is a real valued function of a complex variable

$z = x + iy$ defined as:

$$G_n(z) = \prod_{j=1}^{M}[1 + \frac{w_j}{M}(z^\star e^{in\phi_j} + ze^{-in\phi_j})] \tag{3.22}$$

in each event, where $z^\star = x - iy$ is the complex conjugate of $z$ and $w_j$ is a statistical weight chosen in some way. This function could be averaged over events with the same multiplicity $M$. The expansion of such a function into power series generates correlations to all orders:

$$\begin{aligned}\langle G_n(z)\rangle = ... = 1 + z\langle e^{-in\phi_1}\rangle + z^\star\langle e^{in\phi_1}\rangle + \frac{M-1}{M} \times \\ \times\Big(\frac{z^2}{2}\langle e^{-in(\phi_1+\phi_2)}\rangle + \frac{z^{\star 2}}{2}\langle e^{in(\phi_1+\phi_2)}\rangle + zz^\star\langle e^{in(\phi_1-\phi_2)}\rangle\Big) + ...\end{aligned} \tag{3.23}$$

In this way the *averaged* generating function $\langle G_n(z)\rangle$ contains all the information about multiparticle azimuthal correlations.

In the case of the perfect detector, $\langle G_n(z)\rangle$ does not depend on the phase of $z$, but only on its magnitude $|z| = \sqrt{x^2 + y^2}$. If one changes $z$ into $ze^{in\alpha}$, the only effect is a shift of all angles by the same quantity. But, as the probability that one event occurs under a global rotation is unchanged, one concludes that $\langle G_n(z)\rangle$ is invariant under such a transformation.

The *generating* function of the cumulants is defined as:

$$\mathcal{C}_n(z) \equiv M\big(\langle G_n(z)\rangle^{1/M} - 1\big) \tag{3.24}$$

and its expansion into power series of $z$ and $z^\star$ defines the cumulants

$$\mathcal{C}_n(z) \equiv \sum_{k,l} \frac{z^{\star k} z^l}{k!l!}\langle\langle e^{in(\phi_1+...+\phi_k-\phi_{k+1}-...-\phi_{k+l})}\rangle\rangle \tag{3.25}$$

If particles are uncorrelated, all the cumulants beyond order one are vanished. Indeed, if all $\phi_j$ in Eq. (3.22) are independent from each other, then the mean value of the product is the product of the mean values

$$\langle G_n(z)\rangle = M\big(1 + \frac{1}{M}(z^\star\langle e^{in\phi}\rangle + z\langle e^{-in\phi}\rangle))\big)^M \tag{3.26}$$

Then the generating function of the cumulants reduces to

$$\mathcal{C}_n(z) = z^\star\langle e^{in\phi}\rangle + z\langle e^{-in\phi}\rangle) \tag{3.27}$$

Comparing it with Eq. (3.25) all cumulants of order higher than 1 vanishes, as it is expected in the case of uncorrelated particles.

The interesting cumulants are the diagonal terms with $k = l$ which are related to the flow. They will be denoted with $c_n\{2k\}$:

$$c_n\{2k\} \equiv \langle\langle e^{in(\phi_1+...+\phi_k-\phi_{k+1}-...-\phi_{2k})}\rangle\rangle \tag{3.28}$$

In practice, it is rather difficult to expand the generating function $\mathcal{C}_n(z)$ analytically beyond the order 2. The simplest way to extract $c_n\{2k\}$ is to compute $G_n(z)$ and then $\mathcal{C}_n(z)$ for various values of $z$ in order to tabulate it. Then one has to interpolate their successive derivatives from the obtained matrix. For example, one way is to use the points:

$$z_{p,q} = x_{p,q} + iy_{p,q}, \tag{3.29}$$

$$x_{p,q} \equiv r_0\sqrt{p}\cos(\frac{2q\pi}{q_{max}}), \tag{3.30}$$

$$y_{p,q} \equiv r_0\sqrt{p}\sin(\frac{2q\pi}{q_{max}}) \tag{3.31}$$

for $p = 1, ..., k_{max}$ and $q = 1, ..., q_{max} - 1$ where $q_{max} > 2k_{max}$. Typical values are $k_{max} = 3$ and $q_{max} = 7$. As one wants to know the behavior of $G_n(z)$ and $\mathcal{C}_n(z)$ near the origin, $r_0$ has to be a small number. Averaging $\mathcal{C}_n(z_{p,q})$ over phase of $z$ one obtains

$$C_p \equiv \frac{1}{q_{max}} \sum_{q=0}^{q_{max}-1} \mathcal{C}_n(z_{p,q}), \qquad\qquad p = 1, ..., k_{max} \tag{3.32}$$

It is shown [45] that $C_p$ is related to the cumulants $c_n\{2k\}$ through the linear system

$$C_p = \sum_{k=1}^{k_i} \frac{(r_0\sqrt{p})^{2k}}{(k!)^2} c_n\{2k\} \tag{3.33}$$

which can be resolved in order to extract the cumulants. With $k_i = 3$ it gives

$$c_n\{2\} = \frac{1}{r_0^2}(3C_1 - \frac{3}{2}C_2 + \frac{1}{3}C_3) \tag{3.34}$$

$$c_n\{4\} = \frac{2}{r_0^4}(-5C_1 + 4C_2 - C_3) \tag{3.35}$$

$$c_n\{6\} = \frac{6}{r_0^6}(3C_1 - 3C_2 + C_3) \tag{3.36}$$

The relations between the cumulants $c_n\{2k\}$ and the integrated flow $V_n$, or to be more precise their estimates $V_n\{2k\}$ are given by

$$V_n\{2\}^2 = c_n\{2\}, \tag{3.37}$$

$$V_n\{4\}^4 = -c_n\{4\}, \tag{3.38}$$

$$V_n\{6\}^6 = \frac{c_n\{6\}}{4} \tag{3.39}$$

### Statistical Errors

Due to the finite number of events $N$, the reconstructed integrated flow has a statistical fluctuation which could be calculated from the covariance matrices $\langle V_n\{2k\}V_n\{2l\}\rangle - \langle V_n\{2k\}\rangle\langle V_n\{2l\}\rangle$. The covariance matrices contain information on the standard error.

In [45] it is shown that in the case of a huge flow, i.e., $V_n \gg 1/\sqrt{M}$, the following equation is valid

$$\langle V_n\{2k\}V_n\{2l\}\rangle - \langle V_n\{2k\}\rangle\langle V_n\{2l\}\rangle = \frac{1}{2MN} \tag{3.40}$$

In this limit, reconstructed flow from different cumulant orders coincide and the error is $1/\sqrt{2MN}$ independently of $k$. This is easy to understand: when flow is large compared to $1/\sqrt{M}$ the reaction plane can be reconstructed with a high accuracy.

In the general case, when $V_n$ and $1/\sqrt{M}$ are of the same order of magnitude the statistical deviations are given by

$$\begin{aligned}(\delta V_n\{2\})^2 &= \frac{1}{2MN}\frac{1+2\chi^2}{2\chi^2}\\ (\delta V_n\{4\})^2 &= \frac{1}{2MN}\frac{1+4\chi^2+\chi^4+2\chi^6}{2\chi^6}\\ (\delta V_n\{6\})^2 &= \frac{1}{2MN}\frac{3+18\chi^2+9\chi^4+28\chi^6+12\chi^8+24\chi^{10}}{24\chi^{10}}\end{aligned} \tag{3.41}$$

where $(\delta V_n\{2k\})^2 = \langle V_n\{2k\}^2\rangle - \langle V_n\{2k\}\rangle^2$ and $\chi^2 \equiv MV_n^2$. In the limit of a very large flow ($\chi \gg 1$) all three equations reduce to Eq. (3.40).

In the case of a very weak flow, i.e., $V_n \ll 1/\sqrt{M}$, different estimates of $V_n$ are uncorrelated, and hence flow cannot be reconstructed and statistical errors loose their sense.

### 3.5.2 Differential Flow

When the integrated (over phase space) flow values $V_n\{2k\}$ are known, one can measure the ”differential flow”, i.e. flow value in a narrower phase space window. Following the notation in [45], let’s call a particle belonging to the given narrower window a ’proton’ (although it can be anything else). It’s azimuthal angle is denoted with $\psi$, and it’s differential flow as $v_n(p_T, y) = \langle e^{in(\psi-\Phi)}\rangle$. The particles used for the integrated flow $V_n$ are ’pions’. Once the integrated flow $V_n$ is known, one can reconstruct the differential flow $v_n$ from the correlations between the azimuth $\psi$ and ’pion’ azimuths $\phi_j$. In order to do that, first one constructs a generating function between the ’proton’ and ’pions’. This function is the average value over all ’protons’ of $e^{ip\psi}G_n(z)$, where $G_n(z)$ is defined with Eq. (3.22) evaluated for the event to whom the ’proton’ belongs. Note that the average procedure is not exactly the same as in the case of the integrated flow. One must first average over ’protons’ in the same event (i.e. with the same $G_n(z)$) and then to average over only those events where there are ’protons’.

Expanding in power series of $z$ and $z^\star$, one obtains:

$$\langle e^{ip\psi}G_n(z)\rangle = \langle e^{ip\psi}\rangle + z\langle e^{i(p\psi-n\phi_1)}\rangle + z^\star\langle e^{i(p\psi+n\phi_1)}\rangle + \ldots \tag{3.42}$$

which generates azimuthal correlations between the ’proton’ and arbitrary number of ’pions’. The generating function is then

$$\mathcal{D}_{p/n}(z) \equiv \frac{\langle e^{ip\psi}G_n(z)\rangle}{\langle G_n(z)\rangle} \tag{3.43}$$

Note that the 'proton' should not be one of the 'pions' in order to avoid of autocorrelations, and while the number of 'pions' in Eq. (3.22) is fixed, the number of 'protons' is allowed to fluctuate from event to event.

The cumulants are, by definition, the coefficients in the power series of the generating function, i.e.

$$\mathcal{D}_{p/n}(z) \equiv \sum_{k,l} \frac{z^{\star k} z^l}{k!l!} \langle\langle e^{ip\psi + in(\phi_1 + \ldots + \phi_k - \phi_{k+1} - \ldots - \phi_{k+l})}\rangle\rangle \tag{3.44}$$

The physical meaning of these cumulants is the same as in the case of the integrated flow. They eliminate the detector effects and the lower order non-flow correlations, so only the direct (non-flow) correlations of order $M^{-k-l}$ remain.

If the 'proton' is not correlated with the 'pions', then Eq. (3.43) become $\mathcal{D}_{p/n}(z) = \langle e^{ip\psi}\rangle$ for any $z$ and all cumulants are vanishing. In the case when the correlation is present, expanding Eq. (3.43) up to order $z$ and comparing to Eq. (3.44) one obtains

$$\langle\langle e^{i(p\psi - n\phi_1)}\rangle\rangle \equiv \langle e^{i(p\psi - n\phi_1)}\rangle - \langle e^{ip\psi}\rangle\langle e^{in\phi_1}\rangle \tag{3.45}$$

what is analogous to Eq. (3.19) and has the same interpretation, namely that the cumulant method gives exactly the same result as the two-particle correlations.

In the case of a perfect detector all cumulants defined in Eq. (3.44) are real, because reversing the sign of all azimuthal angles $\psi \to -\psi, \phi_j \to -\phi_j$ leaving $\mathcal{D}_{p/n}(z)$ unchanged. Also the transformation $\phi_j \to -\phi_j$ changes $z$ into $z^\star$ in $G_n(z)$, so

$$\mathcal{D}_{p/n}(z) \equiv \frac{\langle e^{-ip\psi} G_n(z^\star)\rangle}{\langle G_n(z^\star)\rangle} \tag{3.46}$$

Comparing it with Eq. (3.43) one sees that $z$ has been changed into $z^\star$ and $\psi$ into $-\psi$. Since $G_n(z)$ is a real function one finally obtains $\mathcal{D}_{p/n}(z) = \mathcal{D}^\star_{p/n}(z^\star)$. From that one concludes that the coefficients in Eq. (3.44) are real. In the case of a real detector, they are complex, but only the real part has a physical meaning. Writing $p = mn$ the relevant quantities are:

$$d_{mn/n}\{2k + m + 1\} \equiv \mathcal{R}e[\langle\langle e^{in(m\psi + \phi_1 + \ldots + \phi_k - \phi_{k+1} - \ldots - \phi_{2k+m})}\rangle\rangle] \tag{3.47}$$

where $\mathcal{R}e$ denotes the real part, and $\{2k + m + 1\}$ denotes correlations between one 'proton' and $2k+m$ 'pions'. The cumulant $d_{mn/n}\{2k+m+1\}$ has a contribution from flow proportional to $v_p V_n^{2k+m}$. In that way one can calculate the differential flow $v_p$ from the cumulant $d_{mn/n}\{2k+m+1\}$ knowing a previously calculated value of the integrated flow $V_n$. In order to avoid the trivial autocorrelation effect, the 'proton' must not be one of the 'pions'. The same problem is well known in the Standard Flow Analysis where the way to exclude it was to reject the particle under the study (in this case the 'proton') from the definition of the sums (Eq. (3.4)) which were used for the reaction plane reconstruction. In the method of cumulants one simply removes the 'proton''s contribution by dividing $G_n(z)$ with $1 + (z^\star e^{in\psi} + ze^{-in\psi})/M$ in the numerator of the Eq. (3.43). As in the case of the integrated flow, a practical way to determine the differential flow consists in tabulating the generating function $\mathcal{D}_{p/n}(z)$ at the 'pions' $z_{p,q}$ given by Eq. (3.29)

$$D_p \equiv \frac{(r_0\sqrt{p})^m}{q_{max}} \sum_{q=0}^{q_{max}-1} [\cos(m\frac{2q\pi}{q_{max}})X_{p,q} + \sin(m\frac{2q\pi}{q_{max}})Y_{p,q}] \tag{3.48}$$

with

$$\begin{aligned} X_{p,q} + iY_{p,q} \equiv \mathcal{D}_{p/n}(z_{p,q}) = & \frac{\frac{1}{N'}\sum_{ev.w.prot.}[\sum_{prot.}\cos(p\psi)G_n(z)_{p,q}]}{\frac{1}{N_{evts}}\sum_{evts} G_n(z_{p,q})} + \\ & + i\frac{\frac{1}{N'}\sum_{ev.w.prot.}[\sum_{prot.}\sin(p\psi)G_n(z)_{p,q}]}{\frac{1}{N_{evts}}\sum_{evts} G_n(z_{p,q})} \end{aligned} \tag{3.49}$$

where $N'$ is the total number of 'protons'. There is a relation between the cumulant $d_{mn/n}\{2k+m+1\}$ and numbers $D_p$ via the system:

$$D_p = \sum_{k=0}^{k_d-1} \frac{(r_0\sqrt{p})^{2k+m}}{k!(k+m)!} d_{p/n}\{2k+m+1\}, \qquad 1 \leq p \leq k_d \tag{3.50}$$

which can be solved in cumulants $d_{p/n}\{2k+m+1\}$. For instance, with $k_d = 2$ and $m = 1$ which is used for $v_{1/1}$ and $v_{2/2}$, one has:

$$d_{n/n}\{2\} = \frac{1}{r_0^2}(2D_1 - \frac{1}{2}D_2) \tag{3.51}$$

$$d_{n/n}\{4\} = \frac{1}{r_0^4}(-2D_1 + D_2) \tag{3.52}$$

while for $k_d = 2$ and $m = 2$ is used to calculate $v_{2/1}$,

$$d_{2n/n}\{3\} = \frac{1}{r_0^4}(4D_1 - \frac{1}{2}D_2) \tag{3.53}$$

$$d_{2n/n}\{5\} = \frac{1}{r_0^6}(-6D_1 + \frac{3}{2}D_2) \tag{3.54}$$

When the cumulants are determined in that way, then they must be related to the differential flow $v_{mn/n}$. In the case of a perfect detector following equations are valid

$$v_{n/n}\{2\} = \frac{d_{n/n}\{2\}}{V_n} \tag{3.55}$$

$$v_{n/n}\{4\} = -\frac{d_{n/n}\{4\}}{V_n^3} \tag{3.56}$$

$$v_{2n/n}\{3\} = \frac{d_{2n/n}\{3\}}{V_n^2} \tag{3.57}$$

$$v_{2n/n}\{5\} = -\frac{d_{2n/n}\{5\}}{2V_n^4} \tag{3.58}$$

### Statistical Errors

Although, as in the case of the integrated flow, the reconstructed differential flow depends on the number of events $N_{evts}$ (denominator in Eq. (3.49)), this depends additionally on the number of 'protons' $N'$ (numerator in Eq. (3.49)) in a narrow phase-space window where it is measured. Hence, one can neglect the contribution from the denominator to the statistical error of the differential flow.

Again, in the case of the weak flow, i.e., $v_n \ll 1/\sqrt{M}$, correlations between the estimations from the different orders vanish and the statistical errors loose their sense. When $v_n \gg 1/\sqrt{M}$ (large flow), covariance matrix reduces to

$$\begin{aligned}\langle v_{mn/n}\{2k+m+1\} v_{mn/n}\{2l+m+1\}\rangle &- \\ \langle v_{mn/n}\{2k+m+1\}\rangle\langle v_{mn/n}\{2l+m+1\}\rangle &= \frac{1}{2N'}\end{aligned} \tag{3.59}$$

In the general case, when $v_n$ and $1/\sqrt{M}$ are of the same order of magnitude, the following equations are valid. For $m = 1$:

$$\langle v_{n/n}\{2\}^2\rangle - \langle v_{n/n}\{2\}\rangle^2 = \frac{1}{2N'}\frac{1+\chi^2}{\chi^2} \tag{3.60}$$

$$\langle v_{n/n}\{2\} v_{n/n}\{4\}\rangle - \langle v_{n/n}\{2\}\rangle\langle v_{n/n}\{4\}\rangle = \frac{1}{2N'} \tag{3.61}$$

$$\langle v_{n/n}\{4\}^2\rangle - \langle v_{n/n}\{4\}\rangle^2 = \frac{1}{2N'}\frac{2+6\chi^2+\chi^4+\chi^6}{\chi^6} \tag{3.62}$$

where $\chi^2 \equiv M v_n^2$. For $m = 2$:

$$\langle v_{2n/n}\{3\}^2\rangle - \langle v_{2n/n}\{3\}\rangle^2 = \frac{1}{2N'}\frac{2+4\chi^2+\chi^4}{\chi^4} \tag{3.63}$$

$$\langle v_{2n/n}\{3\} v_{2n/n}\{5\}\rangle - \langle v_{2n/n}\{3\}\rangle\langle v_{2n/n}\{5\}\rangle = \frac{1}{2N'}\frac{3+\chi^2}{\chi^2} \tag{3.64}$$

$$\langle v_{2n/n}\{5\}^2\rangle - \langle v_{2n/n}\{5\}\rangle^2 = \frac{1}{2N'}\frac{6+24\chi^2+9\chi^4+10\chi^6+4\chi^8}{4\chi^8} \tag{3.65}$$

In the limit of very large flow ($\chi \gg 1$) all six equations reduce to Eq. (3.59).

## 3.6 The Lee-Yang Zeroes

The Lee-Yang zeroes method [46, 47] derived by J.-Y. Ollitrault, N. Borghini and R.S. Bhalerao is based on the genuine correlation between a large number of particles. It is more natural and more reliable than all other methods which have been used so far. Since the anisotropic flow appears as a collective effect, involving all particles produced in an event, it is indeed natural to characterize it by means of a global multiparticle observable. All previously used methods were practically based on $2k$-particle correlations (where $2k \ll M$) and so they are not the appropriate tool to probe a collective behavior. Especially, in all these methods, except the cumulant method, non-flow effects were neglected.

### 3.6.1 Integrated Flow

In order to measure genuine anisotropic flow one first defines the integrated flow as

$$V_n = \langle \sum_{j=1}^{M} w_j \cos[n(\phi_j - \Phi)] \rangle \tag{3.66}$$

where the sum goes over all particles detected in an event and $w_j$ are appropriate weights. In the Eq. (3.66) $\Phi$ is the azimuth of the impact parameter vector $\vec{b}$. The integrated flow is connected with an average of the Fourier coefficient $v_n$ via: $V_n = M_w v_n$, where $M_w = \sum_{j=1}^{M} w_j$.

In order to compute the integrated flow one has to compute for each event the complex-valued function:

$$g^{\theta}(ir) = \prod_{j=1}^{M} [1 + irw_j \cos(n(\phi_j - \theta)] \tag{3.67}$$

for various values of the real positive variable $r$ and of the angle $\theta$ ($0 \leq \theta \leq \pi/n$) [3]. The $\phi_j$ is the measured laboratory azimuthal angle of a particle and the product goes over all detected particles.

Then, one has to average $g^{\theta}(ir)$ over events for each value of $r$ and $\theta$:

$$G^{\theta}(ir) \equiv \langle g^{\theta}(ir) \rangle = \frac{1}{N} \sum_{events} g^{\theta}(ir) \tag{3.68}$$

where $N$ is the number of events used in the analysis. For each $\theta$, the position of $r_0^{\theta}$ of the first minimum of the modulus $|G^{\theta}(ir)|$ has to be found. Then the estimate of the integrated flow $V_n$ is given by:

$$V_n^{\theta}\{\infty\} \equiv \frac{j_{01}}{r_0^{\theta}} \tag{3.69}$$

where $j_{01} \approx 2.40483$ is the first zero of the Bessel function $J_0$. If the distribution of the laboratory azimuthal angle is rather flat, then $V_n^{\theta}\{\infty\}$ does not depend on $\theta$ up to the statistical fluctuations. Then one can perform an averaging of $V_n^{\theta}\{\infty\}$ over $\theta$ which gives $V_n\{\infty\}$ with smaller statistical error. That quantity is then used to calculate the resolution parameter $\chi$. The resolution parameter is defined as: $\chi = V_n\{\infty\}/\sigma$ and it measures the relative strength of the integrated flow with respect to the finite multiplicity fluctuations $\sigma$ which is given by

$$\sigma = \sqrt{\langle Q_x^2 + Q_y^2 \rangle - \langle Q_x \rangle^2 - \langle Q_y \rangle^2 - V_n\{\infty\}^2} \tag{3.70}$$

In the above formula, $Q_x$ and $Q_y$ are defined as

$$Q_x = \sum_{j=1}^{M} w_j \cos(n\phi_j), \qquad Q_y = \sum_{j=1}^{M} w_j \sin(n\phi_j) \tag{3.71}$$

---

[3] In practice, 4 equally spaced values of $\theta$ are enough

and $\langle\rangle$ means the averaging over many events.

The finite number of the available events makes the relative statistical error on $V_n\{\infty\}$ finite. That statistical error is given by

$$\frac{\langle(\Delta V_n\{\infty\})^2\rangle}{(V_n\{\infty\})^2} = \frac{1}{2Nj_{01}^2 J_1(j_{01})^2}\left[e^{\frac{j_{01}^2}{2\chi^2}} + e^{-\frac{j_{01}^2}{2\chi^2}} J_0(2j_{01})\right] \tag{3.72}$$

### 3.6.2 Differential Flow

When an estimation of the integrated flow is obtained, one can use it in order to calculate the differential flow. As in the case of the cumulant analysis, the differential flow is flow of particles of a given kind in a definite phase-space region, which will be again called 'protons' for the sake of brevity. Azimuthal angle of such a 'proton' will be denoted with $\psi$ and the corresponding differential flow with $v_n(p_T, y)$. For the given angle $\theta$, calculated $V_n^\theta\{\infty\}$ and $r_0^\theta$ determined in a way how it was described in the previous section, an estimation of $v_n^\theta\{\infty\}$ is given by

$$v_n^\theta\{\infty\} = V_n^\theta\{\infty\}\frac{J_1(j_{01})}{J_n(j_{01})}\mathcal{R}e\left(\frac{\langle g^\theta(ir_0^\theta)\frac{\cos(n(\psi-\theta))}{1+ir_0^\theta w_\psi \cos(n(\psi-\theta))}\rangle_\theta}{\langle g^\theta(ir_0^\theta)\sum_j \frac{w_j \cos(n(\phi_j-\theta))}{1+ir_0^\theta w_j \cos(n(\phi_j-\theta))}\rangle_{evts}\rangle}\right) \tag{3.73}$$

In the denominator sum is over all detected particles in the given event averaged over events. The average $\langle ... \rangle_\psi$ in the numerator is over "protons", and varies from one "proton" to the other, even for "protons" within the same event.

Denoting with $N$ the total number of "protons" in the (differential) phase-space window under study, the statistical error on the $v_n^\theta\{\infty\}$ is given by

$$\langle(\delta v_n^\theta\{\infty\})^2\rangle = \frac{1}{4N' J_n(j_{01})^2}[e^{j_{01}^2/2\chi^2} + (-1)^n e^{-j_{01}^2/2\chi^2} J_0(2j_{01})] \tag{3.74}$$

Averaging over $v_n^\theta\{\infty\}$ for different $\theta$ values results in a new $v_n\{\infty\}$ with a smaller statistical error. Statistical fluctuations could produce a spurious flow even there when real flow does not exist. These fluctuations could produce a minimum of $|G_n(z)|$ and corresponding spurious flow satisfy the following non-equality

$$v_n^\theta \leq \frac{j_{01}}{\sqrt{2MlnN}} \tag{3.75}$$

where $N$ is the total number of events and $M$ is the multiplicity. From (3.75) is obvious that if flow is too small even with a huge statistics ($N$) due to the logarithmic dependence it is impossible to measure the flow. This is the main limitation of the method of Lee-Yang Zeroes: $v_n$ can be successfully determined only if it is larger then r.-h.s. of (3.75). The main advantage of the method is that it is stable against the effects like multiple hits or showering, which strongly bias the results of other methods. So, one should not refrain from using all detected particles and combining information from different detectors: increasing the multiplicity results in a smaller statistical error on the flow estimation.

## 3.7 The Method Used in this Analysis

In this thesis due to the rather small magnitude of the elliptic flow it was difficult to apply the method of cumulants and the Lee-Yang zeroes method. Another problem which caused inapplicability of the two above mentioned sofisticated methods was an insufficient statistics. These statements are a consequence of Eq. (3.41) and (3.75)[4]. . So the reaction plane method, described in Section 3.4, was applied in the analysis of the experimental data. In Chapter 5 will be given more details concerning the selection of the method which is going to be applied in the analysis of the experimental data.

---

[4] The cumulant method was applied successfully in [55] but for semicentral collisions where the magnitude of $v_2$ is enough big. Similarly, due to the huge magnitude of the directed flow $v_1$ the Lee-Yang Zero method was applied in [59]

# Chapter 4

# EXPERIMENTAL SETUP AND DATA USED

In this Chapter the CERES experimental setup will be presented. A special attention will be devoted to the description of those detectors features which are especially important for the measurements of the momentum anisotropy. In the Section 4.2, the calibration of the raw data will be shortly presented. The ballistic deficit correction and the efficiency of silicon detectors in which I was personally involved will be explained in detail. A short presentation of data used in the analysis of the anisotropic transverse flow in the CERES experiment is the contents of the Section 4.3. The last Section of this Chapter concerns the centrality determination.

## 4.1 The CERES Experimental Setup

The main goal of the CERES/NA45 experiment is the measurement of low-mass $e^+e^-$ pairs produced in heavy-ion collisions at SPS energies. The experimental setup, shown in Fig. 4.1, consists out of the target system, two radial Silicon Drift Detectors (SDD), two Ring Imaging CHerenkov (RICH) detectors and a cylindrical Time Projection Chamber (TPC) with a radial drift field. With older experimental setups (without the TPC), the measurement of low-mass $e^+e^-$ pairs produced in Pb+Au collisions at the top SPS energy showed a significant enhancement compared to the contributions originating from the hadronic decays [60]. The new experimental setup, upgraded with the TPC, achieved a mass resolution of $\delta m/m \approx 3.8\%$ at $m \approx 1GeV/c^2$ which additionally allowed distinction between different models of in-medium modification and spectroscopy of $\phi$ mesons [5, 61]. Although designed for the measurement of low-mass $e^+e^-$ pairs, the CERES experimental setup has abilities to detect charged particles and measure their momenta. Hence, allows performing of various 'hadronic analyses' like identical, non-identical, two and multiparticle correlations, fluctuations, reconstruction of different particle species like $\Lambda$, $K^0_S$, $\phi$ and etc., and flow and jet physics.

### 4.1.1 The Target and the Beam/Trigger Detectors

During the last data taking period (the year 2000), 13 golden disks with a diameter of $600\mu$m and a thickness of $25\mu$m were used as a target system. The distance of 1.98 mm between them was chosen in order that particles produced in a collision will not travel through other disks before they reach the detector system. For the electron analysis this is important because in that way the conversion of photons into $e^+e^-$ pairs is suppressed.

A system of different beam/trigger detectors, located in the beam line before and after the target was used to detect the occurrence of a collision [62]. If any kind of collision happened, the trigger condition is called *minimum bias*. The collisions could be characterized via the value of the impact parameter. There is no way to measure it directly, but that variable is correlated with the multiplicity. Since many physical variables strongly depend on the impact parameter, the multiplicity had to be measured in some way. In CERES, as in many other heavy-ion experiments, only charged multiplicity is measured which also can be connected with the impact parameter. The Multiplicity Counter (MC) was used to fulfill that purpose. The MC is a scintillation detector.

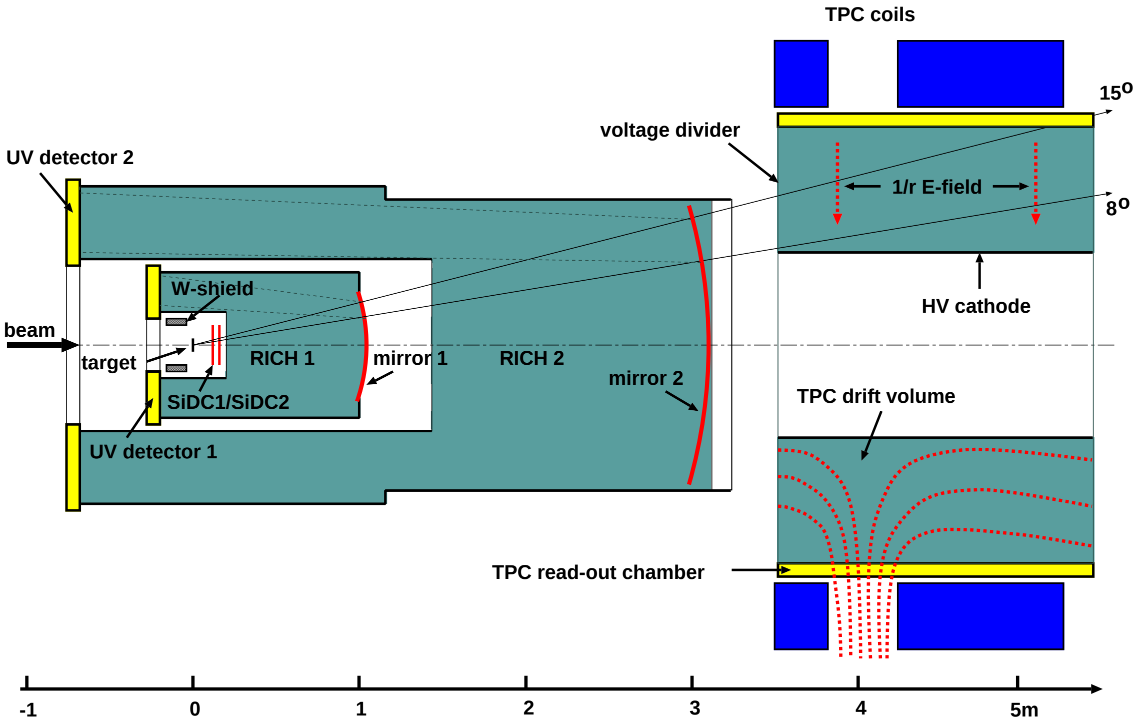

**Figure 4.1:** The CERES/NA45 experimental setup in year 2000 the data taking period.

### 4.1.2 The Silicon Drift Detectors

The SDDs as 4 inch silicon wafers with a thickness of 280 $\mu m$ are located approximately 10 cm behind the target. They have $2\pi$ azimuthal acceptance and cover the pseudorapidity region between approximately 1.6 and 3.4. That overlaps the central rapidity region which is very interesting for the elliptic flow measurement. The high resolution of these detectors is used for the reconstruction of the position of the interaction vertex. The SDDs were also used for the centrality determination. Together with the TPC they were used as the tracking devices also. The precise determination of the primary vertex position and a precise reconstruction of the tracks is very important in performing a flow analysis, as well as a good enough centrality determination.

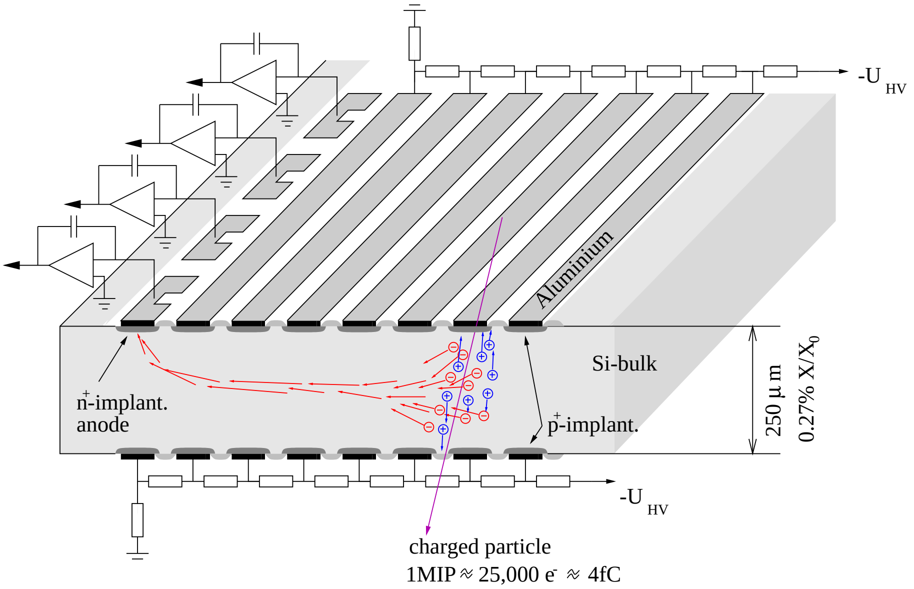

**Figure 4.2:** The Silicon Drift Detectors operate on base of electrons drifting in a radially symmetric electric field towards the edge of the detectors.

Fig. 4.2 shows the working principle of the SDD. The SDDs work in the following principle. When a charged particle passes the detector it creates electron-hole pairs along its trajectory. In a radially symmetric electric field, created electrons drift towards the outside edge of the detector. The edge of the SDD is divided into 360 anodes which are reading out the signal. Knowing the drift time (typically around $3.8\mu s$) it is possible to reconstruct the hit position in the radial direction. Then from the exact position of the given SDD it is possible to obtain the polar angle $\theta$ of the hit. The $\phi$ position of the hit is obtained via knowing the anode at which the signal is received. The precise measurement of $\phi$ and $\theta$ is determined from the center of gravity of the corresponding

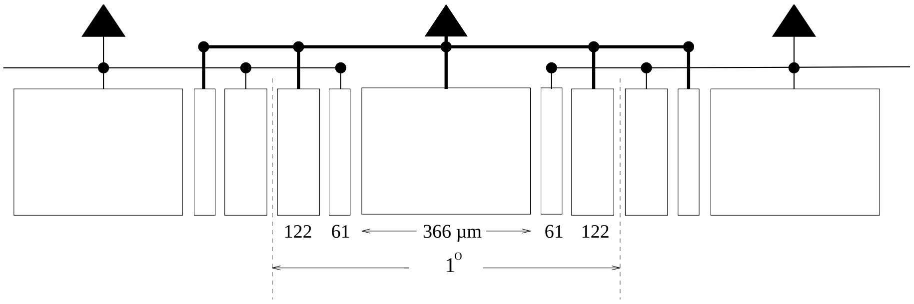

**Figure 4.3:** An interlaced structure of the anode divided into 5 pieces.

charge distributions shared by adjacent time bins and anodes. The high precision in the measurement of $\phi$ is achieved using anodes with an interlaced structure shown in Fig. 4.3. For more details see [63, 64].

### 4.1.3 The RICH Detectors

The purpose of the two RICH detectors, placed behind the SDDs, is electron identification. The working principle of the RICH detector, proposed in [65], is the following. A particle created in the collision emits Cherenkov photons under a constant angle $\theta_C$ with respect to the trajectory of the particle. The relation between the refraction index $n$, particle's velocity $\beta$ and Cherenkov angle $\theta_C$ is given by $\theta_C = \arccos(1/\beta n)$. From the previous relation is obvious that Cherenkov radiation can happen only if $\beta > 1/n$. The emitted photons are reflected from the mirror and form a ring image at the mirror's focal plane. The diameter of the ring corresponds to a certain Cherenkov angle and hence to a certain velocity of the particle. The photons which form the ring are detected at the plane and the signal, after amplification, is read out on 50000 individual pads covering the geometrical acceptance. A complete description of the RICH detectors can be found in [66–68]. The information obtained from the RICH detectors was not used in this analysis.

### 4.1.4 The Time Projection Chamber

The main aim of upgrading the CERES experimental setup with the TPC was to achieve an enough high mass resolution at the intermediate mass region in order to study $\rho/\omega$ and to perform a spectroscopy of $\phi$ mesons. The TPC was designed according to the neediness of preservation of the azimuthal symmetry and matching the acceptance in pseudorapidity roughly between 2.0 and 2.7. The perspective view of the CERES TPC is shown in Fig. 4.4. It is a cylindrical drift chamber with a radial drift field and segmented pad-readout. The length of the TPC is 2 m and the sensitive volume of about 9 m$^3$. 16 readout chambers are distributed in a polygonal structure around the inner electrode with diameter of 0.972 m. In total there are 15360 individual channels. Each of them has 256 time bins. The z-axis of the TPC, which coincides with the beam axis, is divided into 20 planes. Each of them has $16 \times 48 = 768$ readout channels. The TPC was placed inside a $\vec{B}$ field.

The electric field is defined by the inner electrode at a potential of $\sim -30$ kV and the cathode wires of the readout chambers at ground potential. Such electric field shows roughly a $1/r$ dependence. With drift velocities between 2.4 and 0.7 cm/$\mu$s the maximum drift time is about 71 $\mu$s.

The magnetic field is generated by two warm coils with the electric currents floating in the opposite directions. The radial component of the magnetic field is maximal between the coils and it deflect charged particles mainly in the azimuthal direction. The mean value of the magnetic field integral is $0.18$ Tm at $\theta = 8°$ and $0.38$ Tm at $\theta = 15°$.

With such a performance, the TPC allows a precise measurement of a hit position determined by radius $r$, azimuthal angle $\phi$ and polar angle $\theta$ in a coordinate system where the z-axis of the TPC coincides with the beam direction. Using the reconstructed hits, tracks left by particles which passed the TPC are reconstructed with a high precision. The presence of a magnetic field in the sensitive detection volume leads to curved tracks.

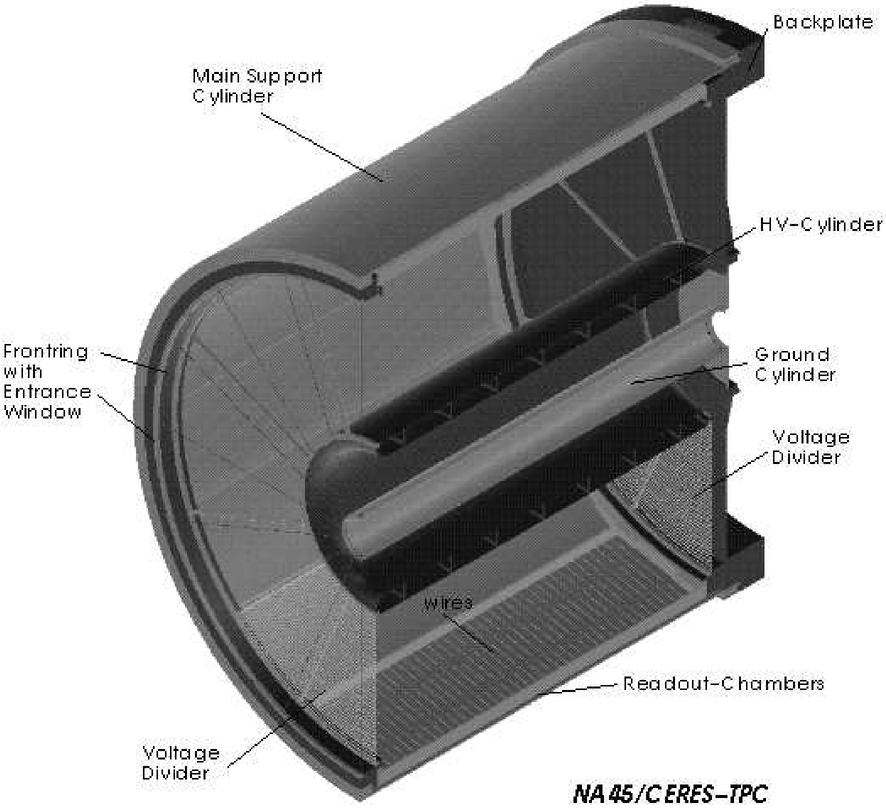

**Figure 4.4:** The cylindrical Time Projection Chamber operates in a radial drift field.

The curvature allows the determination of the sign of the charged particle detected in the TPC. Operating inside a magnetic field, the TPC provides a precise determination of the momentum in a huge range from few tens MeV/c up to more than 20 GeV/c.

A more detailed description of the CERES/NA45 experiment can be found in [69].

## 4.2 The Calibration and Production of Data

In order to do a physics analysis one needs to receive the meaningful information from the detector signals. The raw data, i.e. the data recorded from the detectors are difficult to handle. They are also not calibrated, which means that they are not corrected for the different changes like temperature, gas composition, imperfectness of the detectors and etc. during the data taking. From the raw data via the procedure called *production* measured ADC values obtained from the detector system are transformed into hits. The next step is grouping of hits in order to make tracks. Finally, by fitting tracks, momenta and sign of the charged particles are obtained. The output of the production is stored in shape of files with a ROOT Tree format.

Approximately 30 M events at the highest SPS energy, processed in the production, are used in the anisotropic transverse flow analysis. During the production, the amount of data is significantly reduced. The events are grouped into $\approx 400$ units. Each unit consists out of approximately 200 bursts.

Concerning the calibration of data I was personally involved in the ballistic deficit correction and the efficiency of the SDD. In the next two subsections these topics will be presented in detail.

### 4.2.1 The Ballistic Deficit Correction

The energy loss of $E_{loss}$ in the SDD can be approximated by a Landau distribution [70].

$$\frac{dN}{dEdx} \sim -\exp(\frac{x}{2}+e^{-x}), \qquad x=\frac{E_{loss}-E_{max}}{\sigma} \tag{4.1}$$

where $E_{max}$ and $\sigma$ denote the most probable energy loss and the width of the corresponding distribution. In a SDD detector, the measured number of FADC counts decreases with the radial position of the hit. From the other side, the radial width of the electron cloud increases with the drift time due to the diffusion according to [71]

$$\sigma_r^2(r)=\sigma_{r,r_0}^2+2Dt_{drift}(r) \tag{4.2}$$

where $\sigma_{r,r_0}$ and $D$ are initial radial width of the hit and diffusion constant. Since the

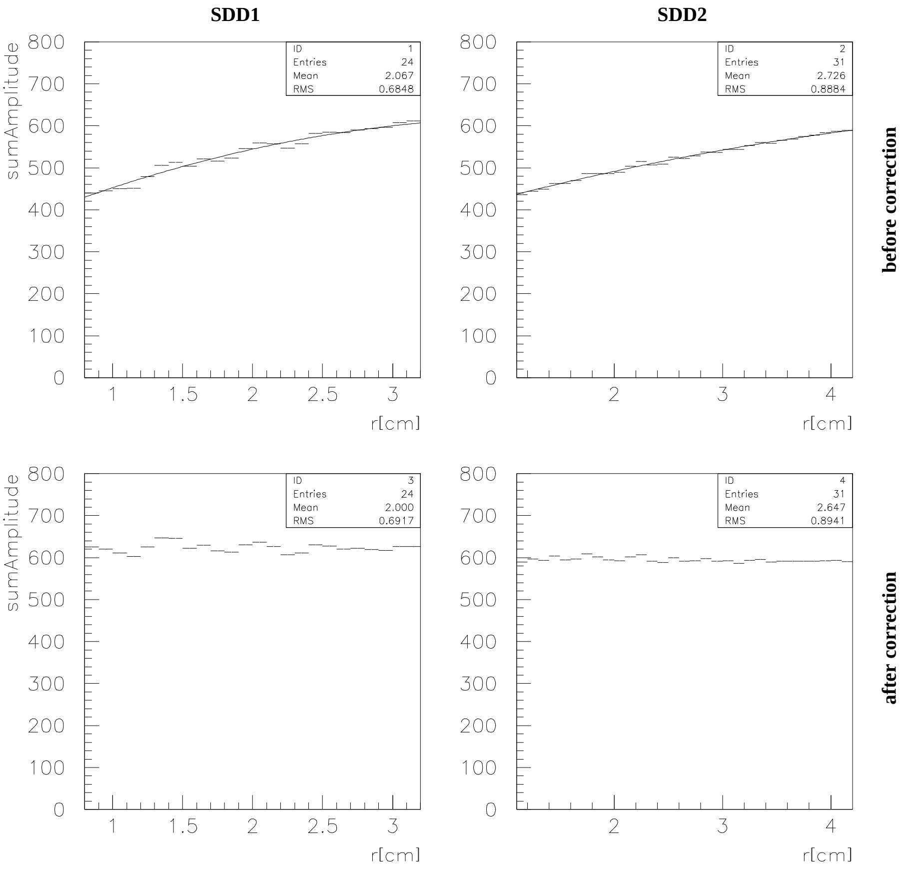

**Figure 4.5:** The ballistic deficit before (top) and after (bottom) the correction in the case of SDD1 (left) and SDD2 (right). Data are fitted with a second order polynom.

response of the SDD depends on the width of the input signal hence the output signal decreases for hits at the lower radius. Such behavior is visible in Fig. 4.5. In that Figure is drawn the sum of amplitudes of the signal *vs* radial distance for both SDD detectors. One can see that before the correction the sum of amplitudes decreases going to smaller values of $r$. This effect is known as the ballistic deficit. After the correction for the ballistic deficit, the distribution of the sum of amplitudes *vs* $r$ becomes flat as it should be.

### 4.2.2 The SDD Efficiency

In order to determine the efficiency of the SDD detector system, a selection of high quality TPC tracks was done. Then, the efficiency of the SDD detector system is defined as a ratio between the number of SDD tracks which are matched, within some window, with the selected 'good' TPC tracks ($N_{SDD}^{match}$) to the number of the selected 'good' TPC tracks ($N_{TPC}^{good}$).

$$\epsilon^{SDD} = \frac{N_{SDD}^{match}}{N_{TPC}^{good}} \tag{4.3}$$

As a selection of 'good' TPC tracks are chosen those TPC tracks which satisfy the high quality criteria listed here below

1. the number of TPC hits has to be bigger than 17 out of 20 possible
2. to have momentum $p$ bigger than $2.0$ GeV/c
3. the polar angle $\theta$ to be between $9^\circ$ and $13^\circ$
4. the measured energy loss $dE/dx$ to be smaller than 250 (81.2% of FP [1])
5. radial distance from the track to the vertex position in the $x - y$ plane had to be smaller than $0.6$ cm. In that way a huge part of non-vertex tracks is eliminated

In that way only a small fraction of TPC tracks are extracted and used as 'good' TPC tracks.

SDD track segments are constructed by connecting the vertex point to the hits in SDD2. A track segment is accepted if there is at least one hit in SDD1 within a predefined window around the point of intersection. The sizes of the fiducial windows are expressed as multiples of the *rms* widths of the corresponding distributions in $r$ and $\phi$ direction. Quantitatively, the normalized squared distance between the closest hits in SDD1 and SDD2 is calculated according to formula

$$d^2 = \frac{dr^2}{R_{win}^2} + \frac{d\phi^2}{\phi_{win}^2} \tag{4.4}$$

where $R_{win}$ and $\phi_{win}$ define a $5\sigma_{match}$ window in which the matching is performed. The maximal value of $d^2$ has to be smaller than 1. The closest hits in SDD1 and SDD2 then define the SDD track segment used for the matching to the 'good' TPC tracks.

---

[1] where FP stands for the Fermi plateau

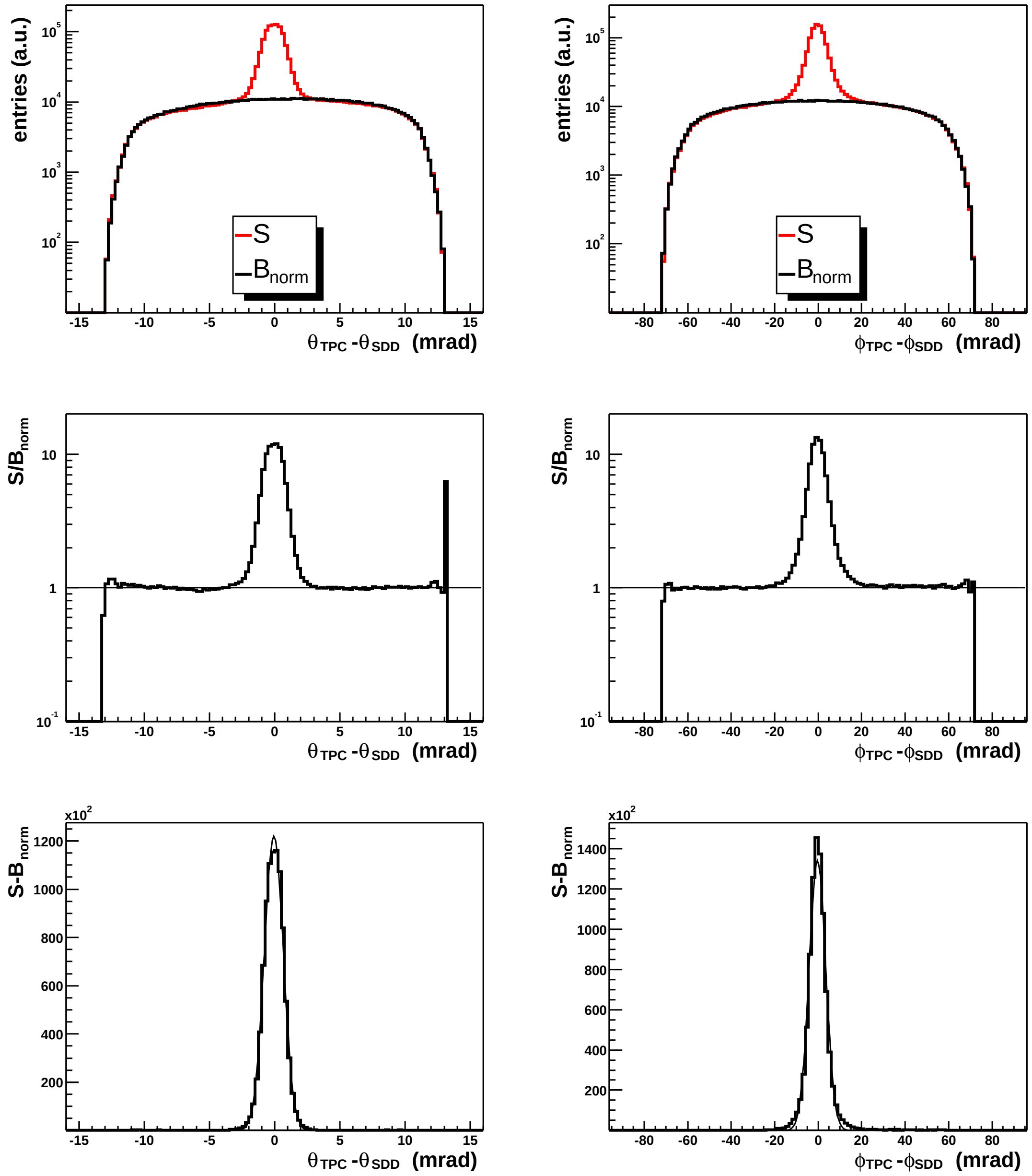

**Figure 4.6:** Top: The signal (S) and normalized combinatorial background ($B_{norm}$) of matched SDD tracks to the referent TPC track in $\theta$ (left) and $\phi$ (right) direction. Middle: The ratio between the signal and normalized combinatorial background. Bottom: The difference between the signal and normalized combinatorial background.

In order to calculate the efficiency one can construct the distributions of number of SDD tracks matched to a TPC track *vs* the difference in $\theta$ or $\phi$ direction between the TPC track and the SDD tracks. Such distributions are made for all 'good' TPC tracks over many events. In Fig. 4.6 (top) are shown such distributions *vs* the difference in $\theta$ or $\phi$ direction depicted with a red line. Among the real matches which are represented with a peak positioned at zero could appear the fake matches between a SDD and a TPC track. These fake matches correspond to entries with $|\theta_{TPC} - \theta_{SDD}| > 4$ mrad and $|\phi_{TPC} - \phi_{SDD}| > 20$ mrad as well as to entries underneath the peak. In order to get the pure signal, these fake matches have to be removed. One way is to rotate for a random angle all TPC tracks around the beam axis and to repeat the procedure for making the signal distribution. In that way all real matches are destroyed and only fake matches can survive. This distribution is shown with a black histogram in Fig. 4.6 (top). In the middle of the Fig. 4.6 is shown the ratio between the signal and the normalized combinatorial background. In the region of fake matches it has the value 1 what means that the normalization is done in a proper way. Then the subtraction of the normalized combinatorial background from the signal distribution in order to get the pure signal can be performed. The corresponding distributions are shown at the bottom part of the Fig. 4.6. In both $\theta$ and $\phi$ direction they have a nice Gaussian shape. Fitting it, one can find the number of real matches and then to calculate the efficiency.

**Table 4.1:** The Gaussian width value of the pure signal distribution in $\theta$ and $\phi$ direction.

| $\sigma_{\Delta\theta}$ [mrad] | $\sigma_{\Delta\phi}$ [mrad] |
|---|---|
| $0.73$ | $3.83$ |

The Table 4.1 shows the Gaussian width value of the pure signal distribution in $\theta$ and $\phi$ direction. The smaller value in $\theta$ direction with respect to the one in $\phi$ direction is a consequence of the fact that the determination of the position of the track in radial direction is better than in azimuthal direction for a factor roughly equal to $1/\sin\theta$.

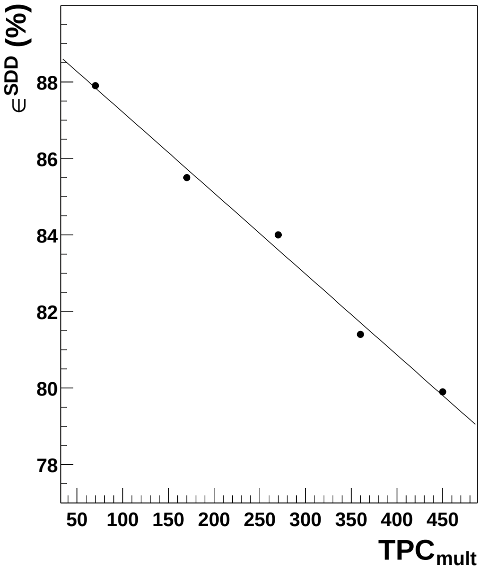

**Figure 4.7:** The SDD efficiency *vs* centrality expressed in the TPC multiplicity.

Fig. 4.7 shows the obtained values for the SDD efficiency applying a matching window with $R_{win} = 0.03$ cm and $\phi_{win} = 0.02$ rad between SDD1 and SDD2. The SDD efficiency is not 100% and it shows a centrality dependence. For the peripheral events where the population of SDD tracks is not big, a huge part (88%) of SDD tracks are matched to the corresponding TPC tracks. Going from the peripheral to the more central collisions, the population of SDD tracks becomes bigger and hence the efficiency decreases. For the most central events, the SDD efficiency is 80%. In order to get 100% efficiency of the SDD detector system, a matching window between SDD1 and SDD2 was optimized. That requirement was achieved applying a matching window with $R_{win} = 0.051$ cm and $\phi_{win} = 0.04$ rad.

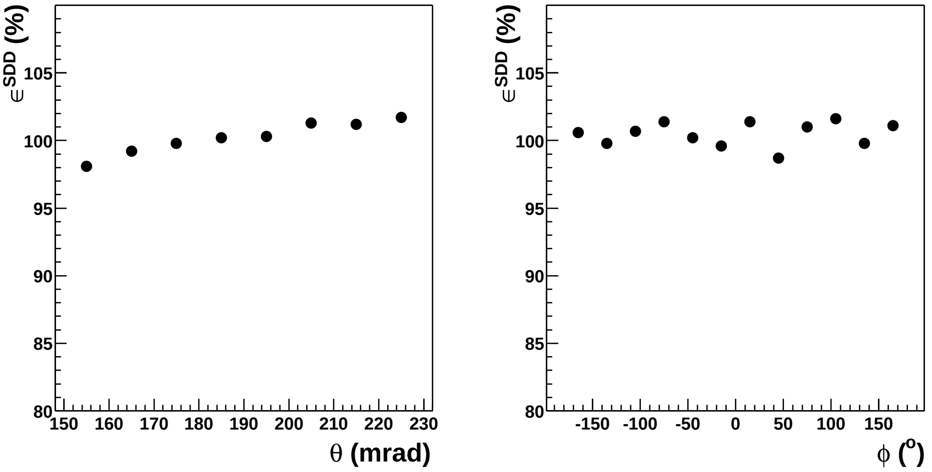

**Figure 4.8:** The efficiency $\epsilon^{SDD}$ *vs* polar ($\theta$) and laboratory azimuthal angle ($\phi$).

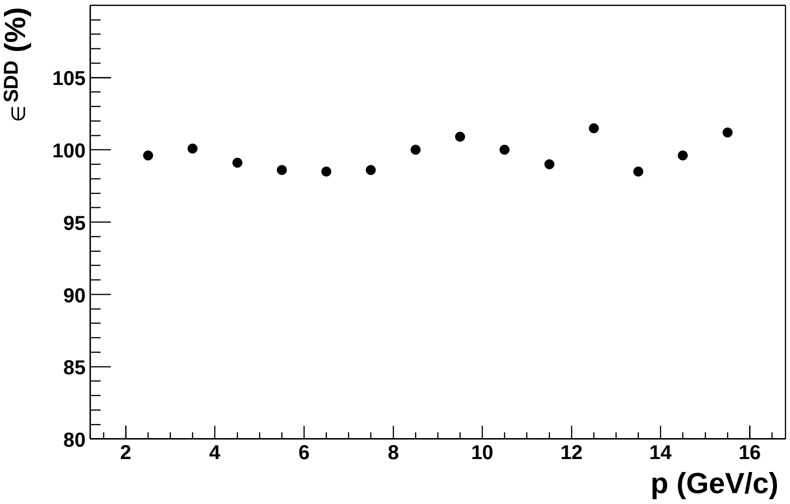

**Figure 4.9:** The efficiency $\epsilon^{SDD}$ *vs* momentum $p$.

We investigated also, how the SDD efficiency looks like differentially. In Fig. 4.8 are shown dependences of $\epsilon^{SDD}$ *vs* polar ($\theta$) and laboratory azimuthal angle ($\phi$). There is a weak increase of the $\epsilon^{SDD}$ with increasing of $\theta$ as a consequence of higher occupancy at small $\theta$, but values are quite close to 100%. The distribution of $\epsilon^{SDD}$ *vs* $\phi$ does not show any dependence. The values are scattered around 100%. In Fig. 4.9 is shown dependence of $\epsilon^{SDD}$ *vs* momentum $p$. As in the case of $\epsilon^{SDD}$ *vs* $\phi$, $\epsilon^{SDD}$ *vs* $p$ distribution does not show any dependence.

## 4.3 Data Used

In this Section, the main features of data used in the elliptic flow analysis, will be shortly presented. In Subsection 4.3.1 will be explained how a partial particle identification is performed. The $dN/d\eta$, $dN/dp_T$ and $dN/d\phi$ distributions of particles used in the elliptic flow analysis are shown in Subsection 4.3.2. The contents of the last subsection of this section concerns the momentum resolution.

### 4.3.1 Particle Identification

In order to perform the elliptic flow analysis it is important to have a sample of particles, as pure as possible, which will be used. This is especially important for the determination of the reaction plane due to the fact that the information about the reaction plane originates from the flow and the flow itself is different for different particle species. In this subsection the sample of particles used in the analysis will be defined.

Charged particles which passed the CERES detectors within its acceptance made tracks. In order to accept the track as a source of information of the corresponding particle, that track has to survive several simple quality criteria listed here below:

1. to have pseudorapidity ($\eta$) between $2.05$ and $2.75$
2. to have transverse momentum $p_T$ bigger than $0.05$ GeV/c
3. the minimal number of hits per track, which depends on $\theta$, has to be between 8 and 12 hits per track. On average it is more than 50% of the maximal number of hits per track (20).
4. radial distance from the track to the vertex position in the $x - y$ plane had to be smaller than $3.0$ cm. In that way non-vertex tracks are suppressed
5. TPC and SDD track segments have to match within $\pm 3\sigma$ window

In that way the 'good' tracks were selected, but still there is no information about the particle specie represented by the track. The CERES experimental setup does not allow full particle identification. Using the TPC, partial particle identification is done with help of 2-dimensional momentum-$dE/dx$ particle distribution. In Fig. 4.10 is shown momentum-$dE/dx$ distribution of all, positive and negative, detected particles. As $\pi^{\pm}$ are chosen positive and negative particles which satisfy the following condition:

$$0.85\frac{dE}{dx}(\pi^{\pm}) \leq \frac{dE}{dx} \leq 1.15\frac{dE}{dx}(\pi^{\pm}) \tag{4.5}$$

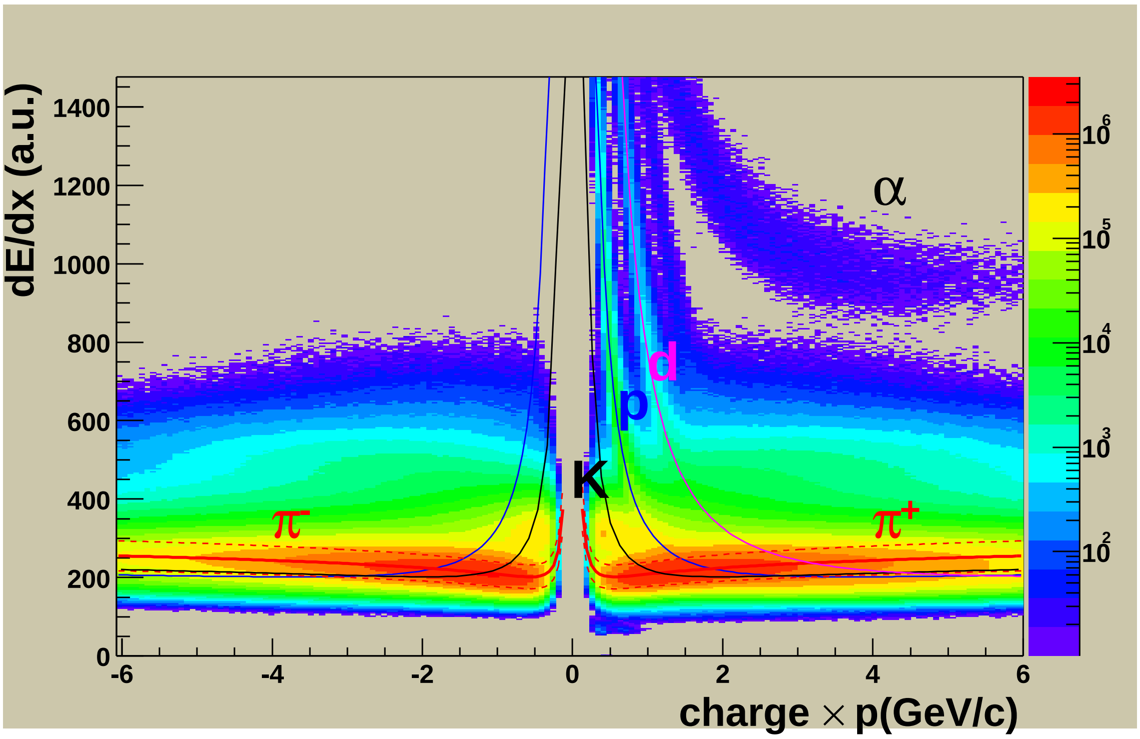

**Figure 4.10:** The momentum-$dE/dx$ particle distribution for all detected charged particles. Full lines represent a nominal energy loss calculated by using the Bethe-Bloch formula. Within dashed line (which corresponds to $\pm 1.5\sigma$ confidence) are chosen $\pi^+$. The same is in the case of $\pi^-$. Even more, $\alpha$ particles as well as low momentum protons and deuterons are clearly separated by their $dE/dx$.

independently of the momentum. This selection corresponds to $\pm 1.5\sigma$ window (dashed lines) around the nominal energy loss for pions $\frac{dE}{dx}(\pi^\pm)$ calculated according to Bethe-Bloch formula (full line). In the region of low momenta, using the $dE/dx$ allows to identify the protons, deuterons and $\alpha$ particles.

### 4.3.2 The $dN/d\eta$, $dN/dp_T$ and $dN/d\phi$ distributions

The pseudorapidity (left) and $p_T$ (right) distribution of particles detected in the TPC are shown in Fig. 4.11. Only those TPC tracks which satisfy quality criteria listed in the previous subsection were used. The covered pseudorapidity region is quite close to the midrapidity region which, at an incident energy of 158 AGeV/c, is 2.92. The TPC covers a huge $p_T$ range from few tens of MeV/c up to more than 4 GeV/c with a mean value of $\langle p_T \rangle \approx 0.5$ GeV/c.

Fig. 4.12 shows the distribution of laboratory azimuthal angle $\phi_{lab}$. As it was already mentioned, the TPC has full azimuthal coverage from $-\pi$ to $\pi$. But the efficiency of detection of particles at any $\phi_{lab}$ is not the same. Due to that one can see very narrow holes at certain $\phi_{lab}$ angles. Their distribution is rather regular. The wholes in $dN/d\phi_{lab}$ distributions originate from the edges of the TPC chambers where the efficiency of detection of particles quickly decreases. Also, at $\phi_{lab} \approx -3$, there is a big whole which appeared due to the fact that 1/3 of a chamber's electronics did not have the low voltage supply.

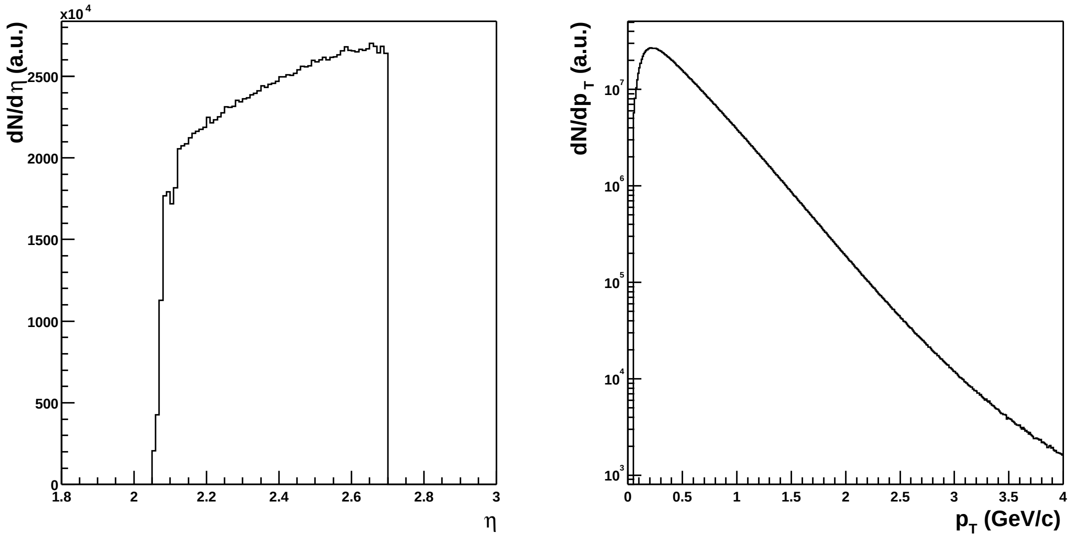

**Figure 4.11:** The pseudorapidity (left) and $p_T$ (right) distribution of particles detected in the TPC. TPC and SDD track segments are matched within a $3\sigma$ window.

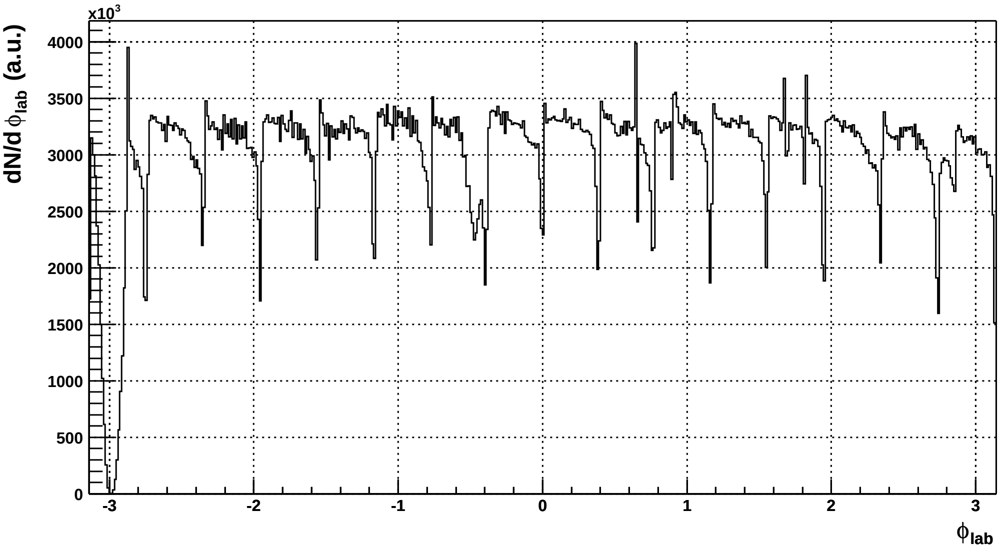

**Figure 4.12:** The distribution of the laboratory azimuthal angle $\phi_{lab}$ in the TPC.

### 4.3.3 The Momentum Resolution

The momentum resolution is determined by the spatial resolution of the detector as well as multiple scattering due to the material from which the detector consists. The relative momentum resolution $dp/p$ as a function of the momentum $p$ can be parameterized in a following way

$$(\frac{dp}{p})^2 = (\frac{dp}{p})^2_{ms} + (\frac{dp}{p})^2_{res} \tag{4.6}$$

with the following assumptions [72, 73]

$$(\frac{dp}{p})_{ms} \propto \frac{1}{\vec{B}}\sqrt{\frac{1}{LX_0}} \tag{4.7}$$

$$(\frac{dp}{p})_{res} \propto p \tag{4.8}$$

$L$ is the measured track length and $X_0$ the radiation length. The *ms* and *res* stands for the multiple scattering and for the spatial resolution of the detector.

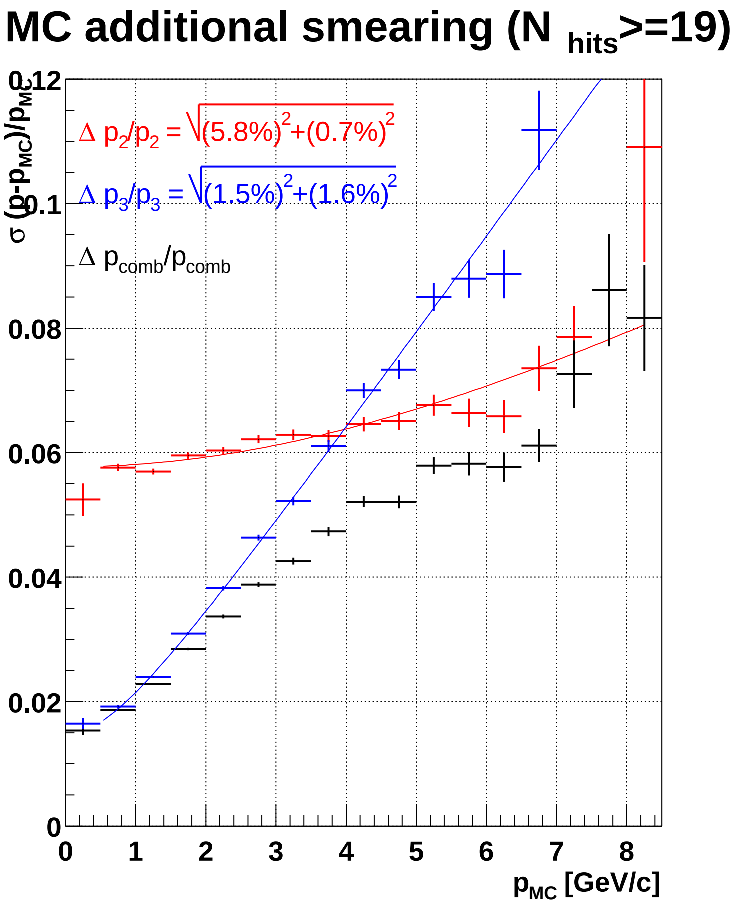

**Figure 4.13:** The momentum resolution obtained by using a Monte Carlo simulation of the detector. The Figure was taken from [5].

It is possible to specify the momentum resolution using a Monte Carlo simulation of the detector. By comparing the reconstructed momentum of a simulated particle with its true momentum, the resolution of the detector can be studied. In Fig. 4.13 is shown the momentum resolution as a function of momentum obtained by using a Monte Carlo simulation of the detector [5]. The two parameter fit depicted as a red histogram provides better results at high momenta, while the three parameter fit depicted as a blue histogram gives better results at small momenta. The combination of these two fits leads to a better momentum resolution over the whole momentum range.

The obtained results suggest that the momentum resolution has a negligible influence on the elliptic flow measurement. For example, at $p = 1$ GeV/c which corresponds to $p_T \approx 0.2$ GeV/c, the momentum resolution is $\Delta p \approx 5$ MeV/c. The smallest bin size used for the elliptic flow analysis in this thesis is 50 MeV/c (see Section 6.3) which is 10 times larger than the momentum resolution.

## 4.4 Centrality Determination

Events detected by CERES in the year 2000 data taking period were not taken with the same trigger conditions. Three triggers were used. A minimum bias trigger contributed with only 0.54% to the total amount of events. Under the trigger condition with $\sigma/\sigma_{geo} \approx 20\%$ have been collected 8.25% of the total amount of events. The biggest part of data (91.21% of events) were taken with a trigger condition with $\sigma/\sigma_{geo} \approx 7\%$. The corresponding TPC multiplicity distributions are shown in Fig. 4.14. Events wiht TPC multiplicity smaller than 70 were cutted-off. The TPC multiplicity distributions are formed from the TPC tracks which satisfy quality criteria listed in the Subsection 4.3.1. All of the distributions are normalized to the minimum bias distribution in the region of the high TPC multiplicity. At the top of the plot is drawn an axis with $\sigma/\sigma_{geo}$ values to make a correspondence to the TPC multiplicities.

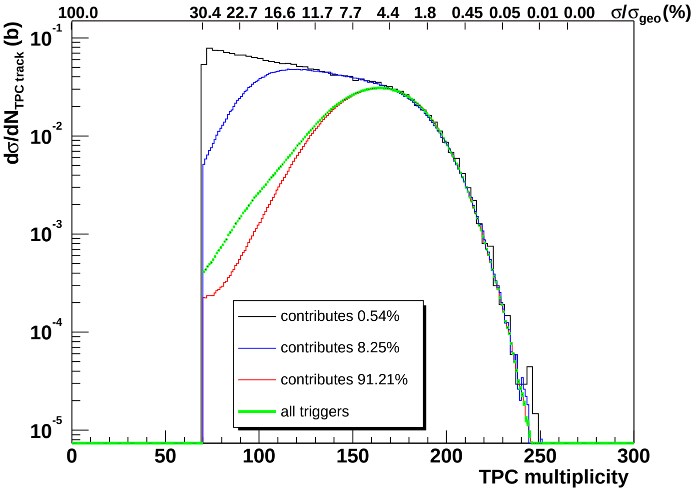

**Figure 4.14:** The TPC multiplicity distribution for all events used in the elliptic flow analysis. The distributions, obtained with different trigger conditions, are normalized to the minimum bias distribution in the high TPC multiplicity region.

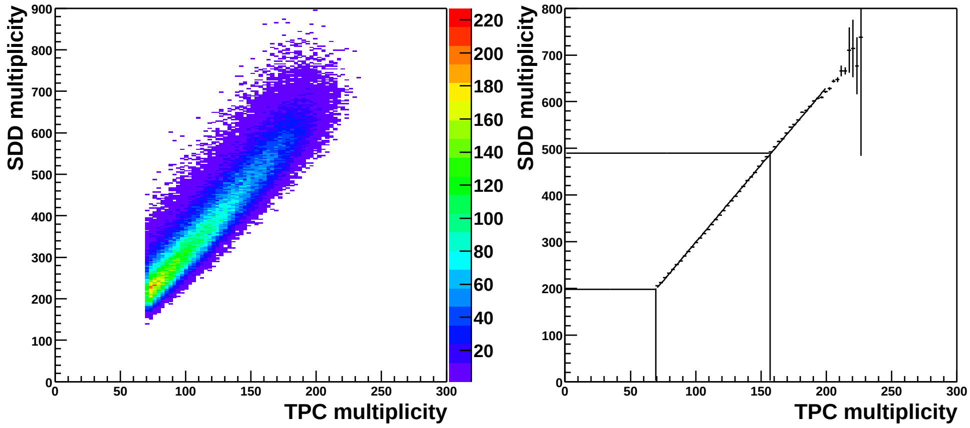

**Figure 4.15:** Left: the correlation between the TPC and SDD multiplicity. Right: The Gaussian mean value of the projection to the SDD multiplicity axis *vs* the TPC multiplicity. A linear fit describes the obtained correlation.

The centrality of the event is determined via the correlation between the TPC and SDD multiplicity. Fig. 4.15 (left) shows the correlation between the TPC multiplicity and the SDD multiplicity. The TPC multiplicity distribution is identical to the one shown in Fig. 4.14. Projecting the distribution at the given TPC multiplicity to the SDD multiplicity axis and fitting it with a Gaussian around the maximum of the projection one gets the one-to-one correspondence between the TPC multiplicity and the SDD multiplicity. This correspondence is shown in Fig. 4.15 (right) together with a linear fit to the obtained result. The fit describes the data very well and the values of the fit are used in the next step of the centrality determination.

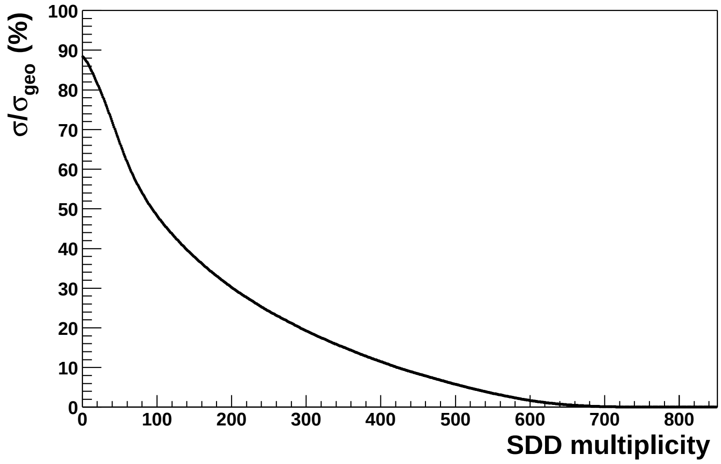

**Figure 4.16:** The correspondence between the SDD multiplicity and the geometrical cross section $\sigma/\sigma_{geo}$.

Fig. 4.16 shows the correspondence between the SDD multiplicity and the geometrical cross section $\sigma/\sigma_{geo}$ [74]. For an event with a given TPC multiplicity one can, using the correspondence shown in Fig. 4.16 find out what the corresponding geometrical cross section is.

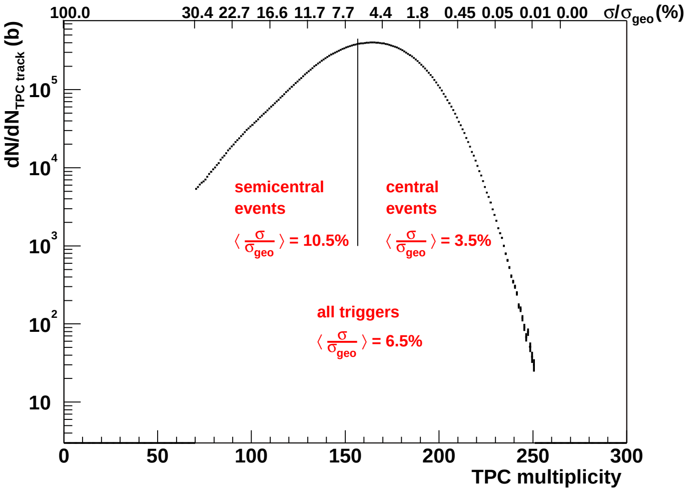

**Figure 4.17:** The TPC multiplicity distribution is divided into two centrality bins in which the elliptic flow analysis is performed. They are characterized with the weighted mean centrality $\langle \sigma/\sigma_{geo} \rangle$.

The $\sigma/\sigma_{geo}$ values shown as the upper axis in Fig. 4.14 are determined in the way described above.

Fig. 4.17 shows two centrality bins in which the differential elliptic flow analysis of $\Lambda$ and $K_S^0$ particles is performed. These two centrality bins are characterized with the weighted mean centrality $\langle\sigma/\sigma_{geo}\rangle$ calculated as an averaged centrality weighted with $d\sigma/dN_{TPCtracks}$. The corresponding values of $\langle\sigma/\sigma_{geo}\rangle$ for two centrality bins mentioned above as well as for all events taken together are shown in the picture.

# Chapter 5

# FLOW ANALYSIS OF SIMULATED DATA

## 5.1 Flowmaker

In order to check the feasibility of different methods for the flow analysis presented in Chapter 3 in application to the CERES data, several sets of the simulated data have been produced using Fortran 77 computer code [75] and a parallel STAR software library STAF package, called MEVSIM [76]. For the sake of brevity it will be called simply *Flowmaker*. The Flowmaker simulator is a new event generator which provides a fast way of producing a large number of uncorrelated A+A collision events. The user can select the number of events, the detector acceptance ranges, the particle types, the multiplicities and the proper one-body momentum space distributions with respect to the transverse momentum ($p_T$), the rapidity ($y$) and the azimuthal angle ($\phi$) distributions from a menu of the model. In addition one can include the reaction plane angle and to specify different harmonics of the anisotropic flow. The particle multiplicities were allowed to vary from event-to-event according to the Poisson statistics. Also, the parameters of the one-body momentum space distributions were randomly varying from event-to-event according to a Gaussian distribution in order to simulate dynamical fluctuations. Finally, the produced events are assumed to be in the A+A center-of-momentum frame. Due to that, in order to use the produced events, the kinematic variables are transformed into the laboratory system which corresponds to the CERES experiment at the top of the SPS energy.

## 5.2 The Data Simulated by the Flowmaker

For the purpose of this thesis only 3 particles species were generated: positive and negative pions ($\pi^{\pm}$) and protons. The $\pi^{+}$ and $\pi^{-}$ contributes each with 45% to the total multiplicity, while the protons ($p$) contributes with 10% to the total multiplicity. Other particle species which have a quite small contribution in the real events like electrons, kaons, $\Lambda$s etc. are neglected in the simulated data. As the feasibility of the method of cumulants and the Lee-Yang Zeroes method strongly depends on the multiplicity and the flow magnitude itself, for the purposes of this thesis were simulated several different sets of data. For the first and largest one, 20 M of the very central events which correspond to the experimental data were simulated. The shape and the mean value of the multiplicity distribution are

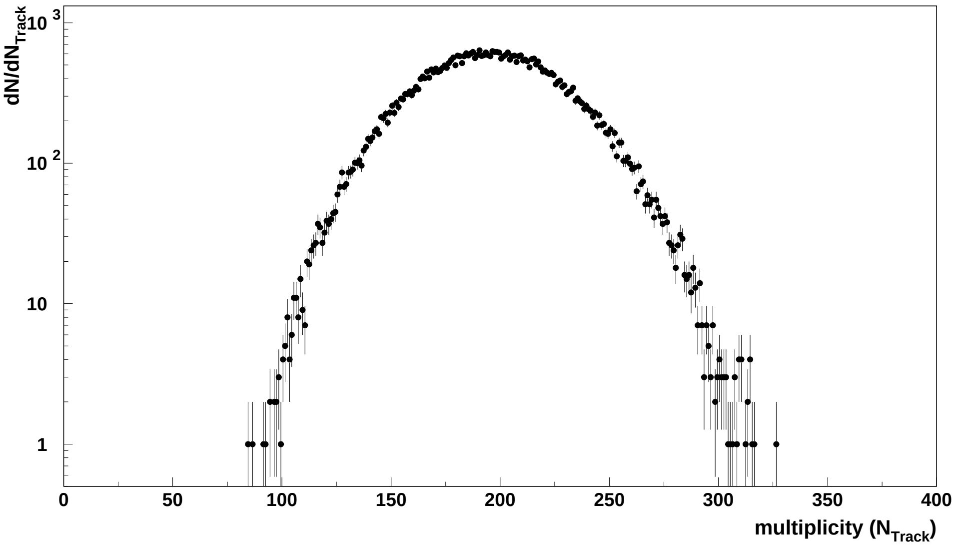

**Figure 5.1:** Multiplicity distribution from the Flowmaker simulated data.

similar to the experimental values and they are shown in Fig. 5.1. Although in the experimental multiplicity distribution (see Fig. 4.17) exists a part of semicentral events they were not simulated using the Flowmaker. The simple Gaussian like multiplicity distribution was simulated by the Flowmaker due to the fact that the majority of the experimental events (above 90%) belong to the class of central events.

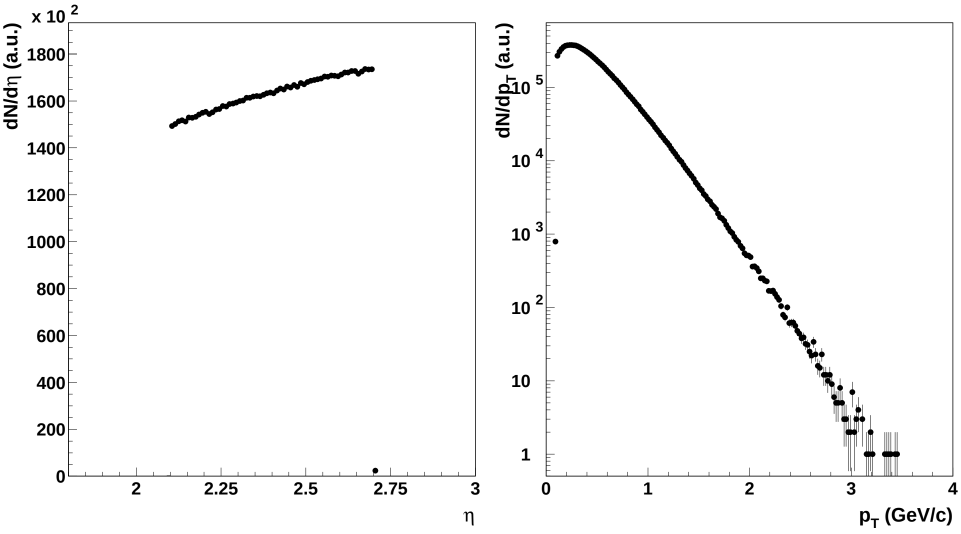

**Figure 5.2:** $dN/d\eta$ (left) and $dN/dp_T$ (right) distribution from the Flowmaker simulated data.

The input values for the Flowmaker are chosen in such a way that $dN/d\eta$ and $dN/dp_T$

have a similar shape as in the case of the experimental data (see Fig. 4.11). The corresponding distributions are shown in Fig. 5.2.

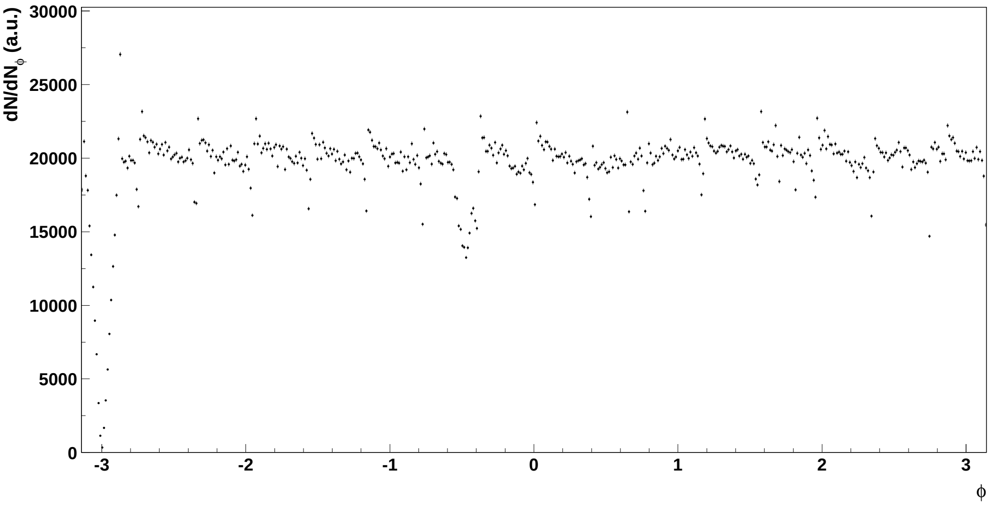

**Figure 5.3:** $dN/d\phi$ distribution from the Flowmaker simulated data.

As the inefficiency in the $dN/d\phi$ distribution strongly influences on the position of the reconstructed reaction plane, the $dN/d\phi$ distribution in the Flowmaker simulated data had to follow the corresponding distribution in the experimental events. The Fig. 5.3 shows the $dN/d\phi$ distribution obtained from the Flowmaker generator. It was generated using the proper weights from the experimental distribution (see Fig. 4.12).

The input values for the integrated anisotropic transverse flow were $v_1 = 0.5\%$ and $v_2 = 2.0\%$. They are quite small just like that what is expected in the case of the experimental data. In the case of the directed flow, the value of the $v_1$ is not independent on $\eta$ and $p_T$. The pseudorapidity dependence of $v_1$ is simulated in a way to show a pion directed flow for the central collisions at the top SPS energy [55]. A similar statement is also valid for the simulated $p_T$ dependence of $v_1$. As the CERES detectors cover a rather small (pseudo)rapidity interval, the $v_2$ dependence was simulated in a way that it does not depends on $\eta$, but it has a typical $p_T$ dependence not corrected for the HBT effect. It grows quickly with $p_T$ for small $p_T$ and then much slower in the region of high transverse momenta.

In each simulated event, the position of the reaction plane is known. Using that information one can easily calculate the 'true' flow. In that way one is just reproducing the input values.

## 5.3 Flow Analysis of the Simulated Data Using the Reaction Plane Method

Although in a real event exists only one reaction plane, it's position is not known and one has to reconstruct it from the emitted particles. In order to check the codes which have been developed for the anisotropic flow analysis applied to the experimental data, these codes were applied on the simulated events in exactly the same way as in the case of the real data. The procedure consists out of several steps. In the fist one, the $X_n$, $Y_n$ $(n = 1, ..., 4)$ values were calculated in each event according to the Eq. (3.4). Using them one can obtain a ”rough” position, determined with the azimuthal angle $\Phi_n$, of the reaction plane using Eq. (3.4). The calculation has been done for each of 4 slices [1]separately. Also, at the end of the first step, files with mean values $\langle X_n \rangle$, $\langle Y_n \rangle$ $(n = 1, ..., 4)$ obtained by averaging over events for each 4 slices have been created.

The main characteristic of the obtained $dN/d\Phi_n$ distributions is that they are not flat as it should be. In the second step of the analysis the method of shifting is performed in order to make these distributions flat. In each event one calculates $X_n$ and $Y_n$ and then from the obtained sums one needs to subtract $\langle X_n \rangle$ and $\langle Y_n \rangle$ values found from the first step of the analysis. Obtained ”shifted” $dN/d\Phi_n$ distributions are flatter, but not enough. Together with determining the ”shifted” distributions, in the second step was also calculated Fourier coefficients for flattening based on Eq. (3.9).

In the third step the final flattening was performed. Again, the values of $(X_n, Y_n)$ were calculated, and then the values of $(\langle X_n \rangle, \langle Y_n \rangle)$ were subtracted. In order to correct $\Phi_n$, in each event values of $\Delta\Phi_n$ were calculated using Fourier coefficients obtained from the second step and Eq. (3.9). The final $dN/d\Phi_n$ distributions became completely flat [2]. This is the best possible estimation of the reaction plane. But due to the finite multiplicity it does not coincide with the true reaction plane. So, the reaction plane resolution is not infinitely small and consequently the flow correction factors are bigger than 1.

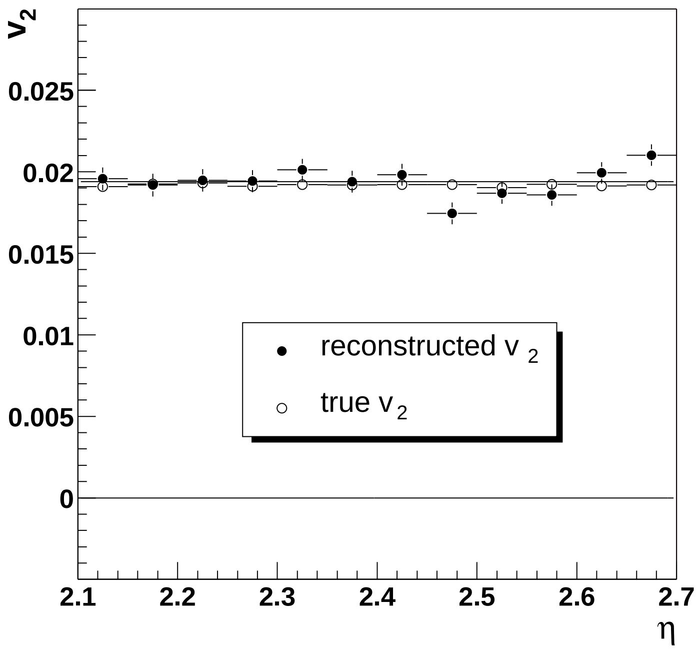

**Figure 5.4:** The true (open circles) and reconstructed (closed circles) second Fourier coefficient *vs* $\eta$.

---

[1] System of slices will be explained in the next Chapter

[2] Figures which show the shape of rough, shifted and flat $dN/d\Phi_n$ distributions are essentially the same as those shown in Section 6.2)

In the final, $4^{th}$, step the "observed" Fourier coefficients $v'_n$ $n = 1, ..., 4$ are calculated with respect to the reconstructed reaction plane. These Fourier coefficients were *a posteriori* corrected for the reaction plane resolution according to:

$$v_n = v'_n / \langle \cos[n(\Delta\Phi_n)] \rangle \quad (5.1)$$

As in this thesis the elliptic flow was investigated, here it is interesting to show the reconstructed $v_2$ dependences on the pseudorapidity ($\eta$) and the transverse momentum $p_T$. In Fig. 5.4 are shown the reconstructed Fourier coefficients $v_2$ *vs* pseudorapidity as closed circles. In order to compare that with the input values, with open circles are shown the $v_2$ Fourier coefficients *vs* pseudorapidity calculated with respect to the true reaction plane (which is known in the Flowmaker simulator). Input values and functional dependences of $v_2$ *vs* pseudorapidity are fully reconstructed. The $v_2$ value does not depend on $\eta$ as one should expect for a narrow $\eta$ coverage in the case of the CERES experiment. It is constant and roughly equal $2\%$. The relative deviation from the true $v_2$ value is smaller than 10%.

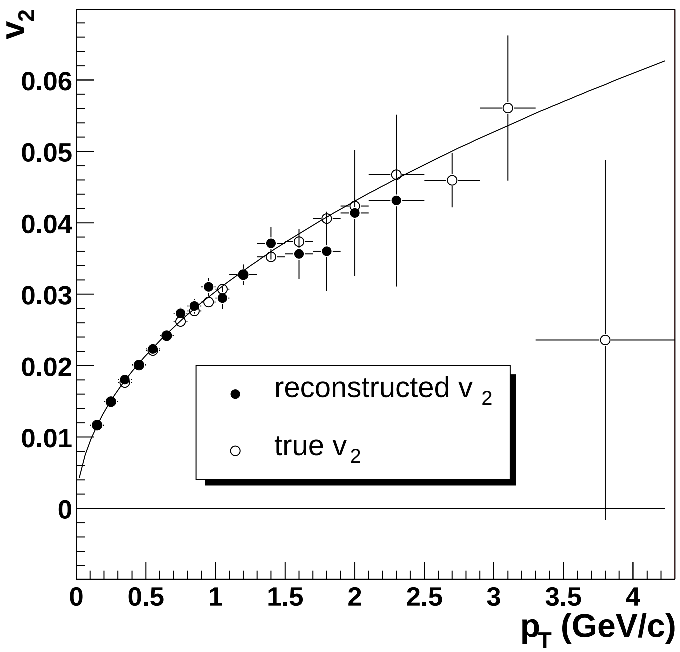

**Figure 5.5:** The true (open circles) and reconstructed (closed circles) second Fourier coefficient *vs* $p_T$ .

The $p_T$ dependence of the elliptic flow is also fully reconstructed. The reconstructed $v_2$ *vs* $p_T$ values are shown in Fig. 5.5 as closed circles while the true $v_2$ *vs* $p_T$ values are shown as open circles.

A perfect agreement between the true and reconstructed $v_2$ values insures that the procedure which is applied on the experimental data is correct.

## 5.4 Cumulant Analysis of the Simulated Data

Here, the results of the cumulant analysis applied on the simulated data are presented. The analysis is performed in order to reconstruct only the integrated elliptic flow, and it follows the procedure described in Subsection 3.5.1.

As, according to Eq. (3.41), the feasibility of the cumulant method strongly depends on the multiplicity $M$, available statistics $N$, and the flow magnitude itself, the new set of events created with the Flowmaker simulator was made. The elliptic flow magnitude is 3% and the directed one is 0.5%. The mean multiplicity was increased up to 300. Fig. 5.6 shows the obtained results. On the left plot are shown obtained $v_1$ values and on the right one the $v_2$ values.

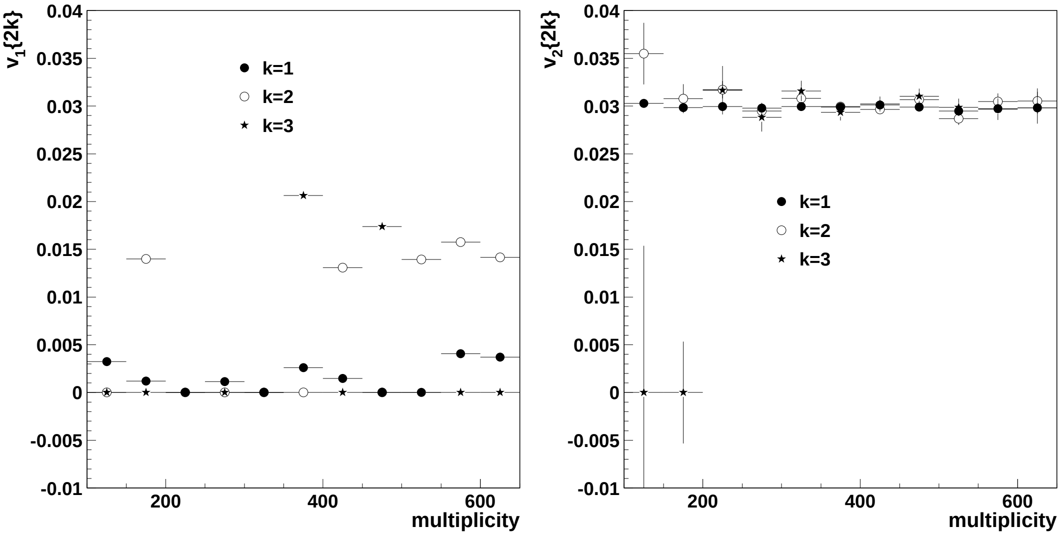

**Figure 5.6:** The integrated $v_1$ (left) and $v_2$ (right) dependence on multiplicity obtained from the first three cumulants.

From all three first cumulants $c_2\{2k\}$, $k = 1, 2, 3$, the elliptic flow value of 3% was reconstructed. The exception is the $v_2\{6\}$ at the smallest multilpicities. As in the simulated data the only correlations are those which originate from the flow, it is naturally that flow reconstructed from different cumulants is the same. The difference is in the statistical errors which grow with increasing of the order of cumulant.

The directed flow is not reconstructed at all due to the quite small value. The non-zero $v_1$ values appear as a spurious flow. Here one should emphasize that if the anisotropic flow is small one needs, according to Eq. (3.41), a huge statistics and multiplicity in order to be able to reconstruct the flow magnitude. For the CERES data analysed in this thesis the $v_2$ is smaller than 0.012 at $\sigma/\sigma_{geo} < 5\%$ where the population of events is highest (see Fig. 4.14). If one wants to have a relative statistical error not bigger than $1/3$, according to Eq. (3.41) one needs at least $9 \cdot 10^9$ events. Considering the fact that the generating function can be averaged only over events with the same multiplicity, the above found requirement is not fulfilled.

## 5.5 Lee-Yang Zeroes Analysis of the Simulated Data

Again, as in the case of the cumulant analysis, the Lee-Yang zeroes analysis has been performed only for the elliptic flow reconstruction. This is due to the fact that only flow with magnitude greater than $j_{01}/\sqrt{2MlnN}$ could be safely measured. From this formula one can see that a huge statistics has a most important role in the reconstruction of the anisotropic flow magnitude if the flow itself is small. Due to that, a new set of events created with the Flowmaker was simulated with higher elliptic flow magnitude ($v_2 = 0.056$) and without the directed flow.

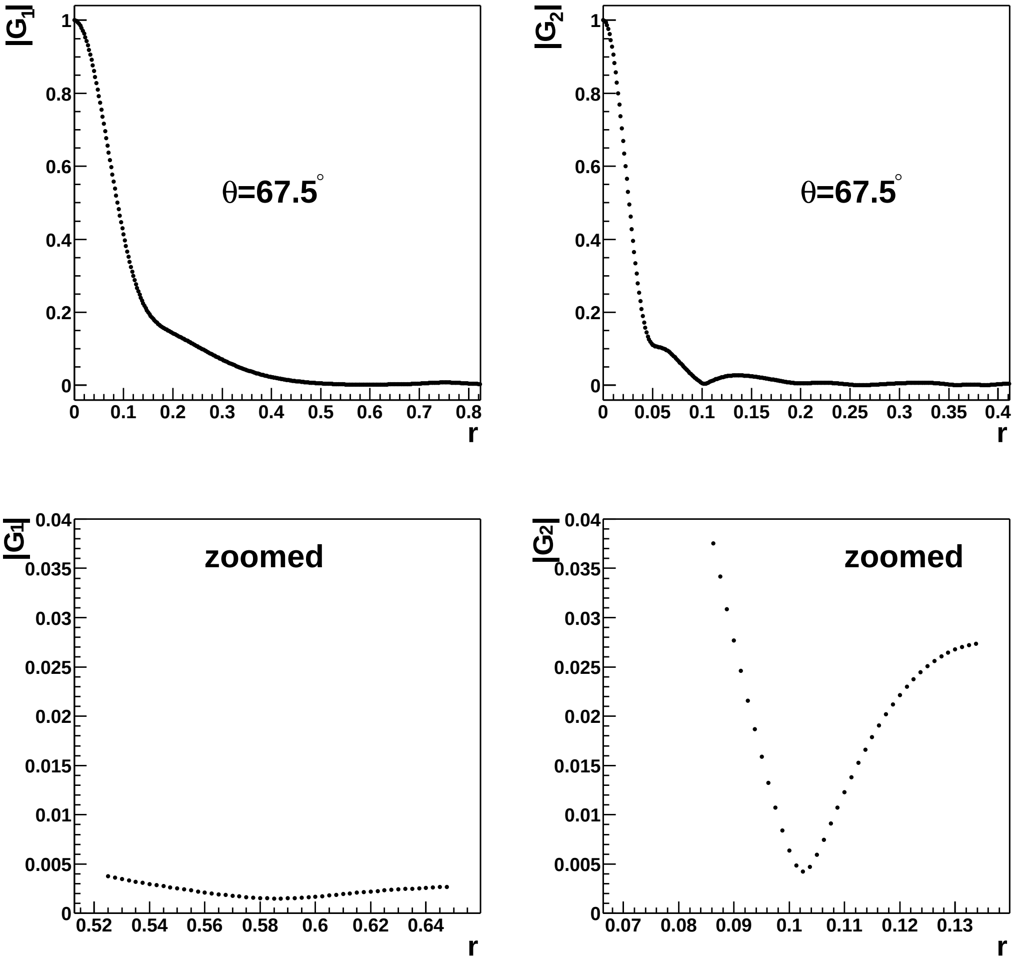

**Figure 5.7:** Top: the absolute values of the generating functions $G_n$ in the case of the directed (left) and elliptic (right) flow plotted against the $r$ value. Bottom: the same as at the top but zoomed at the position of the minimum.

In order to reconstruct anisotropic flow using the method of Lee-Yang zeroes the procedure described in Sec. 3.6 was followed. First, we calculated and tabulated the complex valued function $g^{\theta}(ir)$ for $4$ equally spaced values of $\theta$ and for appropriately chosen discrete values of $r$. As $g^{\theta}(ir)$ has to be a smooth function of $r$ we calculated its values at enough high number of discrete points in $r$ direction in order that the obtained distribution looks like a function. This is necessary for a precise determination of the $r_0^\theta$ position of the minimum of $g^\theta(ir)$. Using Eq. (3.69) the integrated flow $V_n$ has been calculated[3].

At the top of the Fig. 5.7 are shown the absolute values of the generating functions for the directed (left) and the elliptic (right) flow. As an example values of $|G_n(r)|$ at $\theta = 67.5°$ are shown. In the case of the directed flow the absolute value of the generating function does not have a real minimum necessary for the flow determination. Fluctuations can produce a very shallow and broad minimum of $|G_n(r)|$ which position differs from one to another value of $\theta$. The corresponding value of the 'spurious flow' satisfies non-equality (3.75). On the right top plot is visible a clear minimum in the $|G_n(r)|$ produced by the existence of the significant elliptic flow. At the bottom part of the Fig. 5.7 are shown the absolute values of the generating functions for the directed (left) and the elliptic (right) flow zoomed around the position of found minima.

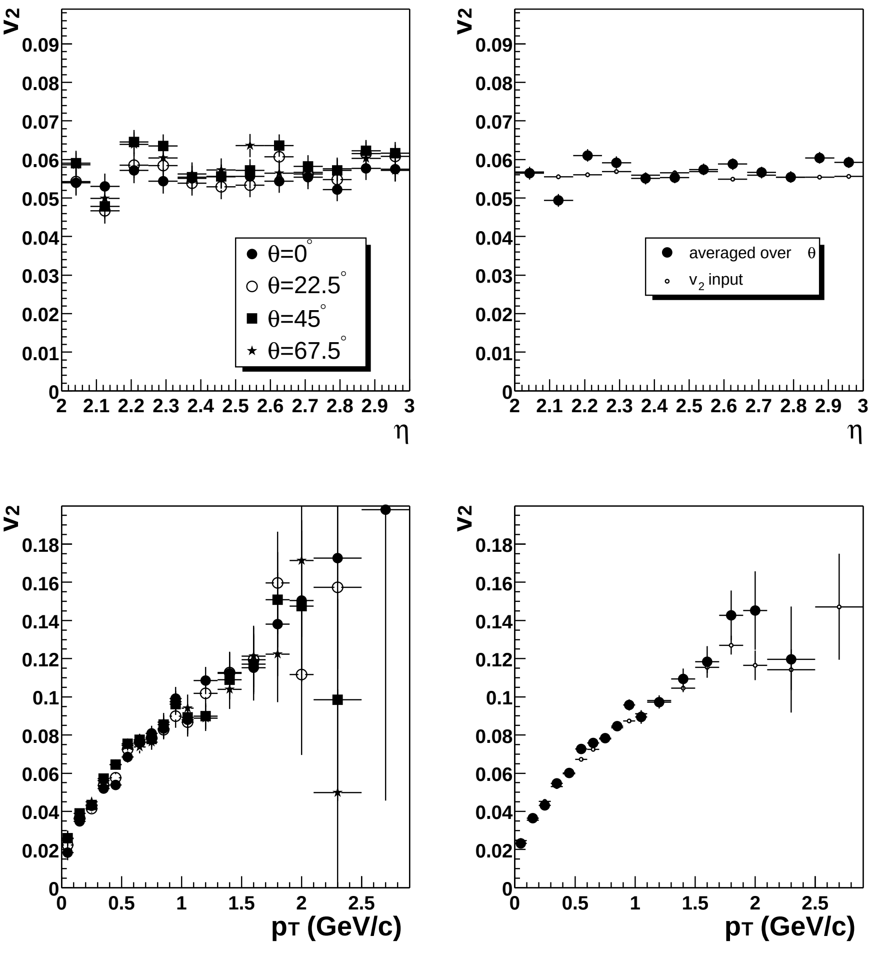

**Figure 5.8:** The reconstructed value of $v_2$ *vs* $\eta$ (top) and *vs* $p_T$ (bottom) for different $\theta$ values (left) and averaged over different $\theta$ values (right).

---

[3] In the method of Lee-Yang zeroes, the integrated flow $V_n$ is defined as a product of the flow $v_n$ integrated over $y$ and $p_T$ and then multiplied to the mean number of particles averaged over many events used in the analysis

In the next step, obtained values for the integrated elliptic flow $V_2$ has been used for the reconstruction of the differential flow via Eq. (3.73). In Fig. 5.8 are shown the obtained results. The reconstructed values of the $v_2$ *vs* pseudorapidity are shown at the top part of the Fig. 5.8, while the $v_2$ *vs* transverse momentum are shown at the bottom bottom part of the Figure. On the left side of the Fig. 5.8 are shown results obtained at different $\theta$ values, while on the right part are shown the corresponding results averaged over different $\theta$ values. One can see that reconstructed flow is in a perfect agreement with input flow values. At the end of this Chapter one has to stress that in the case of a limited statistics (even if it is measured in million of events) if the magnitude of the anisotropic flow is small enough, the cumulant method and the method of Lee-Yang zeros are unapplicable. Only the spurious flow can be produced by these methods. Contrary, if the magnitude of the anisotropic flow is big enough, then it can be safely reconstructed. Because of such a limitation and due to the fact that in this thesis is analised the elliptic flow in rather central collisions ($v_2 \approx 0.015$) the method of Lee-Yang zeros were not used in this thesis [4].

---

[4] According to the non-equality (3.75), with the available statistics, only an elliptic flow with the magnitude bigger than $3.2\%$ can be measured

# Chapter 6

# FLOW ANALYSIS OF CHARGED PARTICLES

In this Chapter will be presented the results of the anisotropic transverse flow measurements of charged particles using the Standard Flow Analysis which is described in Section 3.4. Some specific features of the charged particle elliptic flow analysis performed using the CERES data will be presented in detail.

## 6.1 Particle Selection

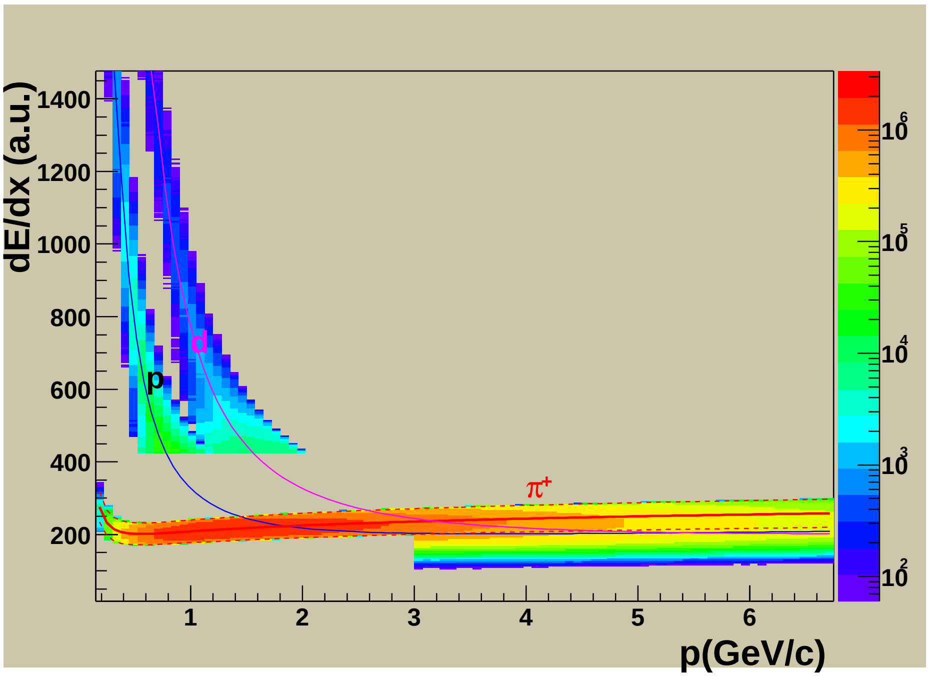

**Figure 6.1:** The momentum-$dE/dx$ particle distribution for the selected pions, protons and deuterons. Full lines represent a nominal energy loss calculated by the Bethe-Bloch formula. Within dashed lines (which correspond to $\pm 1.5\sigma$ confidence) are chosen $\pi^+$. The same is in the case of $\pi^-$. The low momentum protons and deuterons are clearly separated by their $dE/dx$.

Charged particles mostly consist of $\pi^{\pm}$ and a small admixture of protons and kaons which survived the dE/dx selection (see Subsection 4.3.1). In Fig. 6.1 is shown the momentum-$dE/dx$ distribution where the positive pions are selected using a band which corresponds to $\pm 1.5\sigma$ confidence level (denoted with the dashed lines) around the nominal energy loss for the positive pions calculated by using the Bethe-Bloch formula (denoted with the full lines). In Fig. 6.1 one can see that in the region between 1 and 3 GeV/c and the $dE/dx$ values around 220 a part of protons cannot be removed from the pion sample. In Section 6.4 the elliptic flow of the identified low momentum protons is presented. These protons are clearly visible Fig. 6.1.

## 6.2 Determination of the Reaction Plane

The first step in the Standard Flow Analysis which uses the reaction plane method is to calculate the position of the reaction plane. The position of the reaction plane is calculated (see Section 3.2.1) using $\pi^{\pm}$ selected as described in the previous section. In order to avoid the autocorrelation effect and partially the HBT effect the $2\pi$ azimuthal coverage was divided into 4 groups of slices. In total there are $100$ slices distributed regularly in $4$ groups which are denoted with $1$, $2$, $3$ and $4$. So each group consists out of $25$ slices, and each slice covers $3.6^{\circ}$ in $\phi$. The autocorrelation effect is removed by correlating a particle from one slice with the reaction plane determined from the non-adjacent slice (see Fig. 6.2). For example, if a particle of interest belongs to the slice number $3$ then one has to correlate it with a reaction plane determined from the slice number $1$. Concerning partial removing of the HBT effect see Section 6.5.

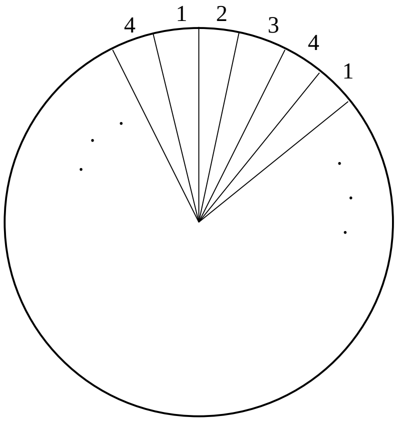

**Figure 6.2:** The distribution of slices in $\phi$ space. The size of a slice is $3.6^{\circ}$. Each fourth of them forms a group denoted with 1, 2, 3 or 4.

So, although in an event exists only one real reaction plan, one has to reconstruct its position in each slice separately. Additionally, in order to calculate the magnitude of the anisotropic transverse flow which corresponds to different Fourier harmonics one reconstructs the position of the reaction plane separately for each harmonic. Together with the reconstruction of the position of the reaction plane one has to calculate the reaction plane resolution in order to correct the observed flow magnitude for the finite reaction plane resolution. As it depends on multiplicity the position of the reaction plane was reconstructed for different centralities also. So, instead of one reaction plane per event one calculates $4$ (slices)$\times$ $4$ (harmonics)$\times$ $6$ (centralities) = $96$ different reaction planes.

Of course, they are actually correlated. That feature is used in order to calculate the corresponding reaction plane resolution. In order to perform such a calculation, each event/slice was randomly divided into two subevents/subslices and corresponding reaction planes were calculated.

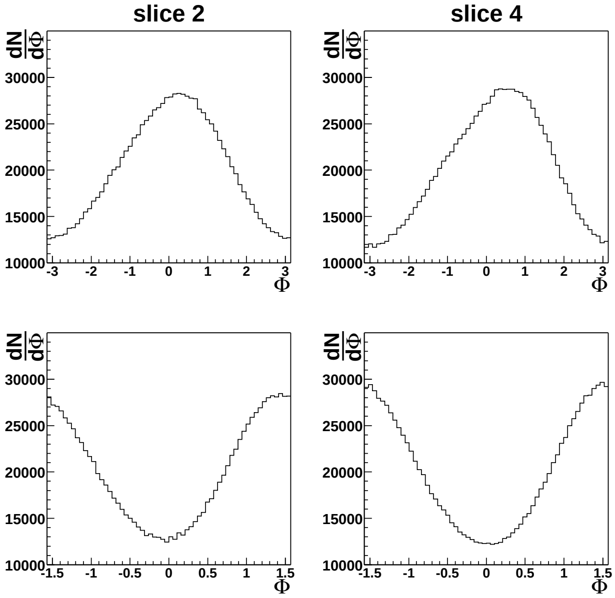

**Figure 6.3:** Raw reaction plane distribution calculated from $X_n$ and $Y_n$ coefficients for $n = 1$ (top) and $n = 2$ (bottom) in the second (left) and fourth (right) slice.

In Fig. 6.3, as an example, are shown the reaction plane distributions $dN/d\Phi$ for the first two harmonics $n = 1, 2$ (top and bottom) in slice $2$ and $4$ (left and right). Due to the non-flat distributions of particles in the laboratory azimuthal angle $\phi$, these distributions are not flat as it should be. One should notice that there is a little difference between the shapes of $dN/d\Phi$ distributions derived from two slices due to similar topology of the slices. From the other side, there is a clear difference in the shape of $dN/d\Phi$ distributions

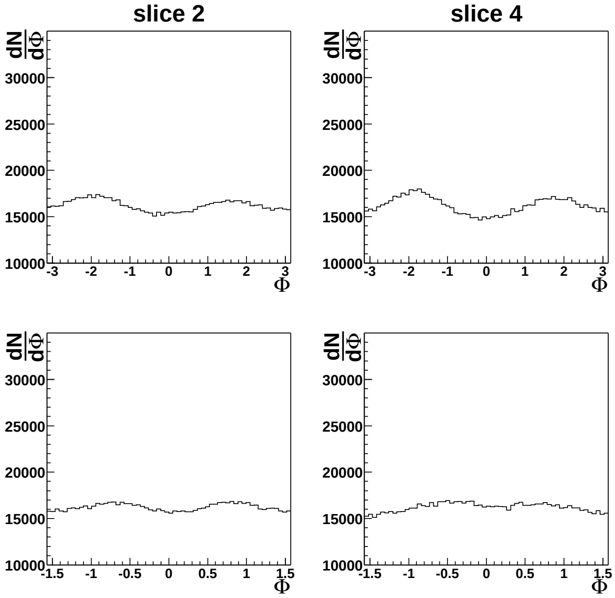

**Figure 6.4:** The reaction plane distribution after applying the shifting method for $n = 1$ (top) and $n = 2$ (bottom) in the second (left) and fourth (right) slice.

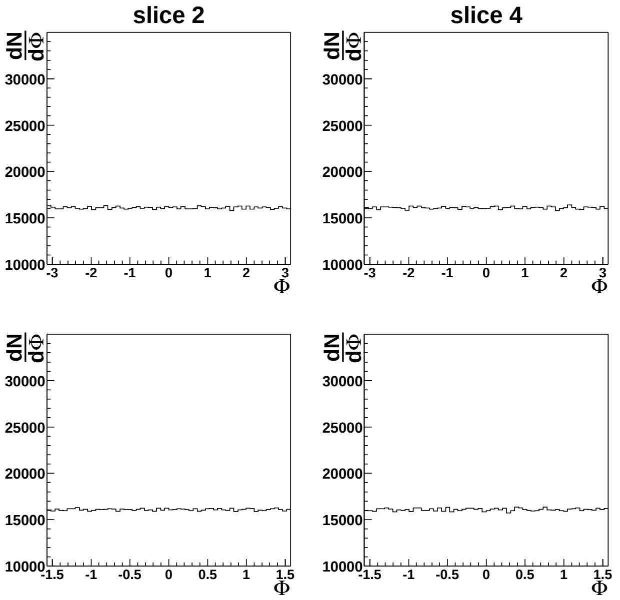

**Figure 6.5:** The reaction plane distribution after applying the shifting and the Fourier method of flattening for $n = 1$ (top) and $n = 2$ (bottom) in the second (left) and fourth (right) slice.

for different harmonics. So, one has to make them flat. In order to fulfill it, it is enough to apply successively first the method of shifting, and then the Fourier method of flattening

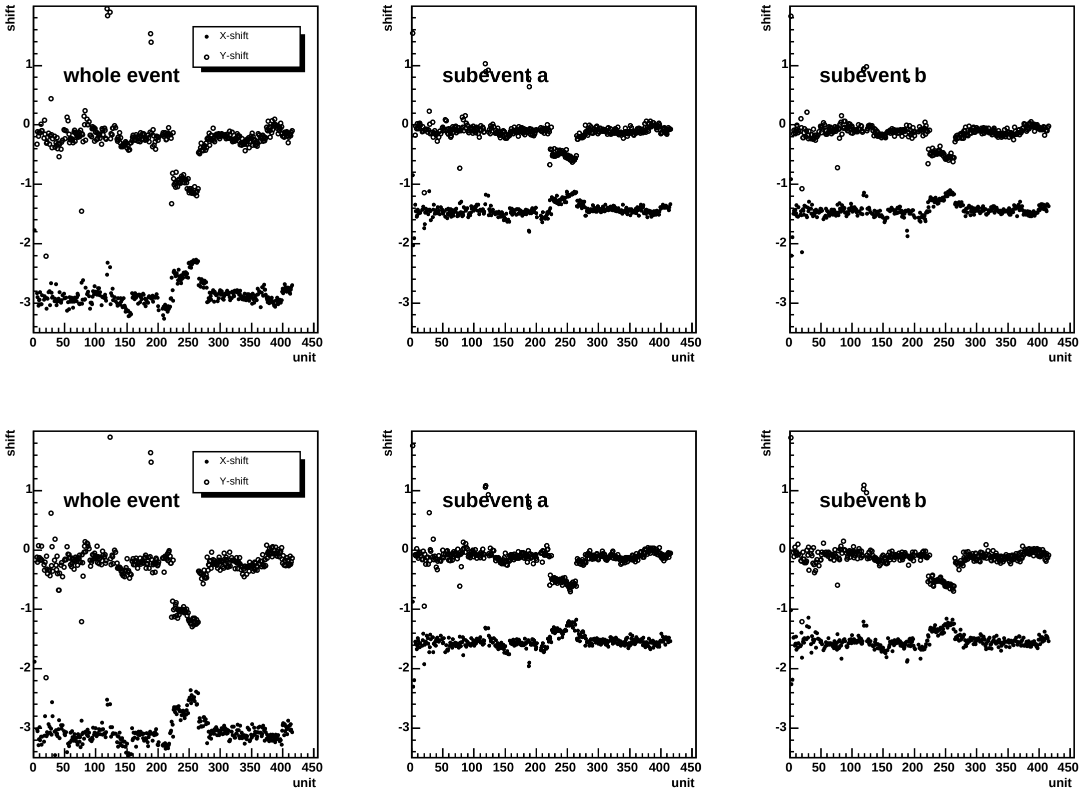

**Figure 6.6:** Shifting coefficients $X_n$ and $Y_n$ for $n = 2$ in the first two centrality bins (up and down) for the whole event (left), and subevents $a$ (center) and $b$ (right) versus the unit number.

(for the description see Section 3.2.2). The results of these methods are shown in Fig. 6.4 and Fig. 6.5 for the same harmonics/slices as in Fig. 6.3. After shifting, which makes rough flattening, the reaction plane distribution $dN/d\Phi$ became more flat (Fig. 6.4) but not completely. In order to make it completely flat, the Fourier method of flattening was applied (Fig. 6.5). Due to consistency, the procedure of the reaction plane determination was done for all slices, harmonics and for all centrality bins.

In order to check the stability of the shifting and the Fourier flattening coefficients for different units, in Fig. 6.6 are shown the shifting coefficients $X_n$ and $Y_n$ (for $n = 2$) and for $2$ different centralities for the whole event (left) subevent $a$ (middle) and subevent $b$ (right). One can see that these distributions do not depend on the unit number except in the region between unit $225$ and $265$ which corresponds to the negative $B$-field data. Also, the shifting coefficients for the whole event are twice larger than in the case of the subevents. This is a consequence of the fact that the whole event has twice larger multiplicity than the multiplicity of one subevent.

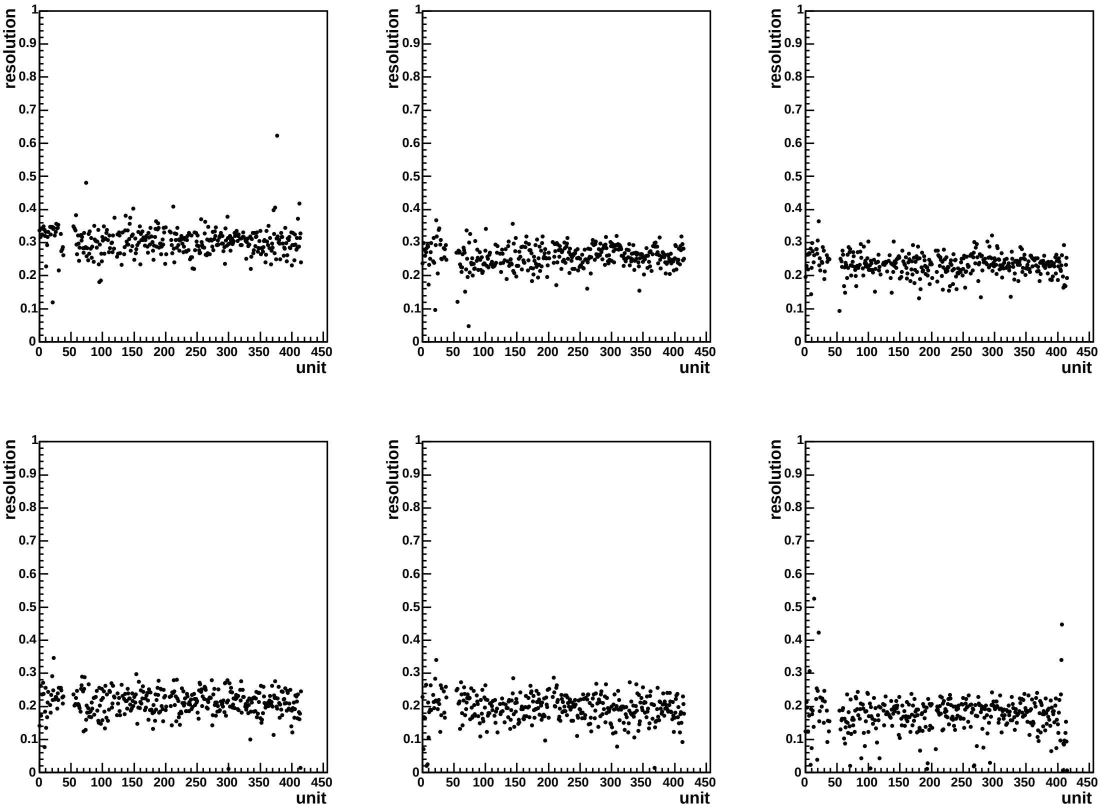

**Figure 6.7:** Reaction plane resolution in case of the second harmonic for all centrality bins *vs* unit number.

From Fig. 6.7 one can notice that the reaction plane resolution becomes smaller with increasing of the centrality as it is expected because flow has to decrease with centrality. Also, the width of the distribution of the reaction plane resolution with respect to the unit number becomes bigger with increasing of the centrality for the same reason.

Before the continuation of the charged elliptic flow analysis, the other way of the reaction plane determination and the charged elliptic flow analysis used in this thesis will be shortly presented. As the charge of particles is well defined in the CERES experiment, one can instead of dividing the event into four subevents (the ’slice’ method) to divide the event into two subevents. Positive pions, defined in Subsection 4.3.1, form the first subevent and negative pions form the second one. Again the autocorrelation effect is removed by correlating the pion from one subevent to the reaction plane constructed from the other one. The advantage of this approach with respect to the ’slice’ method is that the reaction plane resolution is better due to the bigger multiplicity used for the reaction plane reconstruction. In Fig. 6.8 are presented the values of the correction factors in different centrality bins for both, above mentioned, methods. In both cases, the correction factors grow with the TPC multiplicity because the elliptic flow and hence the resolution, decrease with the multiplicity. Due to roughly two times higher multiplicity in the 2 subevents method with respect to the ’slice’ method, the correction factors are $\approx \sqrt{2}$ times smaller then in case of the ’slice’ method.

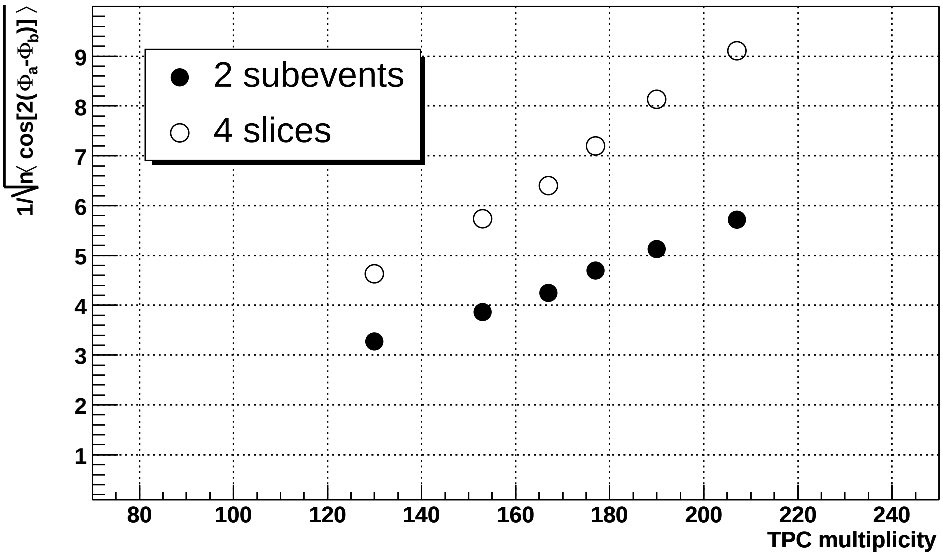

**Figure 6.8:** The correction factors *vs* centrality expressed via TPC multiplicity for the 2 subevents and the ’slice’ method. Due to the roughly double multiplicity, correction factors in the 2 subevents method are $\approx \sqrt{2}$ times smaller then in case of the ’slice’ method.

## 6.3 Elliptic Flow of Pions

In this section the results on $\pi^{\pm}$ elliptic *vs* pseudorapidity, rapidity, transverse momentum and centrality obtained from the two methods will be shown. Also, a comparison between the results obtained from the 2 subevents method and the results obtained using the ’slice’ method will be presented. All results which are going to be presented in this Section are not corrected for the Hanbury-Brown and Twiss (HBT) effect. Differences between the

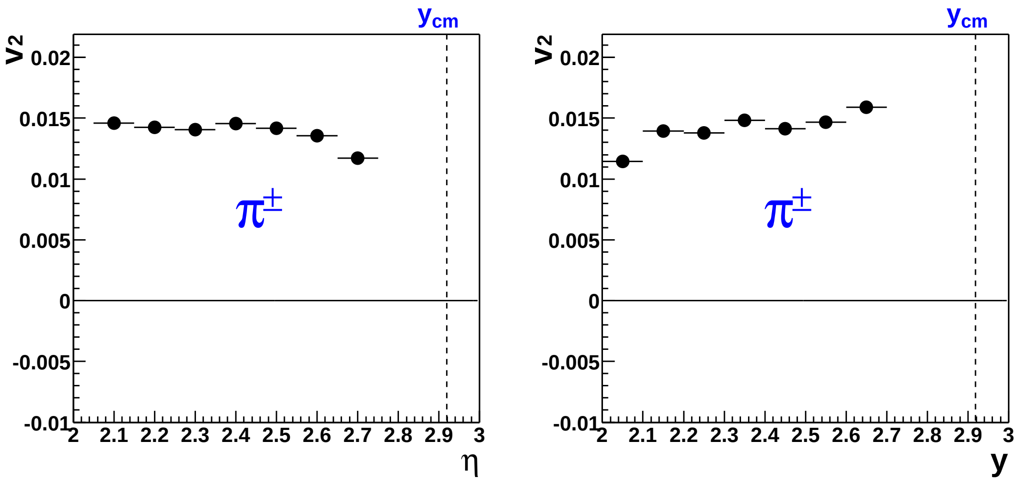

**Figure 6.9:** The $v_2$ values *vs* $\eta$ (left) and $y$ (right) for pions from all centralities taken together. The results are obtained using the 2 subevents method.

results derived from these two methods can give an estimation on the systematic errors in the $\pi^{\pm}$ elliptic flow analysis.

In Fig. 6.9 are shown the results on $\pi^{\pm}$ elliptic flow *vs* pseudorapidity (left) and rapidity (right) obtained using the 2 subevents method. The results are obtained from all centralities taken together. The rapidity and pseudorapidity dependence of $v_2$ is reasonable flat as one should expect in such a small rapidity window. The previous statement is practically completely fulfilled in the region $2.1 \leq y \leq 2.6$. A little bit bigger deviations from a flat behavior is at the edges of the rapidity/pseudorapidity distributions. The integrated magnitude of the pion elliptic flow is $\approx 1.4\%$ in that rapidity region.

The Plot in Fig. 6.10 shows the $p_T$ dependence of $\pi^{\pm}$ elliptic flow from all centralities taken together. The values of $v_2$ grow with $p_T$ going from 0 at $p_T = 0$ up to $\approx 4.0\%$ at

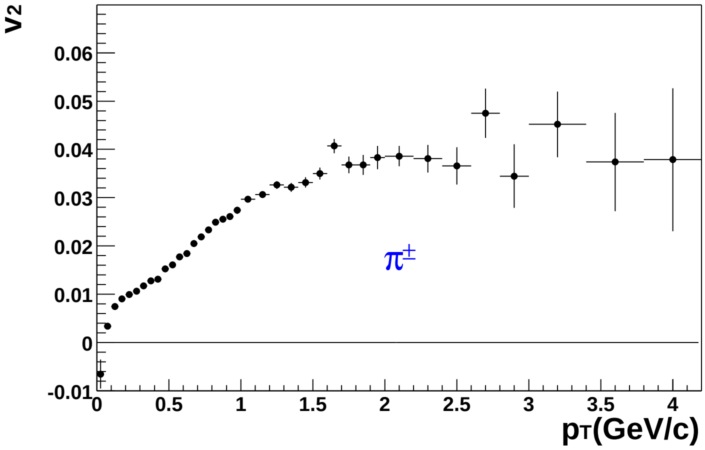

**Figure 6.10:** The pion $v_2(p_T)$ from all centralities taken together. The results are obtained using the 2 subevents method and not corrected for the HBT effect.

the highest $p_T$. It is observed that the pion elliptic flow saturates at $p_T \gtrsim 2$ GeV/c. The elliptic flow values at small $p_T$ do not have a $p_T^2$ like behavior due to the fact that the results are not corrected for the HBT effect. The topic of the next section is the influence of the HBT correlations on the flow measurements. There will be given an explanation of the procedure for the correction as well as the results corrected for the HBT effect.

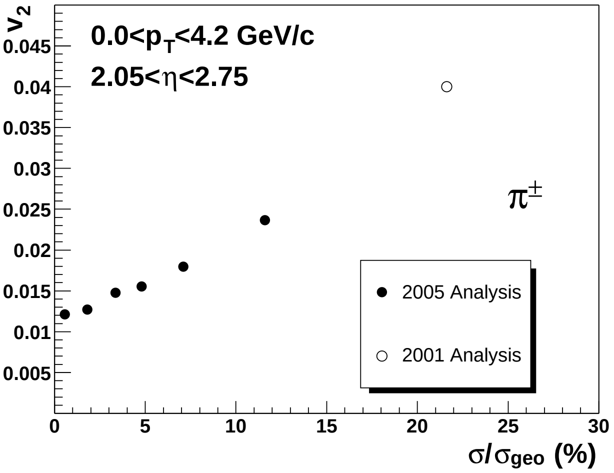

**Figure 6.11:** The $v_2$ values *vs* centrality. The closed circles denote the present analysis, while the open circle represents the older (completely independent) analysis. The result is not corrected for the HBT effect.

In Fig. 6.11 is shown the $v_2$ dependence on centrality. With closed circles is presented the result of the pion elliptic flow analysis done in 2005, while with open circle is represented a completely independent analysis done in 2001 [77]. There is a clear smooth transition between the results of these two analysis. The $v_2$ values, shown in Fig. 6.11, increase with centrality going from $v_2 = 1.2\%$ at very small $\sigma/\sigma_{geo}$ up to 4% for semicentral events with $20\% \leq \sigma/\sigma_{geo} \leq 40\%$ [1]. As the results are not corrected for the non-flow effects (for example, for the HBT effect), the offset of ≈ 1% at $\sigma/\sigma_{geo} \rightarrow 0\%$ can be explained as a consequence of these effects.

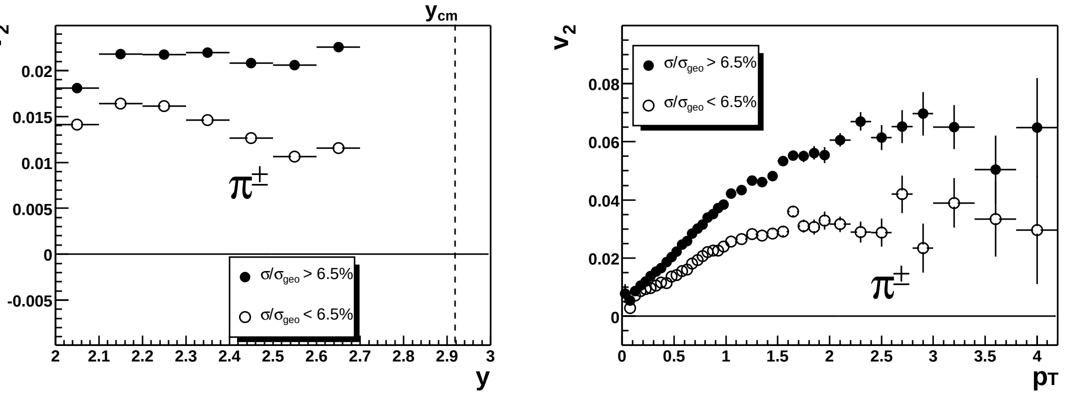

**Figure 6.12:** The pion elliptic flow *vs* rapidity (left) and $p_T$ (right) for central (closed circles) and semicentral (open circles) collisions.

In Fig. 6.12 are shown differential values of the pion elliptic flow *vs* $y$ and $p_T$ in semicentral and central collisions as discussed in Section 4.4. The trend of increasing of $v_2$ with centrality, which is already shown in Fig. 6.11, is visible in the differential distributions too. It seems that the shape of $v_2(y)$ distributions changes with centrality in

---

[1] Points are plotted at the center of gravity of the given centrality bin

a way that it becomes more flat with increasing of $\sigma/\sigma_{geo}$. In the case of $p_T$ dependence, it looks like that the $p_T$ threshold where $v_2$ starts to saturates increases with increasing of $\sigma/\sigma_{geo}$. In the case of the semicentral events the above mentioned threshold is around 2 GeV/c, while in the case of the central events it is around 1.5 GeV/c. Similarly as in the case of Fig. 6.10, the theoretically predicted [58] quadratical dependence of $v_2$ at small $p_T$ is not present at $v_2(p_T)$ distributions shown in and Fig. 6.12 (left).

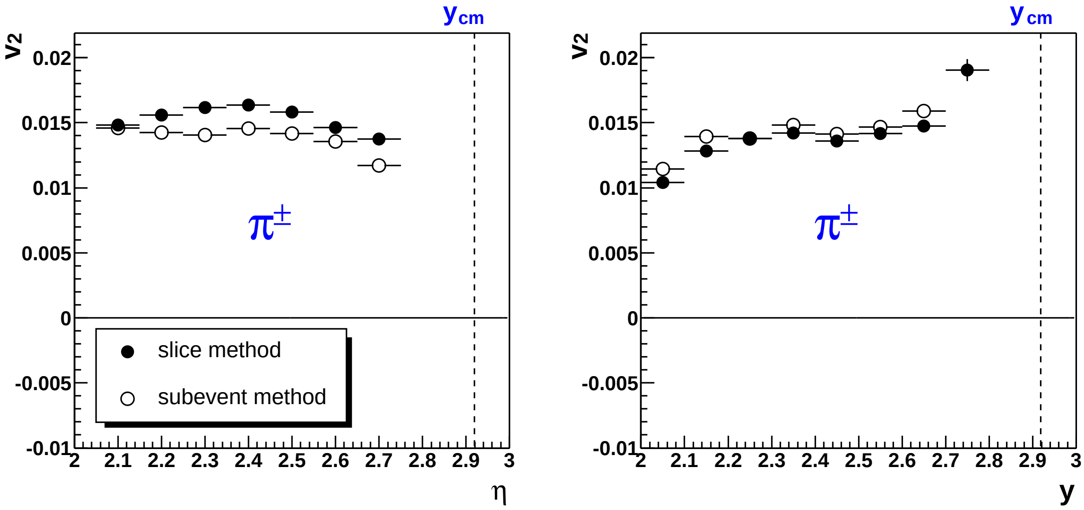

**Figure 6.13:** The pion elliptic flow *vs* pseudorapidity (left) and rapidity (right) calculated using the 'slice' (closed circles) and subevent method (open circles).

Fig. 6.13 shows the values of $\pi^{\pm}$ elliptic flow *vs* pseudorapidity (left) and rapidity (right) obtained using two, above mentioned, methods. The difference between them is rather small. The maximal difference of $\approx 0.002$ appears in $v_2(\eta)$, while the difference in $2.1 \leq y \leq 2.6$ region is negligible.

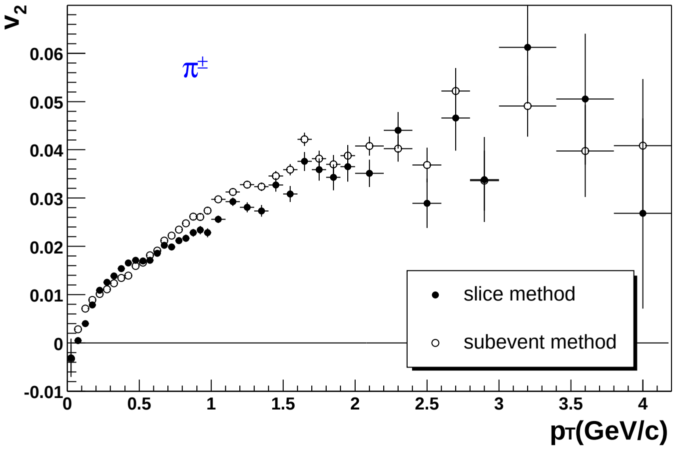

**Figure 6.14:** The pion elliptic flow *vs* transverse momentum calculated using the 'slice' and 2 subevents method.

The $p_T$ dependences of $\pi^{\pm}$ elliptic flow, shown in Fig. 6.14 are in a rather good agreement. The biggest difference of $\approx 0.004$ appears in the middle $p_T$ region around 1 GeV/c.

In Fig. 6.15 is shown the ratio (left panel) and the difference (right panel) between $v_2(p_T)$ dependences shown in Fig. 6.14. Although with some structure, the ratio is quite close to 1 and the difference is close to zero. From the described comparison between results obtained from two independent analysis methods one can conclude that the absolute systematic error in $\pi^\pm$ elliptic flow measurements is not bigger than 0.002. The corresponding relative systematic error is $\approx \pm 7\%$.

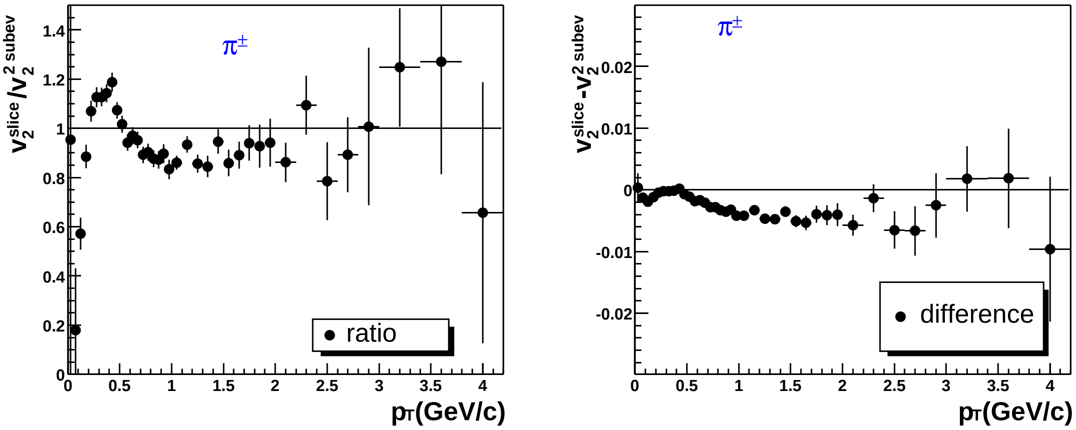

**Figure 6.15:** The ratio (left) and the difference (right) between $v_2(p_T)$ calculated using the 'slice' method and the 2 subevents method.

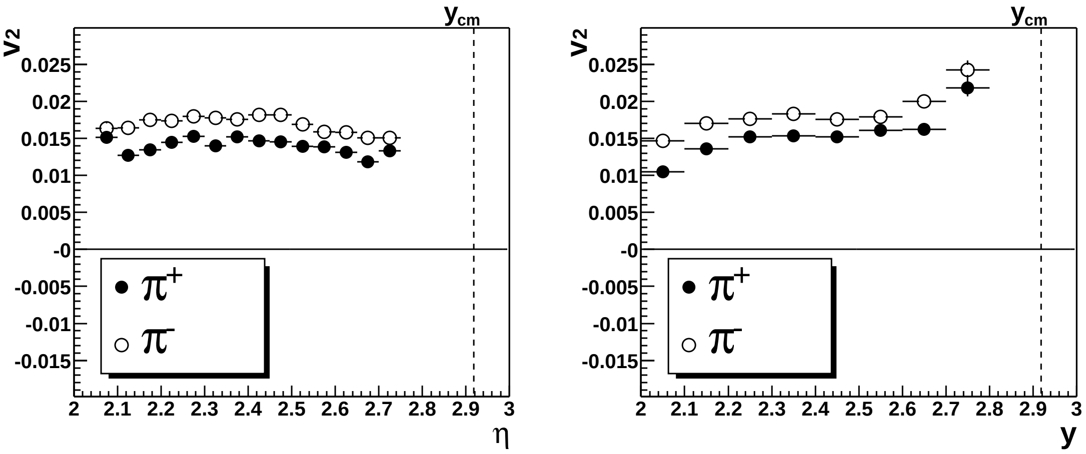

**Figure 6.16:** The $\pi^+$ (closed circles) and $\pi^-$ (open circles) elliptic flow *vs* pseudorapidity (left) and rapidity (right) for all centralities taken together.

Separately calculated elliptic flow of $\pi^+$ and $\pi^-$, using the 'slice' method, is shown in Fig. 6.16. Systematically it appears that $v_2(\pi^+) \leq v_2(\pi^-)$. The averaged difference is $\approx 0.003$ in both $\eta$ and $y$, what could be attributed to the contamination of protons in $\pi^+$ sample even after $dE/dx$ selection. From Fig. 6.1 one can see that protons cross the pion band at $1 \leq p \leq 3$ GeV/c and $200 \leq dE/dx \leq 250$. These low $p_T$ protons ($0.2 \leq p_T \leq 0.6$ GeV/c) contribute to the $\pi^+$ elliptic flow in a way to make it smaller. Assuming the equivalence between $v_2(\pi^+)$ and $v_2(\pi^-)$ and that protons contribute maximally with 0.15 in the total charged multiplicity one obtains that their elliptic flow is smaller than 0.004 which is in an accordance with results from the NA49 experiment in central collisions [78].

## 6.4 Elliptic Flow of Identified Protons

From Fig. 6.1 one can see that the low momentum protons can be clearly separated from other particle species. Particles with $p \leq 1$ GeV/c and $dE/dx \geq 400$ form a band which represents protons according to the nominal energy loss for protons calculated via the Bethe-Bloch formula[2]. In Fig. 6.17 is shown $p_T$ dependence of the elliptic flow of these protons. As it is expected for the elliptic flow of baryons for small $p_T$, the $v_2$ of protons is close to zero [78]. The importance of the proton elliptic flow analysis at this $p_T$ region will become more clear in Chapter 9 where the proton and the $\Lambda$ elliptic flow will be compared. As protons and $\Lambda$ have similar masses it is natural to expect that they have similar elliptic flow too. Due to that, as $\Lambda$ acceptance did not allow to measure $v_2(\Lambda)$ at low-$p_T$ region we will combine the elliptic flow of protons with the one from $\Lambda$ in order to cover the whole $p_T$ region.

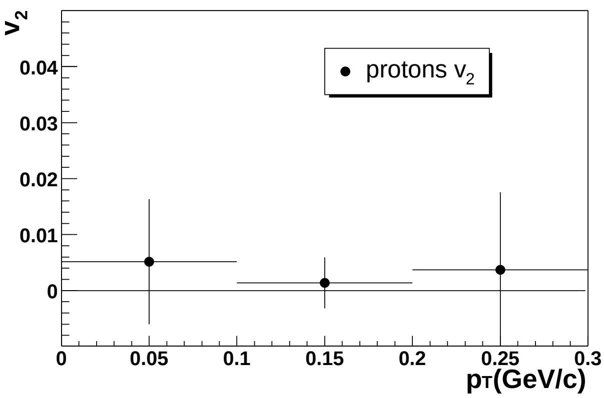

**Figure 6.17:** The identified proton elliptic flow *vs* $p_T$.

## 6.5 HBT Effects on the $\pi^{\pm}$ Elliptic Flow Measurements

The methods which are used in the measurements of the pion elliptic flow assume that the the only azimuthal correlations between pions are those arising from the pion correlation with the reaction plane. However, there are other, non-flow correlations which produce the azimuthal correlations between the pions. One of them, the most pronounced, is Hanbury-Brown and Twiss (HBT) quantum correlations which produce short range azimuthal correlations. Even in collisions with $b = 0$, the HBT correlations produce a spurious flow. This effect is especially important when pions are used for the reaction

---

[2] Although deuterons are visible in the same way, they are not included in this analysis due to the small statistics

plane reconstruction as it is the case in ultrarelativistic heavy-ion collisions experiments as CERES.

Ollitrault *et al.* in [58] have shown that the contribution to the flow arising from the HBT correlations can be subtracted. That correction significantly changes values and shape at the low $p_T$ region in $v_2(p_T)$ distribution. After the correction, $v_2(p_T)$ achieves a physically proper shape proportional to $p_T^2$ at low $p_T$.

In Section 3.3 has already been explained how, from a two-particle azimuthal distribution it is possible to extract the flow magnitude in a given $(p_T, y)$ window, or in other words, how to extract the differential values of the azimuthal anisotropic flow. The Fourier coefficients of the relative azimuthal distributions (3.15) are defined as

$$c_n(p_{T1}, y_1, p_{T2}, y_2) \equiv \langle \cos[n(\phi_1 - \phi_2)] \rangle \tag{6.1}$$

where $\phi_1$ and $\phi_2$ are the laboratory azimuthal angles of particles.

In general, the two-particle distribution can be written as

$$\frac{dN}{d^3\mathbf{p}_1 d^3\mathbf{p}_2} = \frac{dN}{d^3\mathbf{p}_1} \frac{dN}{d^3\mathbf{p}_2}(1 + C(\mathbf{p}_1, \mathbf{p}_2)) \tag{6.2}$$

where $C(\mathbf{p}_1, \mathbf{p}_2)$ is two-particle correlation function and decomposing it one can rewrite the coefficient $c_n$ given by Eq. (6.1) as

$$c_n(p_{T1}, y_1, p_{T2}, y_2) = c_n^{flow}(p_{T1}, y_1, p_{T2}, y_2) + c_n^{non-flow}(p_{T1}, y_1, p_{T2}, y_2) \tag{6.3}$$

where the first term, defined as a product of the Fourier coefficients $v_n$

$$c_n^{flow}(p_{T1}, y_1, p_{T2}, y_2) = v_n(p_{T1}, y_1) v_n(p_{T2}, y_2) \tag{6.4}$$

is due to the flow (see Section 3.3). Averaging $c_n^{flow}$, given by Eq. (6.4), over $(p_{T1}, y_1)$ and $(p_{T2}, y_2)$ within the experimental acceptance one obtains the integrated flow value:

$$v_n(\mathcal{D}) = \pm\sqrt{c_n(\mathcal{D}, \mathcal{D})} \tag{6.5}$$

Finally, integrating Eq. (6.4) over $(p_{T2}, y_2)$ one can get a relation between differential values of $c_n$ and Fourier coefficients $v_n$

$$v_n(p_{T1}, y_1) = \pm\frac{c_n(p_{T1}, y_1, \mathcal{D})}{\sqrt{c_n(\mathcal{D}, \mathcal{D})}} \tag{6.6}$$

In the presence of the HBT, the correlation function $C(\mathbf{p}_1, \mathbf{p}_2)$ has a non-zero value, and according to Eq. (6.1) will increase the contribution to the measured $c_n$ value. As this contribution originates from the HBT effect it will be denoted with $c_n^{HBT}$.

Considering only pions, since they are bosons, the correlation function $C(\mathbf{p}_1, \mathbf{p}_2)$ is positive. Assuming that there is no flow has as a consequence that $c_n^{flow} = 0$, but $c_n^{non-flow}$ is not zero and hence measured $c_n \neq 0$. In that way a spurious flow $v_n^{HBT}$ appears.

Let us estimate the order of the magnitude of $v_n^{HBT}$. The HBT effect between two identical pions with momenta $\mathbf{p}_1$ and $\mathbf{p}_2$ appears only if $|\mathbf{p}_2 - \mathbf{p}_1| \lesssim \hbar/R$ where $R$ is a typical size of the interacting zone. Now it is time to stress that the estimation and the proper numerical calculation of the HBT correction will be done in the natural system of units[3]where $\hbar = c = 1$. In the 2000 data taking period CERES measured rather central collisions with a typical value of the $R \sim 4.5$ fm [79]. Then $1/R \sim 45$ MeV which is more than for one order of magnitude smaller than the average $p_T$, which is about 500 MeV/c. It means that HBT affects only pairs with quite low relative momenta. So

$$\mathbf{p}_2 - \mathbf{p}_1 \sim \mathbf{p}(\phi_1 - \phi_2) \lesssim 1/R \tag{6.7}$$

or

$$(\phi_1 - \phi_2) \sim 1/p_T R \sim 0.09 = 5^\circ \tag{6.8}$$

Hence, on average, only pions with $\phi$ separation smaller than $\approx 5^\circ$ contribute to the HBT effect, or in other words the fraction of particles in $\mathcal{D}$ whose momentum lies in a circle of radius $1/R$ centered at $\mathbf{p}_1$. This fraction is $(R^3\langle p_T\rangle^2\langle m_T\rangle\Delta y)^{-1}$ where $m_T$ is the transverse mass defined as $m_T = \sqrt{p_T^2 + m^2}$ where $m$ stands for the particle mass. In the case of the CERES 2000 data, $\langle p_T\rangle \sim \langle m_T\rangle \sim 0.5$ GeV/c and $\Delta y \approx 0.7$ using Eq. (6.5) one obtains

$$|v_n^{HBT}(\mathcal{D})| \sim (\frac{1}{R^3\langle p_T\rangle^2\langle m_T\rangle\Delta y})^{1/2} \sim 0.03 \tag{6.9}$$

which has the same order of magnitude as the elliptic flow measured with the CERES spectrometer. Therefore, it is important to correct the measured flow for the HBT effect.

In order to get a more quantitative estimate of the $v_n^{HBT}$ in the following shortly the main points will be quoted of the procedure for the HBT correction without deriving the corresponding formulae[4]. Assuming the standard Bertsch-Pratt Gaussian parameterization of the correlation function

$$C(\mathbf{p}_1, \mathbf{p}_2) = \lambda e^{-q_s^2R_s^2 - q_o^2R_o^2 - q_L^2R_L^2} \tag{6.10}$$

after integration one obtains

$$c_n^{HBT}(p_{T1}, y_1, \mathcal{D}) = \frac{\lambda\pi^{3/2}}{R_sR_oR_L}\exp(-\frac{n^2}{4p_{T1}^2R_s^2})\frac{\frac{1}{m_{T1}}\frac{dN}{d^2\mathbf{p}_{T1}dy_1}}{\int_{\mathcal{D}}\frac{dN}{d^2\mathbf{p}_{T2}dy_2}d^2\mathbf{p}_{T2}dy_2} \tag{6.11}$$

At low $p_T$, one must do the following substitution in the previous equation

$$\exp(-\frac{n^2}{4p_{T1}^2R_s^2}) \to \frac{\sqrt{\pi}}{2}\chi e^{-\chi^2/2}(I_{\frac{n-1}{2}}(\frac{\chi^2}{2}) + I_{\frac{n+1}{2}}(\frac{\chi^2}{2})) \tag{6.12}$$

where $\chi = R_s p_T$ and $I_k$ is the modified Bessel function of order $k$. In the case of the elliptic flow Eq. (6.11, 6.12) become

---

[3] In natural system of units 1 fm corresponds to $5.076\ GeV^{-1}$

[4] For more details, see [58]

$$c_2^{HBT}(p_{T1}, y_1, \mathcal{D}) = \frac{\lambda \pi^{3/2}}{R_s R_o R_L} e^{-1/\chi^2} \frac{\frac{1}{m_{T1}} \frac{dN}{d^2\mathbf{p}_{T1} dy_1}}{\int_{\mathcal{D}} \frac{dN}{d^2\mathbf{p}_{T2} dy_2} d^2\mathbf{p}_{T2} dy_2} \tag{6.13}$$

with the substitution at low $p_T$ given by

$$e^{-1/\chi^2} \to \frac{\sqrt{\pi}}{2} \chi e^{-\chi^2/2} \left(I_{\frac{1}{2}}\left(\frac{\chi^2}{2}\right) + I_{\frac{3}{2}}\left(\frac{\chi^2}{2}\right)\right) \tag{6.14}$$

Our domain $\mathcal{D}$ is defined with: $0.05 \leq p_T \leq 4.2$ GeV/c, $2.05 \leq y \leq 2.75$ and $-\pi \leq \phi \leq \pi$. Also, assuming that 85% of detected charged particles are pions, half $\pi^+$ and half $\pi^-$, the right side of the Eq. (6.13) has to be multiplied with $0.85 \cdot 0.5$ which gives the probability that a particle in $\mathcal{D}$ is, let's say, $\pi^-$.

Now, one is ready to evaluate the contribution of HBT correlations $c_n^{HBT}$ and to subtract it from the measured correlation $c_n^{measured}$ in order to isolate the correlation due to the flow $c_n^{flow}$ in the following simple way

$$c_n^{flow}(p_{T1}, y_1, \mathcal{D}) = c_n^{measured}(p_{T1}, y_1, \mathcal{D}) - c_n^{HBT}(p_{T1}, y_1, \mathcal{D}) \tag{6.15}$$

where $c_n^{measured}(p_{T1}, y_1, \mathcal{D}) = v_n^{measured}(p_{T1}, y_1) v_n^{measured}(\mathcal{D})$. The corrected Fourier coefficients $v_n^{flow}$ can be obtained by converting back $c_n^{flow}$ into $v_n^{flow}$ via Eq. (6.6).

**Table 6.1:** The input values for $\lambda$, $R_s$, $R_o$ and $R_L$ for the HBT correction of the integrated $v_2$. The input values are obtained by averaging over centralities with $\sigma/\sigma_{geo} \leq 15\%$ and over $k_T \leq 0.6$ GeV/c.

| $\lambda$ | $R_s$ [fm] | $R_o$ [fm] | $R_L$ [fm] |
|---|---|---|---|
| 0.38 | 4.30 | 4.55 | 4.79 |

In Table 6.1 are given the input values for $\lambda$, $R_s$, $R_o$ and $R_L$ taken from [79] for the HBT correction of the integrated elliptic flow. The value of the integrated elliptic

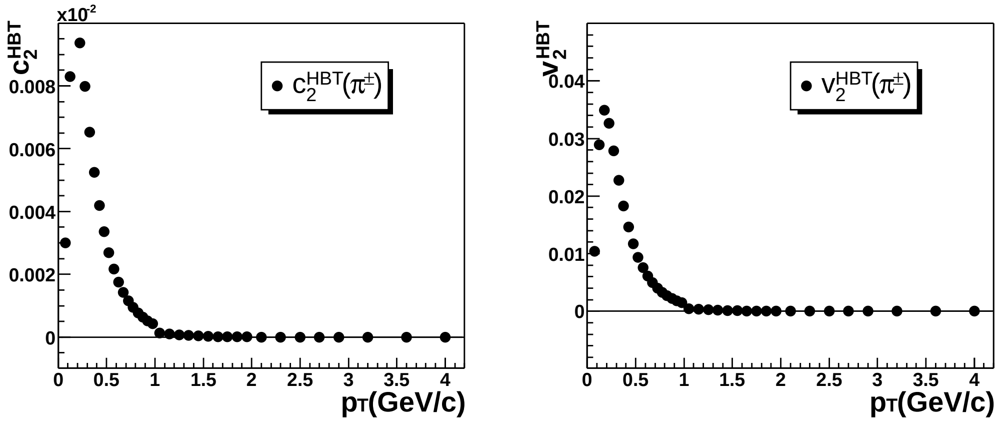

**Figure 6.18:** Left: the correlation coefficient $c_2^{HBT}$ *vs* $p_T$ calculated via Eq. (6.13). Right: the apparent $v_2^{HBT}(p_T)$ pion elliptic flow arising only from the HBT correlations calculated from $c_2^{HBT}(p_T)$.

flow before correction for the HBT effect was 0.0153. Several iterations of the correction procedure were done until the final value of the integrated elliptic flow corrected for the HBT effect became stable. That value is 0.0137 and it is 10% smaller with respect to the value before the correction for the HBT effect.

In the left panel of Fig. 6.18 are shown $c_2^{HBT}$ coefficients *vs* transverse momentum calculated using Eq. (6.13). In the right panel of Fig. 6.18 are shown values of the apparent flow $v_2^{HBT}(p_T)$ due to the HBT effect. The coefficients $v_2^{HBT}(p_T)$ are calculated using Eq. (6.6) where $c_2$ coefficients are substituted with the $c_2^{HBT}$. The biggest contribution of the HBT correlation effect is situated around 150 MeV/c. At $p_T = 0$ it has zero value. Then it is rising quickly up to its maximum, and then it is decreasing to the value close to zero already at $p_T = 1$ GeV/c.

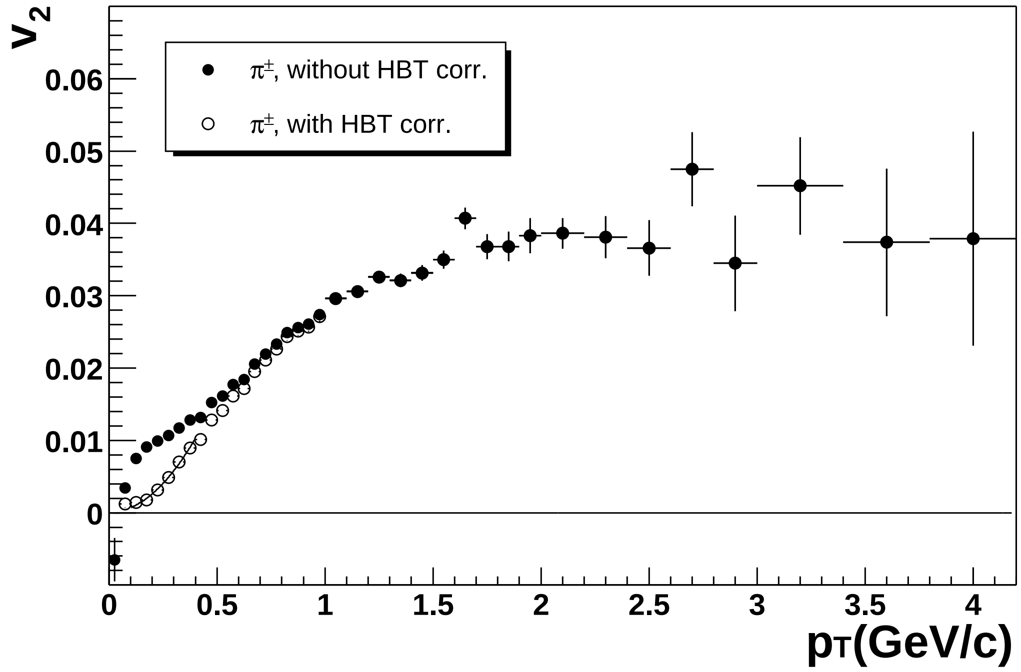

**Figure 6.19:** The pion elliptic flow *vs* $p_T$ before (closed circles) and after (open circles) correction for the HBT effect. A parabolic ($p_T^2$) fit is indicated with a full line.

In Fig. 6.19 the elliptic flow values, corrected for the HBT effect, are plotted against the transverse momentum (open circles). At the same Figure are also plotted the elliptic flow values uncorrected for the HBT effect (closed circles). The HBT corrected $v_2$ values are calculated via Eq. (6.15) and (6.6) where $c_2$ coefficients are substituted with the $c_2^{flow}$. As was expected, the correction affects only values of $v_2$ at low-$p_T$ up to 500 MeV/c. For $p_T \geq 0.5$ GeV/c it only slightly changes the values of the measured pion elliptic flow. For $p_T \geq 1.0$ GeV/c, the change is negligible. The correction did not only decrease the measured elliptic flow values but also it changed the shape of the $v_2(p_T)$ distribution. It changed it into a roughly $p_T^2$ like distributions which is physically expected. The peculiar behavior of the pion elliptic flow at low-$p_T$ disappears and now $v_2$ is compatible with a variation of type $v_2 \propto p_T^2$ up to $\approx 400$ MeV/c.

The correction of the $v_2(p_T)$ for the HBT effect could be done separately for each centrality bin too. In Table 6.2 are given values of $R_s$, $R_o$ and $R_L$ at different centrality bins [79]. Recalculated integrated values of the pion elliptic flow corrected for the HBT effect are shown in Fig. 6.20. As it is expected, the correction for the HBT effect decreases the elliptic flow values.

**Table 6.2:** The input values for $\lambda$, $R_s$, $R_o$ and $R_L$ for the HBT correction of the integrated elliptic flow. The input values are obtained by averaging over $k_T \leq 0.6$ GeV/c in different centrality bins.

|  | $R_s$ $[fm]$ | $R_o$ [fm] | $R_L$ [fm] |
|---|---|---|---|
| $0\% \leq \sigma/\sigma_{geo} \leq 5\%$ | 4.54 | 4.84 | 5.04 |
| $5\% \leq \sigma/\sigma_{geo} \leq 10\%$ | 4.32 | 4.52 | 4.78 |
| $10\% \leq \sigma/\sigma_{geo} \leq 15\%$ | 4.05 | 4.30 | 4.56 |

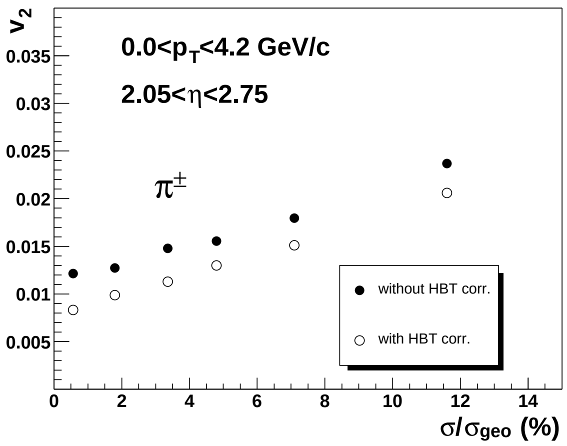

**Figure 6.20:** The integrated pion elliptic flow *vs* $\sigma/\sigma_{geo}$ calculated using the 2 subevents method corrected for the HBT effect.

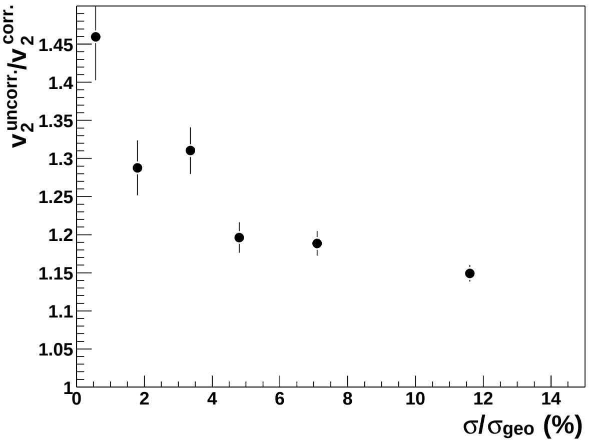

**Figure 6.21:** The ratio between the integrated pion elliptic flow uncorrected and corrected for the HBT effect *vs* $\sigma/\sigma_{geo}$ calculated using the 2 subevents method.

In Fig. 6.21 is shown the ratio between the values of the integrated pion elliptic flow before and after the correction for the HBT effect *vs* centrality. The biggest relative con-

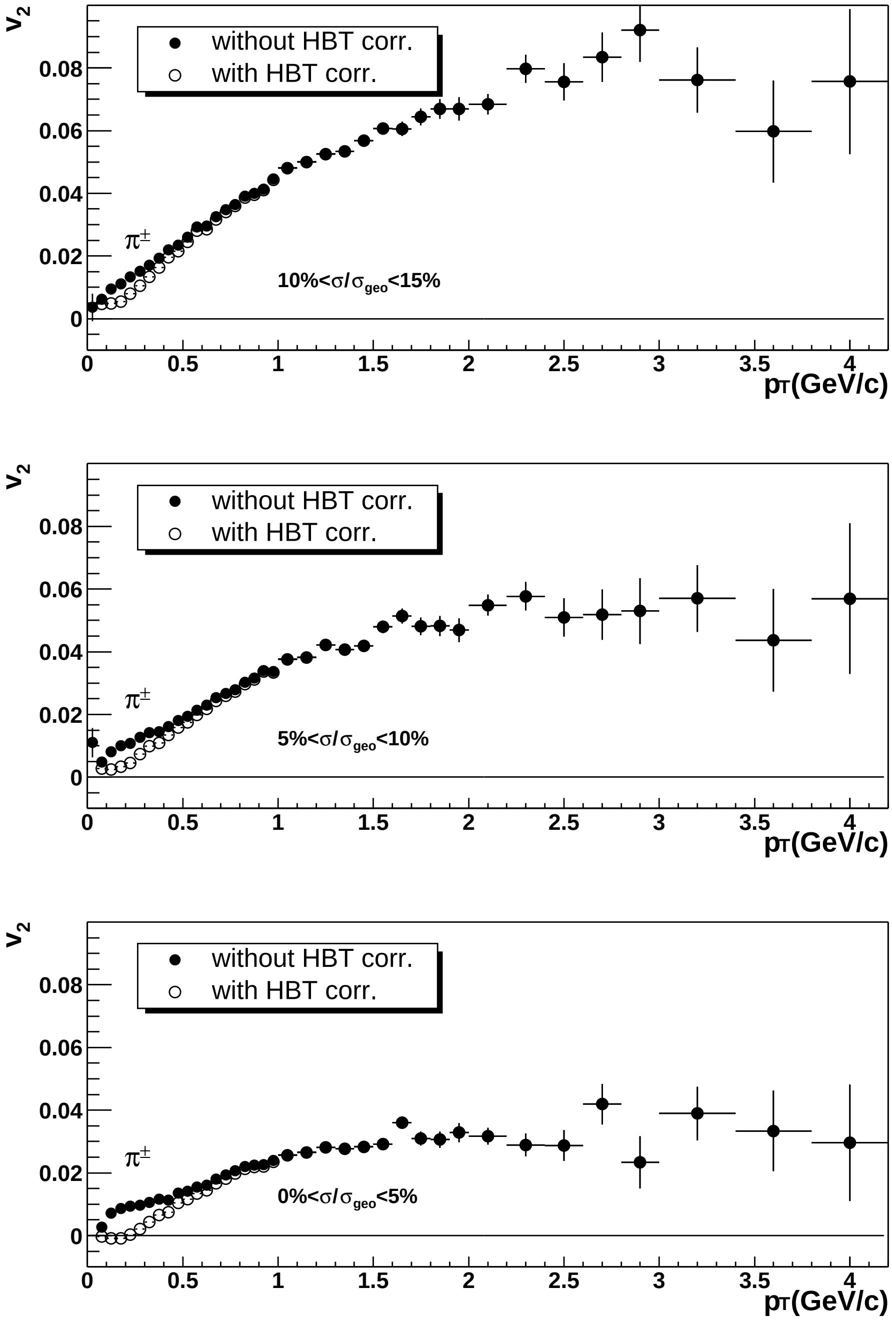

**Figure 6.22:** The pion elliptic flow *vs* the transverse momentum calculated using the 2 subevents method for 3 different centralities before (closed circles) and after (open circles) correction for the HBT effect.

tribution is visible in the most central events ($\approx$ nearly 50%). Going from the most central to the semicentral events, the HBT correction becomes smaller and in the last centrality bin with $\sigma/\sigma_{geo} \approx 12\%$, the relative decrease of the $v_2$ is only 15%. This observation is consistent with the expected physical behavior.

Applying the procedure for the HBT correction for 3 different centralities one obtains the plots similar to one shown in Fig. 6.19. In Fig. 6.22 are shown the corresponding plots. One can notice that going from semicentral to more central collisions, the HBT effect becomes more pronounced. That is already visible looking at $v_2(p_T)$ distributions for different centralities. For $10\% \leq \sigma/\sigma_{geo} \leq 15\%$ the uncorrected $v_2(p_T)$ is a linear function. There is no bump visible in the distribution. But the distribution does not have a shape proportinal to $p_T^2$ at small $p_T$. After subtraction the contribution which comes from the HBT effect the obtained shape at small $p_T$ became proportional to $p_T^2$. For more central collisions, a bump is visible, but after subtraction the contribution from the HBT effect it disappears completely and corrected distributions have a $p_T^2$ like shape.

At the end of this section one has to notice that the $v_2$ values obtained from the 'slice' method were not corrected for the effect of HBT correlation. The reason is that the method itself removes the HBT effect partly. From the rough estimation given in Eq. (6.8), the HBT affects the data only within a narrow $\Delta\phi$ region of $\pm 2.5°$. As in the 'slice' method the pion elliptic flow is calculated via the combining particles from non-adjacent slices where minimal $\Delta\phi$ is $1°$ it is clear that a big part of the HBT effect is removed automatically. Taking into account that particles are also distributed in $\theta$ makes the above spatial separation between particles even bigger. That is visible from Fig. 6.14 where the $v_2(p_T)$ values obtained from two methods are compared. At small $p_T$ (smaller than 150 MeV/c) $v_2$ obtained from the 'slice' method are smaller than those obtained from 2 subevent method uncorrected for the HBT effect. The most natural explanation is that the method itself, just due to the slicing, removes the HBT influence at a small enough $p_T$. With the increasing of $p_T$, this advantage of the method slowly disappears.

# Chapter 7

# FLOW ANALYSIS OF $\Lambda$ PARTICLES

Most of the anisotropic flow measurements available in the systematics are done for non-strange particles [39,49,55,80–83]. At very low collision energies directed flow of strange particles was measured [80, 84–88]. Recently, at very high RHIC energies [89] elliptic flow of strange particles ($K_S^0$, $\Lambda$, $\Xi$, and $\Omega$) was measured. At the CERN SPS a few measurements of transverse radial flow in Pb+Pb collisions at $\sqrt{s_{NN}} = 17$ GeV/c [90,91] were done. In order to explain a quantitative difference in the transverse radial flow between multi-strange baryons and non-strange hadrons was proposed a physical picture in which multi-strange baryons do not take part in a common expansion and thus decouple early from the system [92]. This explanation also suggests that via the investigation of the elliptic flow of strange particles one can have an insight into very early stages of the collisions.

In this Chapter will be presented results of the anisotropic transverse flow measurements of $\Lambda$ particles emitted in Pb+Au collisions at $\sqrt{s_{NN}} = 17$ Gev/c using the method which is partially described in Section 3.4. Some specific features of this analysis, like the reaction plane determination and autocorrelation effect, construction of $\Lambda$ elliptic flow pattern and extraction of *observed* flow coefficients, will be presented in detail because they are not part of the standard reaction plane method.

This Chapter will start with the identification of $\Lambda$ daughters particles. The main part of the contents of Section 7.1 is the reconstruction of $\Lambda$ particles and the characteristics of the obtained signals. In the Section 7.2, the reaction plane reconstruction and its resolution will be presented in detail. Finally, in the last Section 7.3 of this Chapter, the results on $\Lambda$ elliptic flow measured as a function of rapidity, transverse momentum and the collision centrality will be presented.

## 7.1 Particle Selection and $\Lambda$ Reconstruction

The $\Lambda$ particles were reconstructed via the decay chanel $\Lambda \rightarrow p + \pi^-$ with a $BR = 63.9\%$ and $c\tau_\circ = 7.89$ cm [70]. In order to estimate a systematic error in the measurement of the elliptic flow of $\Lambda$ hyperons, two different analysis were performed. In both of them many cuts, listed below, which are applied in order to maximize the significance, were the same. One cut, which was used in order to eliminate the contribution of $\pi^+$ in a proton sample was essentially different. In the first case, which will be called Run I, was applied a sharp cut on the transverse momentum of positive particles ($p_T > 0.4$ GeV/c) together with a sharp opening angle $\theta_{p\pi^-}$ cut ($\theta_{p\pi^-} \geq$ 0.015). In that way, protons with $dE/dx \approx 200$ and $p \lesssim 2$ GeV/c which overlap with positive pions at approximately the same $dE/dx$ and momentum were excluded from the analysis. This as a consequence had a more pronounced $\Lambda$ signal above the combinatorial background, but from the other side, many $\Lambda$ particles in that case were excluded from the analysis. In the second case, which will be called Run II, in order to increase the number of $\Lambda$ particles for the elliptic flow analysis was applied combined $p_T$ dependent opening angle $\theta_{p\pi^-}$ cuts. Using the kinetic generator [93], $\Lambda$ decays were simulated and for all rapidity bins in which $\Lambda$ was reconstructed two dimensional $\theta_{p\pi^-}$ *vs* $p_T$ distributions were formed. Based on them was possible to establish a set of $p_T$ dependent opening angle cuts which were used in order to partially remove positive pion contribution from the proton sample. As a price the $\Lambda$ statistics is increased twice, but the signal integrated over $y$ and $p_T$ has been less pronounced with respect to the Run I.

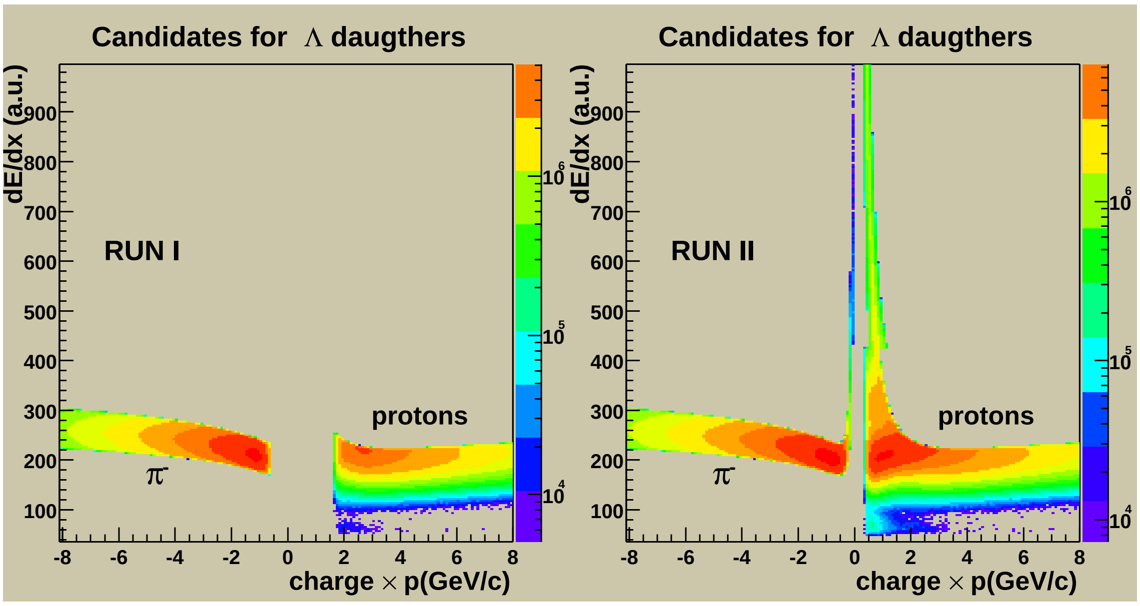

**Figure 7.1:** Left: Partially identified $\pi^-$ and protons in the case of a sharp cut on the transverse momenta of positive particles and a sharp opening angle cut (Run I). Right: Partially identified $\pi^-$ and protons in the case were combined $p_T$ dependent opening angle $\theta_{p\pi^-}$ cuts have been applied.

As candidates for $\Lambda$ daughters were chosen only those TPC tracks which satisfied several simple cuts[1] listed below.

1. Due to late decay of $\Lambda$ particle, TPC and SDD segment of daughter track should not match within $\pm 3\sigma$ window.

2. Radial distance from the daughter track to the vertex position in the $x - y$ plane had to be bigger than $3.0$ cm. This is an additional cut used in order to exclude the

---

[1] Overall quality criteria on particle track were the same as in Subsection 4.3.1

vertex tracks[2].

3. Partial identification of particles was determined by $dE/dx$ cut. Protons were selected as positive particles with $dE/dx$ smaller than $1.1 \cdot dE/dx(protons)$, which corresponds to $+1\sigma$ boundary. Negative pions were selected as negative particles with $dE/dx$ between $0.85 \cdot dE/dx(\pi^-)$ and $1.15 \cdot dE/dx(\pi^-)$, which corresponds to $\pm 1.5\sigma$ boundary. The nominal energy loss $dE/dx(protons)$ and $dE/dx(\pi^-)$ were calculated according to the appropriate Bethe-Bloch formulae. In Fig. 7.1 (left) one can see partially identified $\pi^-$ and protons in the case of a sharp cut on the transverse momenta of positive particles and a sharp opening angle cut (Run I) after applying the described $dE/dx$ cuts. On the right side of Fig. 7.1 are shown partially identified protons and negative pions after the $dE/dx$ cuts were applied in the case of combined $p_T$ dependent opening angle $\theta_{p\pi^-}$ cuts (Run II).

4. In order to suppress the contamination of $K^0_S$, an Armenteros-Podolanski cut [94] with $q_T \leq 0.125$ GeV/c and $0.0 \leq \alpha \leq 0.65$ was applied. In Fig. 7.2, as a 2-dimensional $\alpha - q_T$ distribution, are shown $\Lambda$, $\bar{\Lambda}$ and $K^0_S$ reconstructed from the experimental data [6]. In the case of the $\Lambda$ particle, the $\alpha$ variable is defined as $\alpha = (q^+_L - q^-_L)/(q^+_L + q^-_L)$ where $q^+_L$ and $q^-_L$ are the longitudinal momentum components of $\vec{p}^+$ and $\vec{p}^-$ calculated with respect to the $\vec{p}_\Lambda = \vec{p}^+ + \vec{p}^-$. The $q_T$ variable is defined as the momentum component of $\vec{p}^+$ in the transverse plane perpendicular to the $\vec{p}_\Lambda$. In the case of the $\bar{\Lambda}$ ($K^0_S$) particle one should exchange $\vec{p}_\Lambda$ with $\vec{p}_{\bar{\Lambda}}$ ($\vec{p}_{K^0_S}$) in the above definitions.

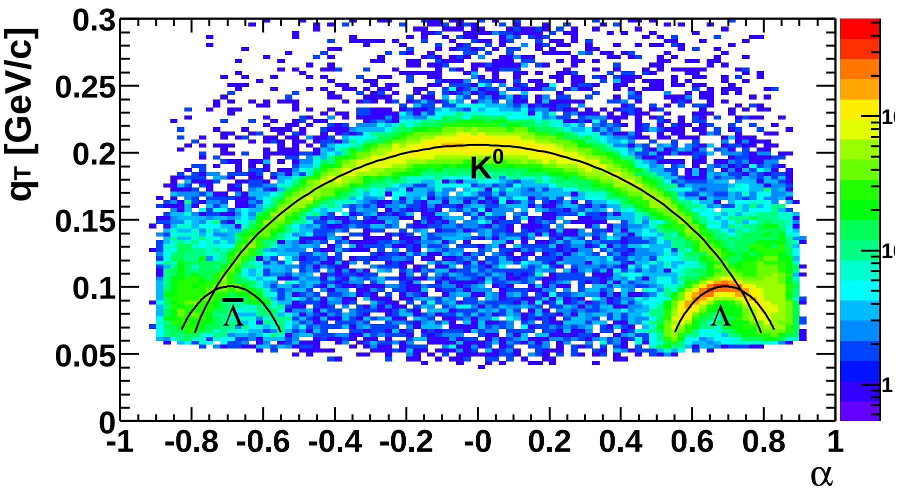

**Figure 7.2:** Armenteros-Podolanski plot shows $\Lambda$, $\bar{\Lambda}$ and $K^0_S$ reconstructed from the experimental data. The Figure is taken from [6].

In order to remove the effect of autocorrelation, tracks which were chosen to be candidates for $\Lambda$ daughter particles were not included into the determination of the ori-

---

[2] For the first and the second item, the opposite condition is required in the case of $\pi^\pm$ elliptic flow analysis (see Subsection 4.3.1)

entation of the reaction plane. Anyhow, they are well separated because $\Lambda$'s daughter particles do not point into vertex due to rather long time of half life of $\Lambda$ ($\tau_\Lambda = (2.632 \pm 0.020) \cdot 10^{-10}$ s).

For the flow measurements, the topology of the event is important, especially the multiplicity and the position of the reaction plane. In order to completely preserve the topology, the mixed events technique was not used for the combinatorial background calculation, but rather the same event technique. Additionally, this way is much more efficient due to consuming much less CPU time and hence faster computing. The combinatorial background was determined by rotating positive $\Lambda$'s daughter tracks by $180^\circ$ around the beam axis and constructing the invariant mass distribution. By such a rotation of positive daughter tracks around the beam axis all real $\Lambda$ vertexes were destroyed. In order to decrease the statistical errors, instead of one rotation for $180^\circ$, ten of them by a random angle were performed. The shape of the combinatorial background was unchanged in both cases.

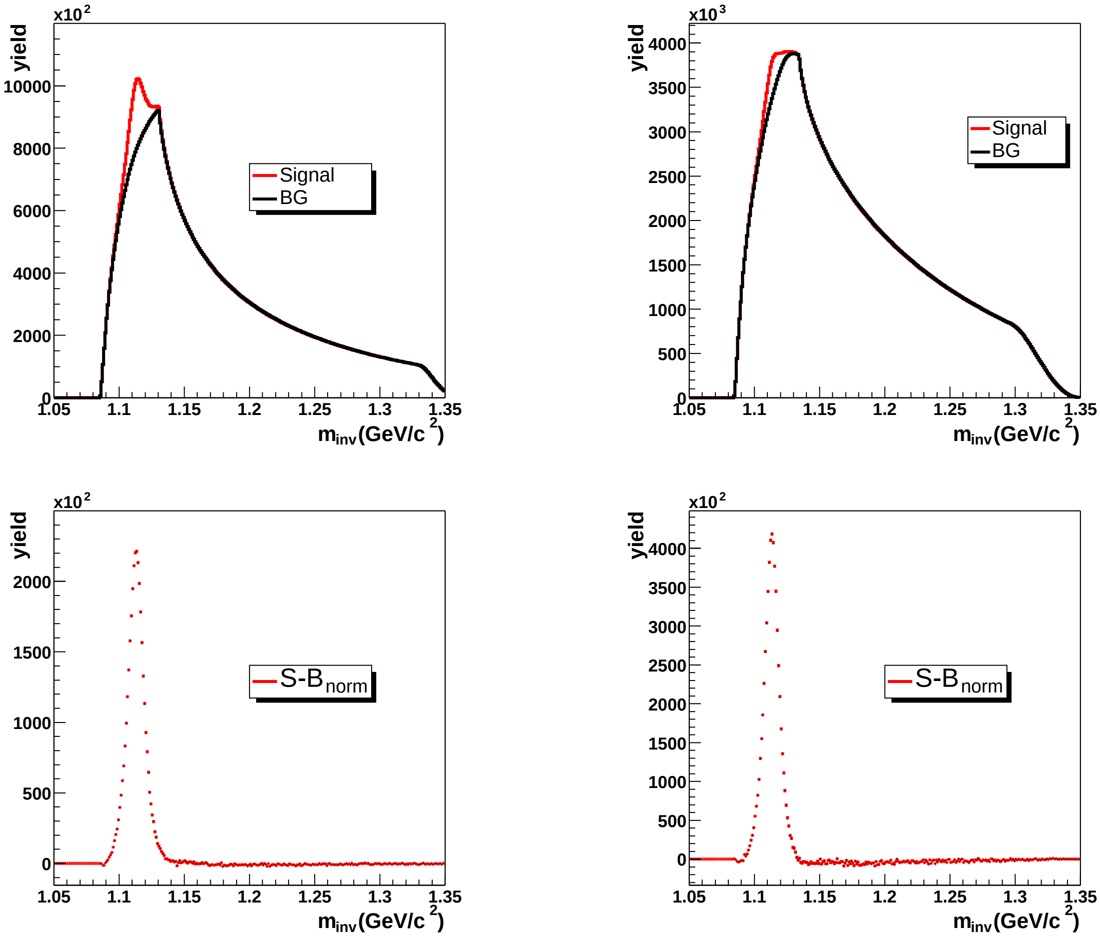

**Figure 7.3:** Left: Run I. Top: the invariant mass distribution of the signal and the normalized combinatorial background. In the region of the $\Lambda$ mass a pronounced signal is observed. Bottom: the invariant mass distribution of the signal after subtraction of the normalized combinatorial background. Right: Run II. Top: A small enhancement of the signal is visible in the region of the $\Lambda$ mass. Bottom: the invariant mass distribution of the signal left after subtraction of the normalized combinatorial background.

For two different ways of $\Lambda$ reconstruction (Run I and II) in Fig. 7.3 are shown the invariant mass distribution of the signal and the normalized combinatorial background as well as the invariant mass distribution of the signal after subtraction the normalized combinatorial background. The distributions show that in the case of Run I the signal is much more pronounced then in the case of Run II, but the yield of $\Lambda$ is twice higher in the case of Run II with respect to the case of Run I as it is explained above.

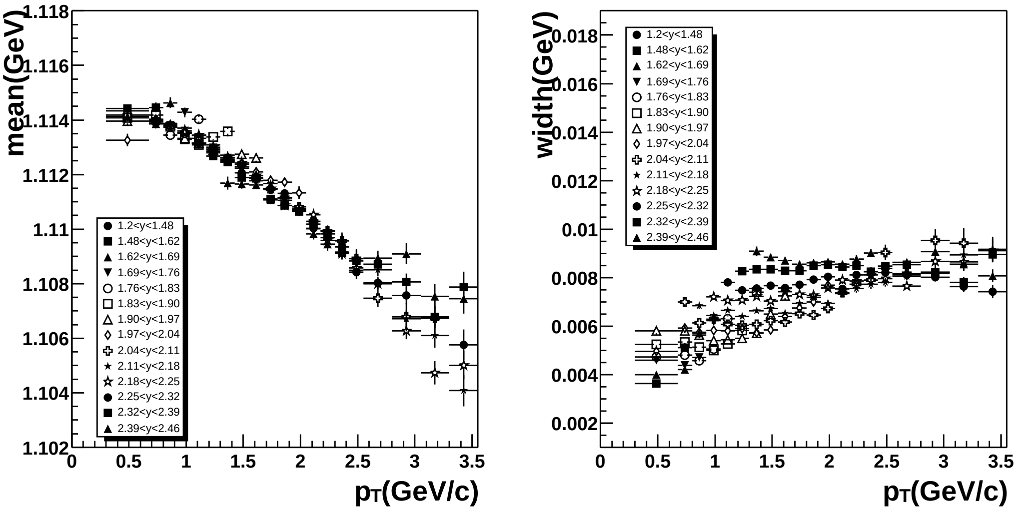

**Figure 7.4:** Left: mass of $\Lambda$ in function of $p_T$ for different rapidities displayed with different symbols. Right: the same dependences in the case of width of $\Lambda$

The pure $\Lambda$ signal shown at the bottom part of Fig. 7.3 does not have a Gaussian shape (this is a convolution of several Gaussians). This is a consequence of the fact that the observed mass and width of $\Lambda$ particles depend on $p_T$ and $y$, because the displaced secondary vertex is not used for recalculation of the angles. Due to that, the analysis was done separately in $p_T - y$ windows which are small enough that the mass and width of $\Lambda$ particles are practically constant. In each of these small $y - p_T$ windows the procedure of $\Lambda$ reconstruction was performed in order to extract the mass and width of $\Lambda$. The signal distributions were fitted with a *Gaussian + a constant* and in this case the best $\chi^2$ values were obtained[3]. In Fig. 7.4 is displayed the mass and width of $\Lambda$ as a function of $p_T$ of $\Lambda$ for different rapidity bins. The mass of $\Lambda$ particles strongly depends on $p_T$ and practically does not depend on rapidity, while in the case of $\Lambda$'s width both dependences are present. Once the mass and width of $\Lambda$ were established for a given $y$ and $p_T$ they were kept as constants for the rest of the analysis.

With the cuts, listed above, the optimal values for $S/B \approx 0.04$ and $S/\sqrt{B} \approx 500$ were obtained. Here $S$ stands for the signal and $B$ for the combinatorial background. Before continuation of the presentation of the $\Lambda$ reconstruction one should stress that $S/B$ and significance (defined as $S/\sqrt{B}$) strongly depends on the transverse momentum of $\Lambda$ particle. In Fig. 7.5 these quantities are displayed as a function of applied cuts. First point corresponds to the distributions before any cut was applied. The second one represents

---

[3] The results obtained by fitting with a *Gaussian + a slope* were a little bit less satisfactory

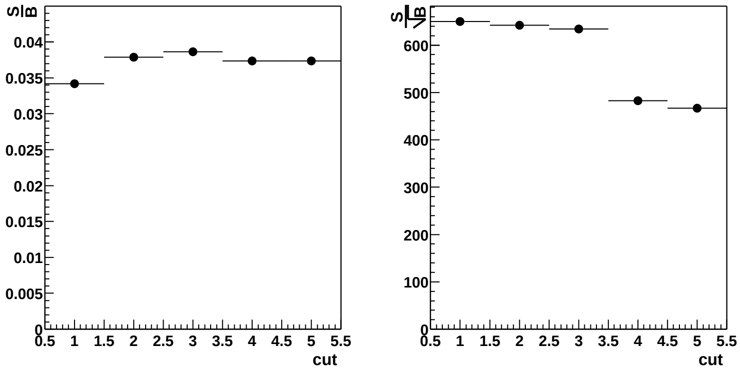

**Figure 7.5:** Left: $S/B$ as a function of applied cuts (for the correspondence between the depicted points and the applied cuts see the text below). Right: the same dependences in the case of the significance $S/\sqrt{B}$.

the cut on the acceptance edges. All $y - p_T$ bins, where the number of reconstructed $\Lambda$ was extremely small, were cutted off in the analysis. In Fig. 7.7 it is represented with non-colored area. The third, main cut was Armenteros-Podolanski cut what is visible with a drop of $S/B$ and $S/\sqrt{B}$ values. This cut was necessary in order to suppress the $K_S^0$ contamination. Last two cuts represent the opening angle cuts *vs* proton and pion $p_T$. In Fig. 7.6, $S/B$ and $S/\sqrt{B}$ as a function of $p_T$ for different rapidities are displayed with different symbols. There is practically no rapidity dependence of $S/B$, while $S/\sqrt{B}$ shows significant rapidity dependence. Concerning the $p_T$ dependence, $S/B$ goes from values close to $0$ at small $p_T$ up to values close to $1$ at the highest $p_T$. The biggest values of the significance $S/\sqrt{B}$ are situated at $p_T \approx 1 - 1.5$ GeV/c with $y \approx 2$ what is the consequence of the fact that it is the most populated area in $y - p_T$ distribution of the reconstructed $\Lambda$ (see Fig. 7.7).

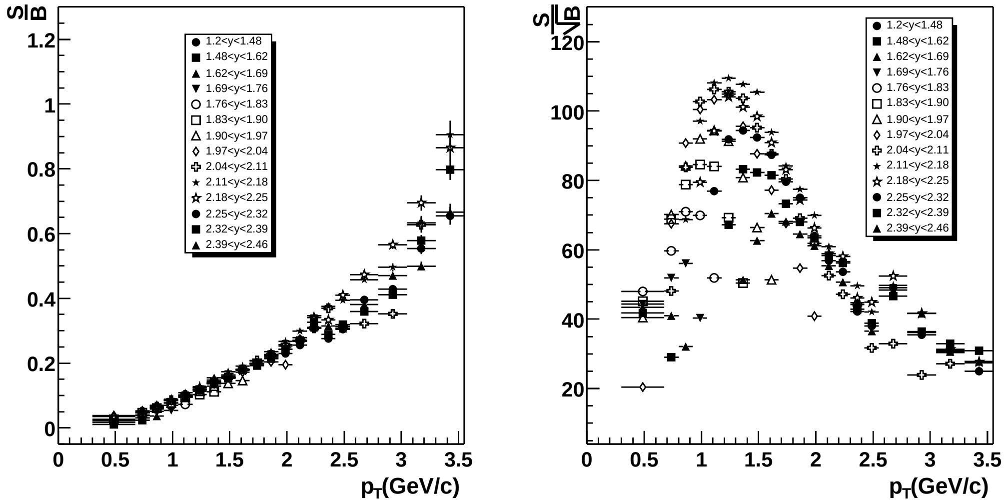

**Figure 7.6:** Left: $S/B$ as a function of $p_T$ for different rapidities displayed with different symbols. Right: the same dependences in the case of the significance $S/\sqrt{B}$.

In Fig. 7.7 is shown $\Lambda$ acceptance after these cuts were applied. The $\Lambda$ particles used for the elliptic flow analysis are from the kinematic region $1.6 \leq y \leq 2.6$ and

$0.3 \leq p_T \leq 3.5$ GeV/c. This region does not cover the whole kinematic region shown in Fig. 7.7. The $\Lambda$ particles with small $p_T$ and at small rapidities were not included because they are reconstructed with a quite small value of $S/B$ and significance $S/\sqrt{B}$.

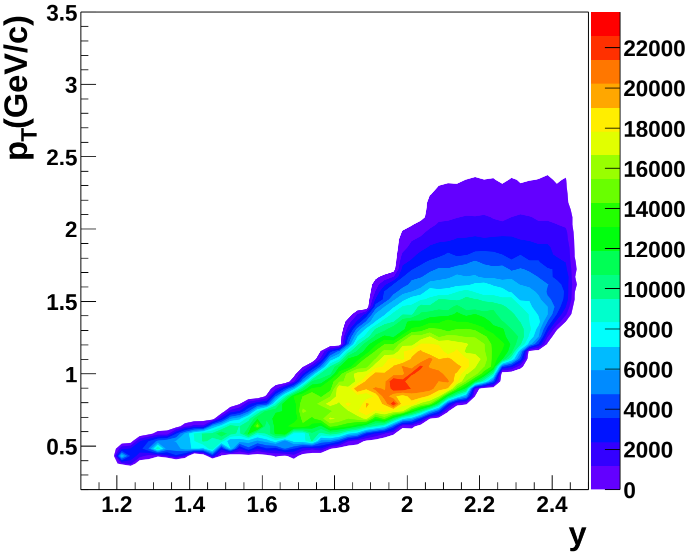

**Figure 7.7:** Distribution of accepted $\Lambda$ in $y - p_T$ space.

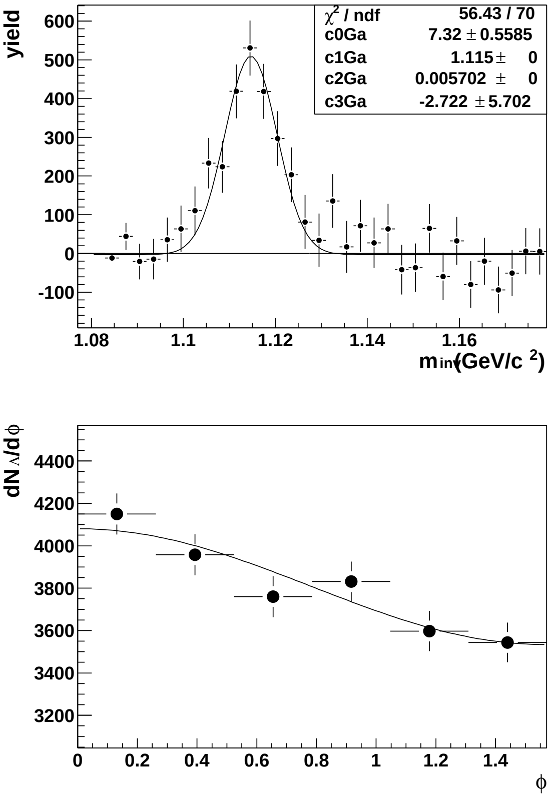

**Figure 7.8:** Top: $\Lambda$ reconstructed for $1.62 \leq y \leq 1.69$, $0.675 \leq p_T \leq 0.8$ GeV/c and $15° \leq \phi \leq 30°$. Bottom: Elliptic flow pattern reconstructed from the $\Lambda$ yield in $\phi$ bins for $p_T \approx 2.7$ GeV/c.

The area under the peak in the invariant mass distribution was used to measure the yield of $\Lambda$ particles in different $y$, $p_T$ and $\phi$ bins[4]. The above mentioned yield was obtained by subtracting a normalized combinatorial background from the corresponding signal distributions. In the top part of Fig. 7.8 is shown an example of such a distribution. Plotting the yield versus $\phi$ for different $p_T$ and $y$ values one can construct $dN_\Lambda/d\phi$ distribution (Fig. 7.8 bottom). Fitting these distributions with a cosine function $c[1+2v_2' \cos(2\phi)]$, it is possible to extract the observed elliptic flow values $v_2'$ for different $p_T$ and $y$ and hence to obtain differential dependences of $v_2$ versus $p_T$ and $y$ which is the main goal of this analysis. Of course, in order to get the proper elliptic flow magnitude, the obtained $v_2'$ coefficients were corrected for the reaction plane resolution via $v_2 = v_2'/\sqrt{2\langle\cos[2(\Phi_1 - \Phi_2)]\rangle}$ as it was explained in Section 3.2.3.

## 7.2 Reaction Plane Determination and its Resolution

At the top SPS energy and with rather central events which were analyzed, it is correct enough to assume that the only significant azimuthally anisotropic flow is the elliptic flow of particles. With such a supposition, azimuthal distributions of particles with respect to the true reaction plane orientation ($\Psi$) can be written as a Fourier decomposition where the only elliptic flow component ($v_2$) has a non-zero value

$$E\frac{d^3N}{d^3p} = \frac{d^2N}{p_T dp_T dy}\frac{1}{2\pi}\{1 + 2v_2\cos[2(\phi - \Psi)]\} \tag{7.1}$$

Using that supposition, the reaction plane was determined by measuring the corresponding orientation (i.e. the azimuthal angle $\Phi$) from the second Fourier harmonic

$$\Phi = \frac{1}{2}\arctan\left(\frac{\sum_i p_{Ti}\sin(2\phi_i)}{\sum_i p_{Ti}\cos(2\phi_i)}\right) \tag{7.2}$$

according to the Eq. (3.4) and (3.5) [5]. As it was already mentioned, in order to avoid the autocorrelation effect for the reaction plane determination were used only those particles which are not candidates for $\Lambda$ daughters, i.e. were used only primary vertex tracks. The flattening of the reaction plane was done by recentering and Fourier Expansion of $dN/d\Phi$ distribution in exactly the same way as in the case of the pion analysis which was described in Section 6.2. The results of subsequent application of the flattening procedure mentioned above are shown in Fig. 7.9. Again, as in the case of pion flow analysis, big non-uniformity in the 'raw' reaction plane distribution is a consequence of a deep in $\phi_{lab}$ distribution due to the fact that in the case of one TPC chamber 1/3 of its electronics did not work. The flattening procedure is performed for 9 (6) centrality bins in the case of Run I (II). The obtained results (in the case of Run I) are shown in Fig. 7.10.

In order to find the resolution of the measured reaction plane each event [6]was randomly divided into two subevents. The corresponding reaction planes reconstructed from these subevents were correlated using the $\cos[2(\Phi_1 - \Phi_2)]$ variable. Here, $\Phi_1$ and $\Phi_2$ stands for the azimuthal angles of the reaction planes reconstructed in the subevents. From this, using Eq. (3.13) the resolution was calculated. As the resolution depends on centrality

---

[4] Here $\phi$ is the azimuthal angle of the reconstructed $\Lambda$ measured with respect to the reaction plane.

[5] For the weight is chosen $p_{Ti}$, transverse momentum of the given, $i$-th, particle.

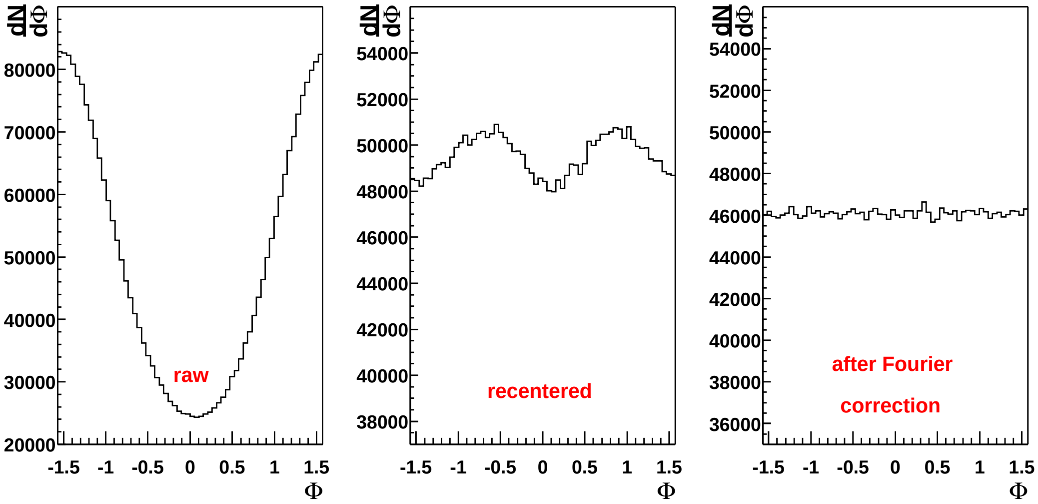

**Figure 7.9:** Example of flattening of the calculated reaction plane $(\Phi)$ in one of 6 centrality bins (Run II).

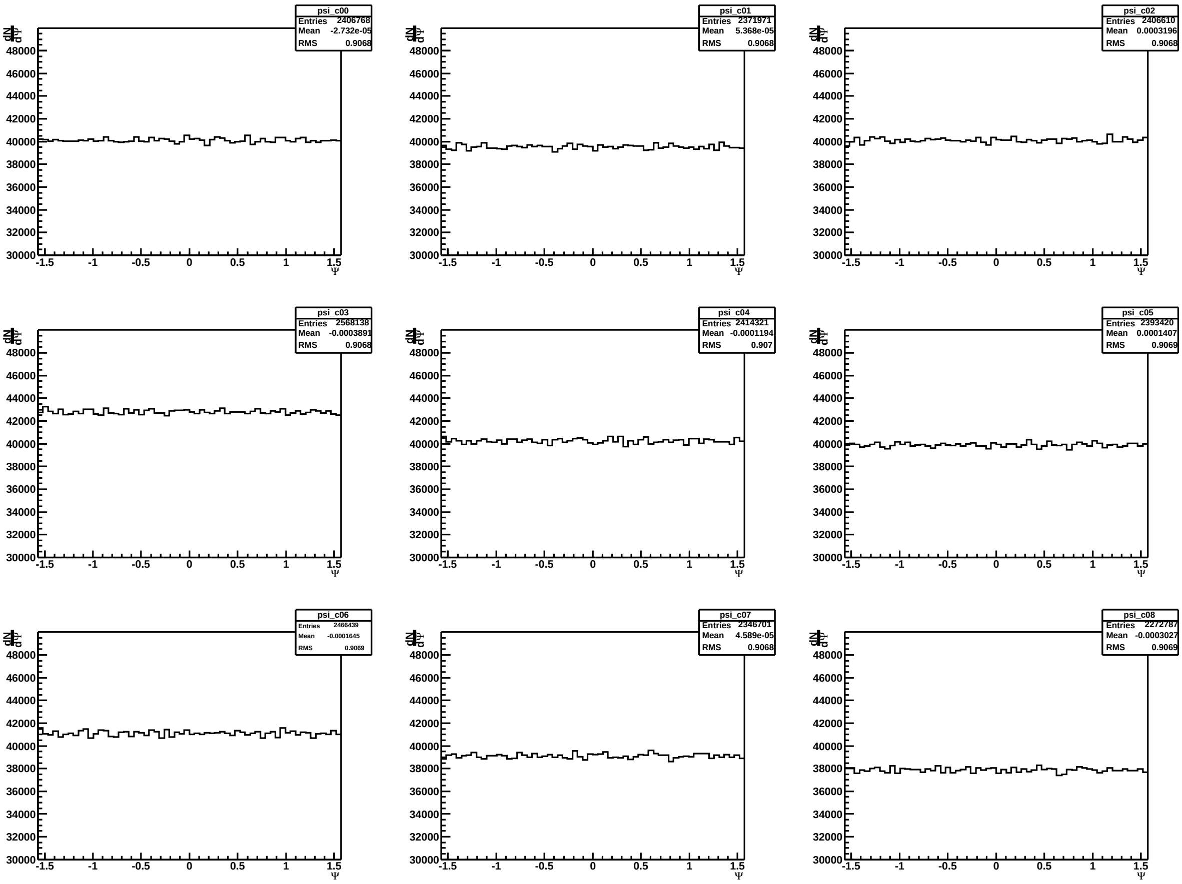

**Figure 7.10:** Corrected $dN/d\Phi$ distribution for 9 different centralities (Run I) as a function of the reaction plane angle $\Phi$ calculated using the Eq. (7.2).

(via the elliptic flow which decreases with centrality), in the above described way the resolution was calculated for each centrality bin separately. The resolution goes from 0.16 (semicentral events) to 0.31 (very central events).

The correction factor, which one has to use in order to correct the observed Fourier harmonics for the finite reaction plane resolution, is defined as an inverse value of the corresponding reaction plane resolution. In Fig. 7.11 are displayed values of the correction factors *vs* centrality (expressed via TPC multiplicity). The correction factors grow with centrality as a consequence of the fact that the elliptic flow, and hence the reaction plane resolution, decreases with centrality. The values of the correction factors were calculated in three different ways. In Fig. 7.11 with open (closed) circles are depicted the correction factor values calculated from the correlation of the reaction plane angles obtained from a random division, in $\phi$ space, of the event into two subevents in Run I (Run II). The difference between them is practically negligible. With stars are shown the correction factor values calculated from the correlation of reaction plane angles obtained from a division, in $\eta$ (pseudorapidity) space. In order to make a big difference in two ways of calculation (division in $\phi$ and division in $\eta$), the event was not divided randomly into two $\eta$ subevents but in two separate subevents which correspond to $2.05 \leq \eta \leq 2.375$ and $2.375 \leq \eta \leq 2.70$ region.

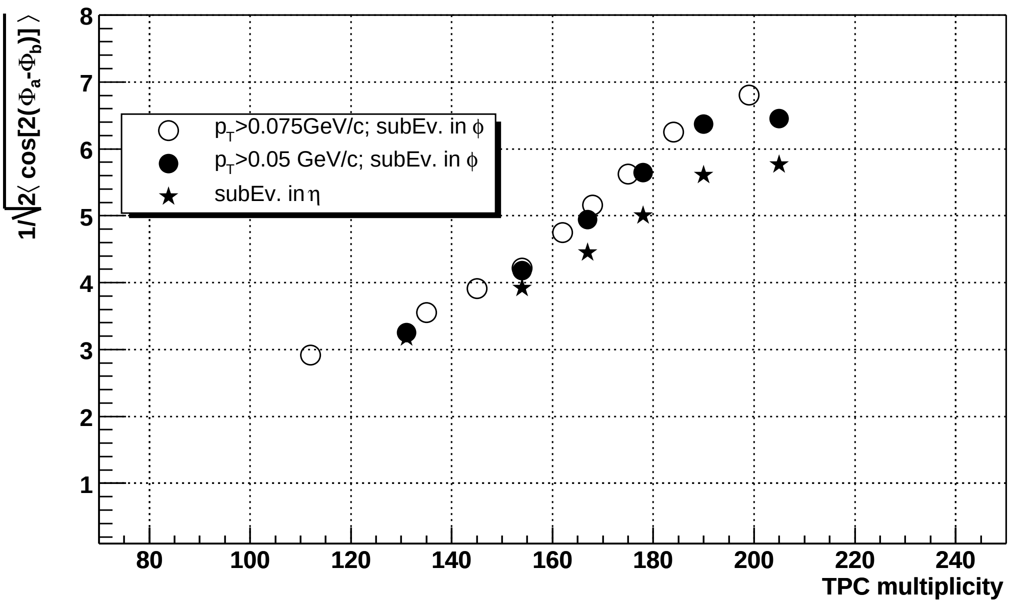

**Figure 7.11:** Correction factors, as the inverse values of the reaction plane resolutions calculated using the Eq. (3.13) are presented as a function of centrality.

The information which Fig. 7.11 contains is later used for an estimation of the systematic errors in the elliptic flow measurements which comes from a finite precision with which the reaction plane resolution can be calculated.

---

[6] In this case *event* means a set of particles which were used for the reaction plane reconstruction.

## 7.3 Elliptic Flow of $\Lambda$ Particles

In Fig. 7.12 are plotted the values of $v_2$ measured as a function of $\Lambda$ particle transverse momentum ($0.3 \leq p_T \leq 3.5$ GeV/c) integrated over all centralities. The $\Lambda$ elliptic flow shows a typical $p_T$ dependence characteristic for baryon elliptic flow. It has a small magnitude in the region of small $p_T$ and with increasing $p_T$, the $v_2$ values slowly increase. When it reaches high $p_T$ values, the baryon elliptic flow achieves big values.

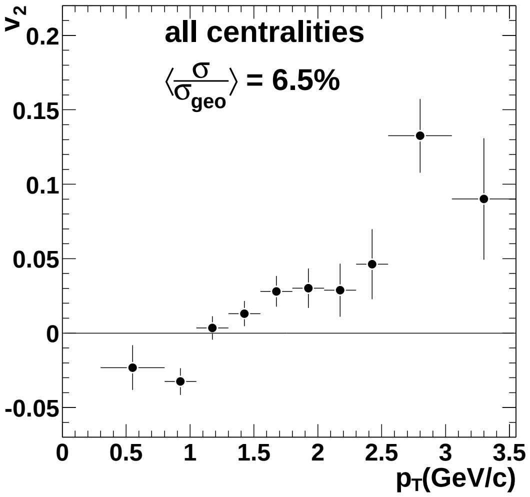

**Figure 7.12:** $\Lambda$ elliptic flow *vs* $p_T$ for all centralities taken together.

Such a behavior can be seen better in the case of semicentral collisions. In the left plot of Fig. 7.13 are shown the results of the $\Lambda$ elliptic flow *vs* the $p_T(\Lambda)$ in the semicentral collisions. The $v_2(\Lambda)$ grows with $p_T$ and reaches values larger than 10% for the highest $p_T$. On the right plot of Fig. 7.13 is shown $v_2(p_T)$ dependence for $\Lambda$ particles emitted in central collisions. There is a clear difference in the elliptic flow magnitude between semicentral and central collisions.

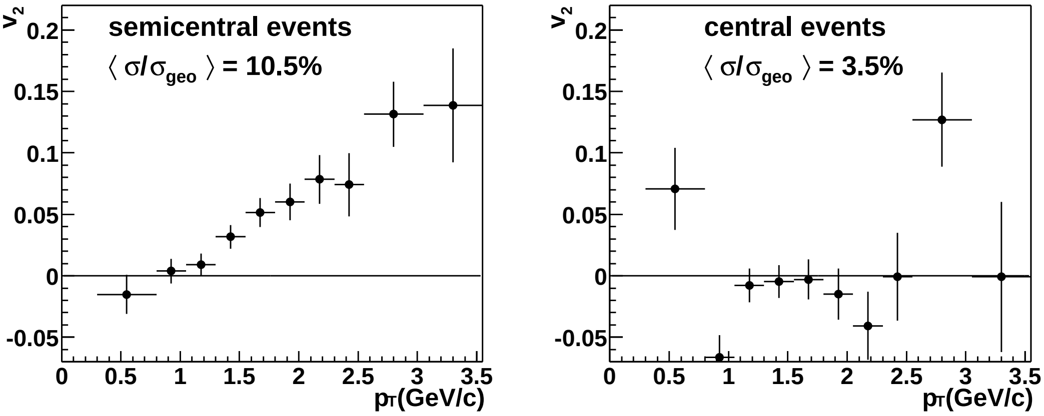

**Figure 7.13:** $\Lambda$ elliptic flow *vs* $p_T$ for the semicentral (left) and central (right) collisions.

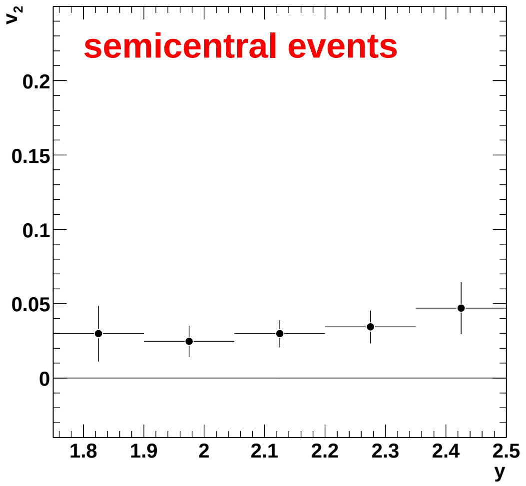

**Figure 7.14:** $\Lambda$ elliptic flow ıvs $y$ in the case of semicentral events.

As an example, in Fig. 7.14 is plotted the $\Lambda$ elliptic flow (integrated over all $p_T$ bins) versus $y$ in the case of semicentral collisions. As one can expect, this distribution should be flat [7]. But, the fact that $v_2(y)$ is not completely flat in rapidity could be explained by the $\Lambda$ acceptance. The mean transverse momentum of the $\Lambda$ increases with rapidity (as one can see from Fig. 7.7) and hence $v_2$ increases.

The analysis performed in this thesis, as was already mentioned, was done in 9(6) centrality bins in the case of Run I (Run II). Integrating $dN/d\phi$ distributions (like that one shown in Fig. 7.8 at the bottom) over whole $p_T$ and rapidity range in a given centrality bin gives the possibility to obtain $\Lambda$ elliptic flow *vs* centrality. Such distributions are shown in Fig. 7.15. The $\Lambda$ elliptic flow decreases with centrality.

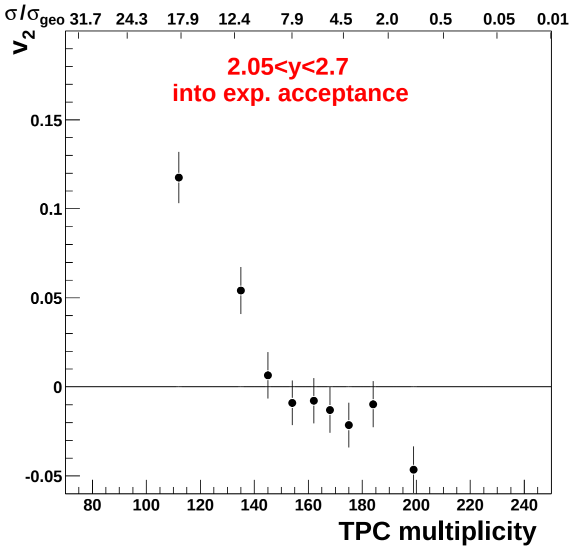

**Figure 7.15:** $\Lambda$ elliptic flow *vs* centrality.

As the $\Lambda$ elliptic flow analysis was performed in two different ways (Run I/II), the

---

[7] Due to the fact that the rapidity interval in which the analysis is done is rather narrow $\Delta y = 0.65$

differences between these two analysis could be used to estimate the systematic error of this study. In order to visualize the size of the systematic errors, in Fig. 7.16 are shown on the top of each other results of $v_2$ *vs* $p_T$ obtained in the two, above mentioned analyses. There is a very good agreement between them which means that the statistical errors dominate over the systematic ones. The overall absolute systematic error $\Delta v$ is estimated as the difference between $v_2$ values integrated over $p_T$, $y$ and centrality and its value is $^{+0.001}_{-0.009}$. One can notice that the systematic error is not independent of $p_T$. For small $p_T$ values ($p_T \leq 1.6$ GeV/c) the estimated absolute systematic error $\Delta v$ is $^{+0.001}_{-0.007}$, while in the case of high $p_T$ values ($p_T \geq 1.6$ GeV/c) the estimated absolute systematic error is $^{+0.00}_{-0.02}$.

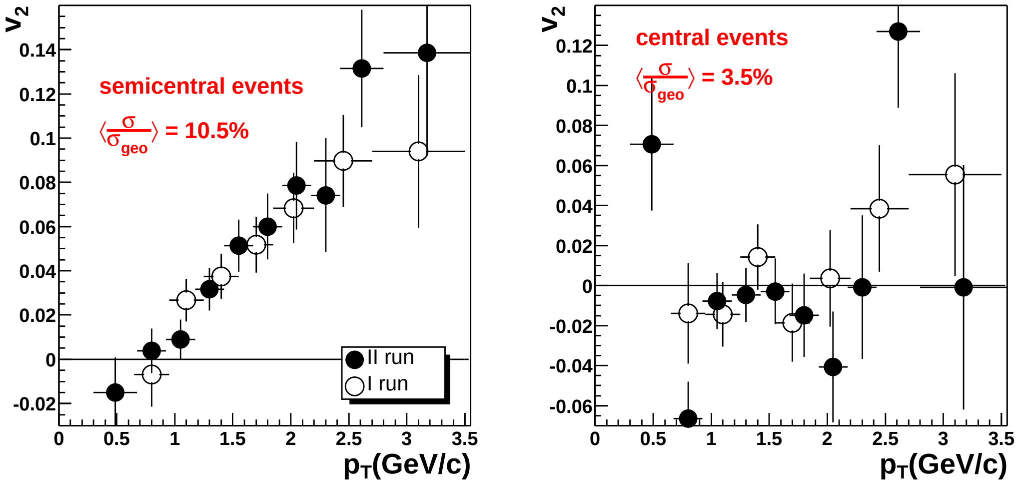

**Figure 7.16:** $\Lambda$ elliptic flow *vs* $p_T$ from Run I and Run II calculations.

# Chapter 8

# FLOW ANALYSIS OF $K_S^0$ PARTICLES

The second strange particle which its anisotropic flow has been investigated in this thesis is the $K_S^0$ meson. The study of the $K_S^0$ elliptic flow is important due to getting the systematics from different particle species. It is especially important for the comparison with $\pi^{\pm}$ and $\Lambda$ elliptic flow which can establish the mass ordering effect due to the fact that the mass of $K_S^0$ particle is bigger than the pion mass and smaller than the mass of $\Lambda$ particle. Having one particle specie more in the elliptic flow systematics can give better insight in the properties of different scaling scenarios. Chapter 9 is partially devoted to the mass ordering effect and the scaling properties.

This Chapter is organized in the following way. In Section 8.1, as a possible $K_S^0$ daughters, the $\pi^+$ and $\pi^-$ selection will be discussed as well as the method of $K_S^0$ reconstruction. The method of $K_S^0$ reconstruction is entirely different from the one used for the $\Lambda$ reconstruction. The reaction plane determination and the determination of its resolution are the contents of Section 8.2. In the last Section of this Chapter the obtained results will be presented.

## 8.1 Particle Selection and $K_S^0$ Reconstruction

The $K_S^0$ particles were reconstructed via the decay chanel $K_S^0 \rightarrow \pi^+ + \pi^-$ with $BR = 68.95\%$ and $c\tau = 2.6739$ cm [70]. The first step in the extraction of $K_S^0$ daughters was the selection of $\pi^+$ and $\pi^-$ particles as possible candidates of $K_S^0$ daughters. The selection was done in the same way as in Subsection 4.3.1 with one difference. In order to increase the $K_S^0$ statistics, in the momentum-$dE/dx$ distribution, instead of $\pm 1.5\sigma$ window around the nominal Bethe-Bloch value, particles within $\pm 2\sigma$ window around the nominal Bethe-Bloch value were chosen.

Impossibility to make a perfect particle identification via the TPC $dE/dx$ value results in a big combinatorial background. A powerful tool for the background suppression is provided by the secondary vertex reconstruction. The corresponding codes used for the secondary vertex reconstruction were developed by W. Ludolphs [6]. The method is able to separate tracks originating from the primary vertex from those originating from the secondary one. The detectors used for this purpose are the 2 SDD detectors and the TPC. The first step in the procedure is the fitting of a particle track with a straight line in the $\bar{B}$ field free region between the SDD detector system and the RICH2 mirror. The straight line fit is based on 3 points coming from the 2 SDD detectors and the TPC track extrapolated to the position of the RICH2 mirror. The deviations from the straight line can occur by multiple scattering what is accounted for by the momentum dependent errors of these 3 points. The second step of the procedure is that each two tracks, as possible candidates for the $K_S^0$ daughters, are combined and the point of the closest approach between them is calculated. Assuming that the $K_S^0$ particle comes from a primary vertex, a possibility to suppress fake track combinations is given by a cut on the radial distance between the momentum vector of the $K_S^0$ candidate and the primary vertex in the $x - y$ plane. This variable will be called *bep*. In the case of possibly true $K_S^0$ candidate the *bep* parameter has to be small in contrast to the case of the fake combination of tracks. The more details about the procedure for the secondary vertex reconstruction one can find in [6].

The following list of cuts was applied in order to suppress the combinatorial background

1. a $\chi^2$ probability value for a linear fit applied on 3 points has to be bigger than 0.01.
2. the *bep* parameter has to be smaller than 0.02 cm.
3. the opening angle $\theta_{\pi^+\pi^-} > 0.05$ rad.
4. the value of the z-coordinate of the secondary vertex has to be bigger than 1.0 cm.
5. In order to suppress the contamination of $\Lambda$ and $\bar{\Lambda}$ particles, an Armenteros-Podolanski cut with $q_T \geq 0.12$ GeV/c was applied (see Fig. 7.2).
6. a $\chi^2$ probability of finding the secondary vertex has to be bigger than 0.01.

The combinatorial background is reconstructed by using the mixed events technique. In order to preserve the topology of the event, only events with similar multiplicity and the orientation of the reaction plane were allowed to mix with each other. Similar multiplicity means that the difference in the multiplicity must not be bigger than 10%, while the similar reaction plane orientation means that the difference between the reaction plane orientations from the two events which are used in the mixed events analysis must not be bigger than $22^\circ$ what corresponds to the half of the reaction plane resolution. In order to make the combinatorial background smooth enough the events mixing procedure was repeated 10 times.

In Fig. 8.1 is shown the invariant mass distribution of the signal and the normalized combinatorial background (left) and the invariant mass distribution of the signal after subtraction of the normalized combinatorial background (right). A huge part of the background is suppressed if one recalculates the momenta of possible daughter particles with respect to the reconstructed secondary vertex and make cuts on the position of the vertex.

Similarly as in the case of the $\Lambda$ elliptic flow analysis, the $K_S^0$ elliptic flow analysis was done differentially in small enough $y - p_T$ bins. The characteristics (the mean value and the width) of the signal after subtraction of the normalized combinatorial background

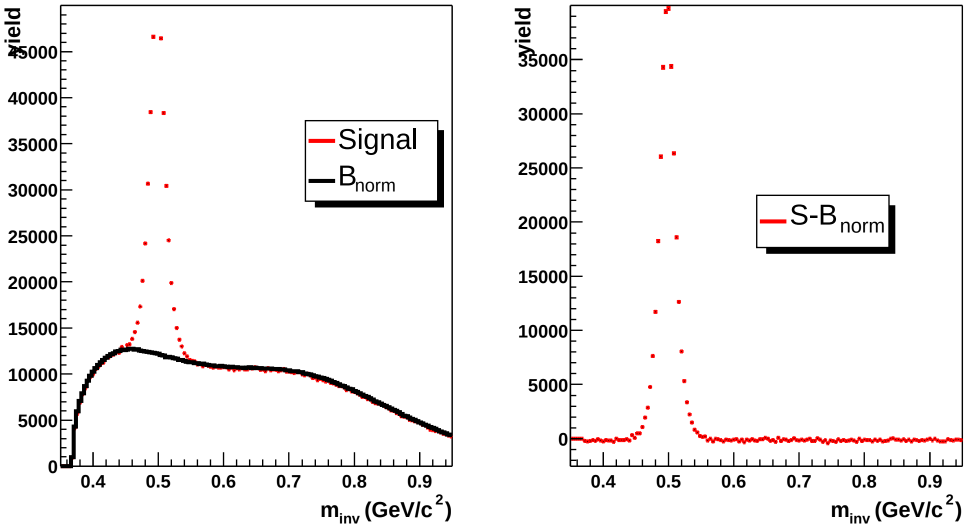

**Figure 8.1:** Left: The invariant mass distribution of the signal (red line) and the normalized combinatorial background (black line). Right: The invariant mass distribution of the signal after subtraction of the normalized combinatorial background.

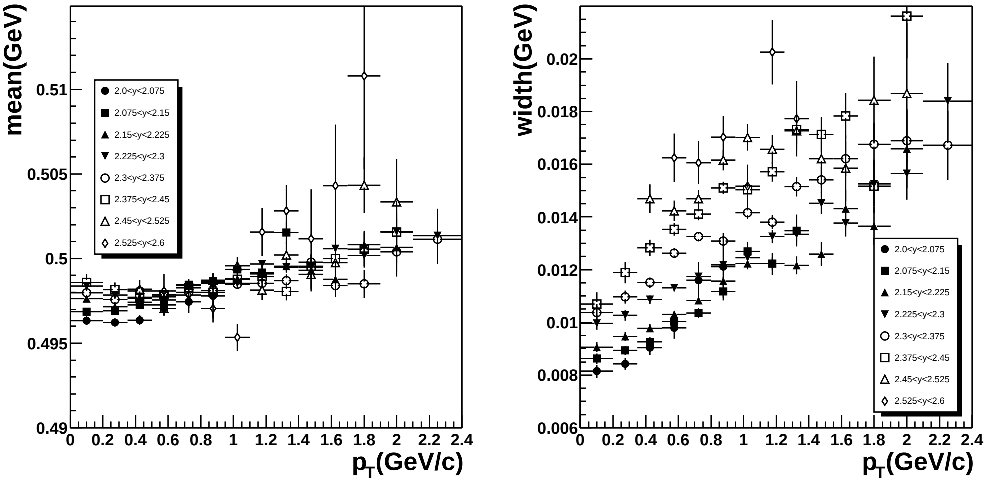

**Figure 8.2:** Left: mass of $K_S^0$ as function of $p_T$ for different rapidities displayed with different symbols. Right: the same dependence in the case of the width of $K_S^0$.

*vs* $y$ and $p_T$ are shown in Fig. 8.2. The signal distributions were fitted with *a Gaussian + a constant*. The mass of $K_S^0$ which is obtained as the mean value of the Gaussian fit has a weak dependence on $y$ and $p_T$, while in the case of the width both dependences are strong. Once the mass and the width of $K_S^0$ were determined for a given $y$ and $p_T$ bin they were kept as constants for the rest of the analysis. In the approach for the $K_S^0$ reconstruction described above the values of $S/B \approx 0.92$ and $S/\sqrt{B} \approx 500$ were obtained.

Fig. 8.3 shows the $y - p_T$ distribution of the accepted $K_S^0$ particles after all applied cuts. The $K_S^0$ particles used for the elliptic flow analysis are from the kinematic region

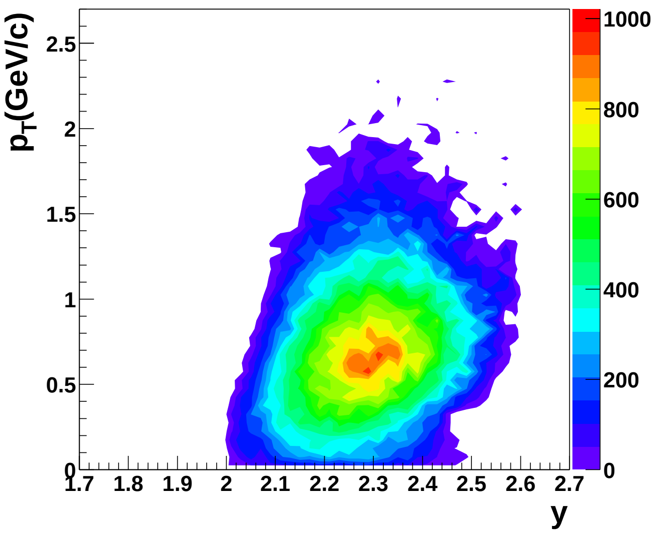

**Figure 8.3:** Distribution of accepted $K_S^0$ in $y - p_T$ space.

$2.0 < y < 2.6$ and $0 < p_T < 2.4$ GeV/c. This kinematic region does not cover all $y - p_T$ bins where $K_S^0$ particles were reconstructed. The $y - p_T$ bins where the $K_S^0$ statistics (the edges of the acceptance) were not included in the elliptic flow analysis.

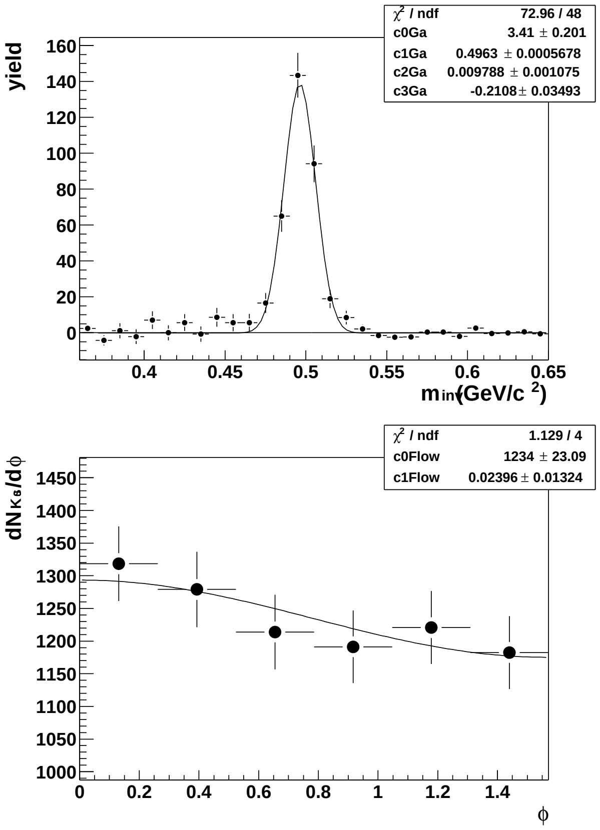

**Figure 8.4:** Top: $K_S^0$ reconstructed for $1.62 \leq y \leq 1.69$, $0.675 \leq p_T \leq 0.8$ GeV/c and $15° \leq \phi \leq 30°$. Bottom: Elliptic flow pattern reconstructed from the $\Lambda$ yield in $\phi$ bins for $p_T \approx 2.1$ GeV/c.

In order to measure the yield of $K_S^0$ particles in a given $y - p_T - \phi$ bin, the area under the peak in the invariant mass distribution, which is obtained from the Gaussian fit, was used. Fig. 8.4 (top) shows an example of such a distribution. Plotting the yield *vs* $\phi$ for different $y$ and $p_T$ values one can construct $dN_{K_S^0}/d\phi$ distributions. One example of such a distribution is shown at the bottom of the Fig. 8.4.

The observed elliptic flow values $v_2'$ are obtained by fitting $dN_{K_S^0}/d\phi$ distribution with a cosine function $c[1+2v_2'\cos(2\phi)]$. After the correction for the reaction plane resolution one gets the information about the differential elliptic flow magnitude.

## 8.2 Reaction Plane Determination and its Resolution

Again, as in Section 7.2, assuming that the only significant anisotropic flow is the elliptic flow, one can decompose the azimuthal distributions of $K_S^0$ particles constructed with respect to the reaction plane in a Fourier decomposition given by Eq. (7.1). The orientation of the reaction plane is derived from the second Fourier harmonic using Eq. (7.2). In order to avoid of the autocorrelation effect, tracks used for the $K_S^0$ reconstruction are excluded from the set of tracks used to calculate the reaction plane. Again, as in the case of $\pi^\pm$ and $\Lambda$ elliptic flow analysis, the flattening of the reaction plane was done by recentering and the Fourier expansion of the raw $dN/d\Phi$ distribution. After the flattening procedures were applied the flat $dN/d\Phi$ distributions were obtained and they are essentially the same to the one shown in Fig. 7.9 (right).

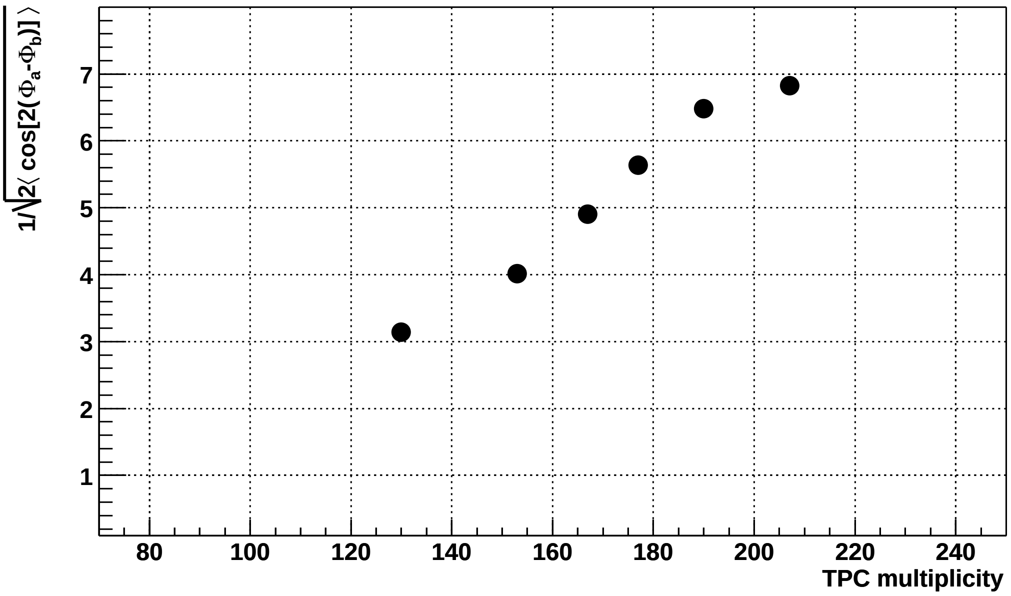

**Figure 8.5:** Correction factors in the $K_S^0$ elliptic flow analysis using the Eq. (3.13) are shown as a function of centrality.

The determination of the resolution of the measured reaction plane was done using the two random subevents method which is already described in Section 7.2. The correction factors for the reaction plane resolution *vs* centrality are shown in Fig. 8.5. Again, they are growing with the centrality because the magnitude of the elliptic flow and hence the reaction plane resolution decreases with the centrality.

## 8.3 Elliptic Flow of $K_S^0$ Particles

Fig 7.12 shows the $K_S^0$ elliptic flow *vs* $K_S^0$ transverse momentum for all centralities taken together. As in average the elliptic flow analysis was performed for rather central collisions (see Fig. 4.17) where the $v_2$ is expected to be small, and as the $K_S^0$ statistics is rather poor has as a consequence huge statistical errors in the presented distribution. Still, there is an indication that $v_2(p_T)$ grows with transverse momentum of the $K_S^0$.

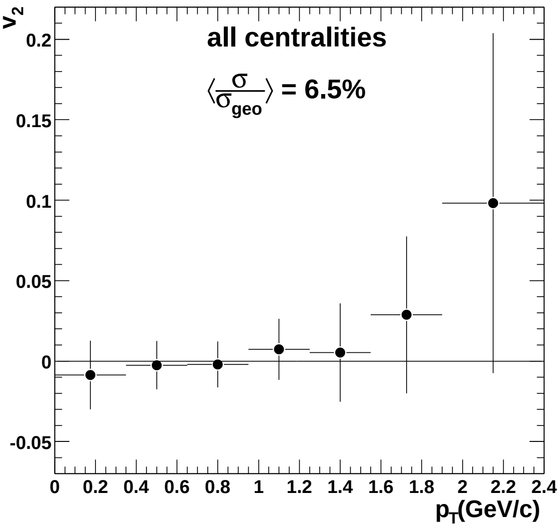

**Figure 8.6:** $K_S^0$ elliptic flow *vs* $p_T$ for all centralities taken together.

In order to see the elliptic flow signal, in the left plot of Fig 8.7 are shown $v_2(p_T)$ dependences for the $K_S^0$ particles emitted in the semicentral collisions. In the right plot of

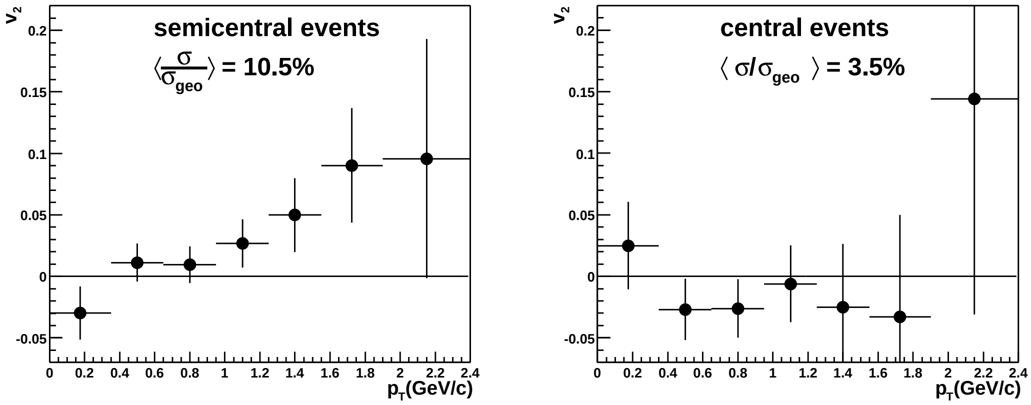

**Figure 8.7:** $K_S^0$ elliptic flow *vs* $p_T$ for the semicentral (left) and central (right) collisions.

the same Figure is shown the corresponding dependence for the central collisions. In the case of semicentral collisions, $K_S^0$ elliptic flow grows with $p_T$ and reaches roughly 10% at the highest $p_T$. There is a difference in the $K_S^0$ elliptic flow magnitude between these two classes of events.

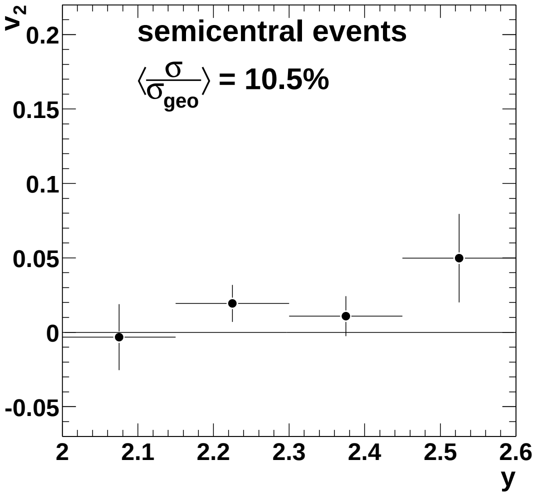

**Figure 8.8:** $K_S^0$ elliptic flow *vs* $y$ in the case of semicentral events.

As an example, in Fig. 8.8 is plotted $K_S^0$ elliptic flow integrated over all $p_T$ bins as a function of $y$ in the case of semicentral collisions. Similarly as in the case of the $\Lambda$ elliptic flow analysis $v_2$ grows with $y$ due to the fact that the mean transverse momentum of $K_S^0$ increases with rapidity (as one can see from Fig. 8.3). It seems that the effect is not so strong as in the case of the $\Lambda$ elliptic flow analysis. Also, small $K_S^0$ statistics does not allow to make a strong conclusion about $v_2(y)$ dependence.

# Chapter 9

# COMPARISONS AND SCALINGS

The elliptic flow of mesons ($\pi^{\pm}$ and $K_S^0$) and baryons (protons and $\Lambda$) will be mutually compared. Also, the obtained results will be compared with the hydrodynamical calculations and to other SPS and RHIC results. At the end of this Chapter the results scaled to the number of constituent quarks $n_q$ and to the flavor transverse rapidity $y_T^{fs}$ will be presented.

## 9.1 Comparison with Hydrodynamical Model

A system can be described within a hydrodynamical theory if the time scales of the microscopic processes within the system are significantly smaller than the time scale of the macroscopic evolution of the system. In the heavy-ion collisions it means that the averaged time between two successive interactions between partons is much smaller than the life time of the system. Only under that condition partons can interact enough times in order to equilibrate the system. Then the hydrodynamical formalism can be applied in order to describe the system.

The covariant equation for the energy-momentum conservation is given by

$$\partial_\mu T^{\mu\nu} = 0 \tag{9.1}$$

where the energy-momentum tensor is defined as

$$T^{\mu\nu} = (\epsilon + p)u^\mu u^\nu - p g^{\mu\nu} \tag{9.2}$$

where $\epsilon$, $p$ and $u^{nu}$ are the energy density, pressure and four-velocity respectively.

The hydrodynamical equations are valid from the early time of the collision when the system became thermalized until the time when the interactions between partons become so weak that they cannot maintain the equilibration reached in the previous stage of the collision. When the initial conditions for a given type of heavy-ion collision is provided one needs to specify the EoS which relates thermodynamical quantities of the system.

Basically, the elliptic flow is a consequence of the rescattering of the particles produced in a heavy-ion collision. For a given initial size of the overlapping region between the colliding nuclei, the hydrodynamical description gives the highest flow magnitude due to the most intense rescattering incorporated into the hydrodynamical formalism.

In this thesis the obtained results on the elliptic flow are compared with the hydrodynamical calculations done by P. Huovinen based on [95, 96]. The calculation was done in 2+1 dimensions assuming a boost-invariant longitudinal flow. The initial conditions were fixed via a fit to the $p_T$ spectra of negatively charged particles and protons in Pb+Pb collisions at the top SPS energy [97]. The used EoS assumed the 1-st order phase transition to a QGP at a critical temperature of $T_c = 165$ MeV. The hydrodynamical predictions were calculated with 2 freeze-out temperatures, $T_f = 120$ MeV and $T_f = 160$ MeV.

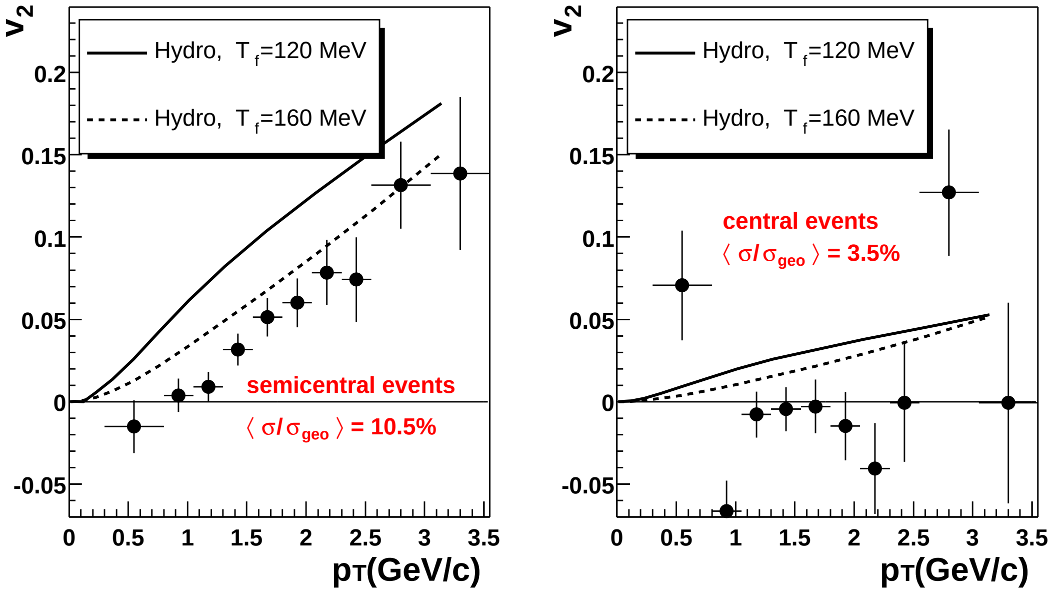

**Figure 9.1:** Comparison between the hydrodynamical calculation and the CERES experimental results on $\Lambda$ elliptic flow in semicentral (left) and central (right) events.

In Fig. 9.1 is shown a comparison between $v_2(p_T)$ for $\Lambda$ hyperons emitted in semicentral (left plot) and central (right plot) collisions and the hydrodynamical calculations described above. The model prediction with a lower freeze-out temperature of $T_f = 120$ MeV overpredicts the data at any $p_T$ value. A better agreement between the theory and the data can be achieved with a higher freeze-out temperature of $T_f = 160$ MeV. The same behavior is observed comparing the pion flow from CERES to the same hydrodynamical model [98].

The higher freeze-out temperature may as well be consistent with the freeze-out parameters extracted from the inclusive transverse mass distributions [99]. Similar results can be obtained by combining the hydrodynamical model with $T_f = 120$ MeV together with a transport model [100] or by a hydrodynamical model which including viscosity [101].

## 9.2 Comparison with STAR and NA49 experiment

A comparison of the CERES data with the results from the NA49 [102, 103] at the same energy ($\sqrt{s_{NN}} = 17$ GeV) and with the STAR results [104] at $\sqrt{s_{NN}} = 200$ GeV are shown in Fig. 9.2. The NA49 and CERES results are in a very good agreement.

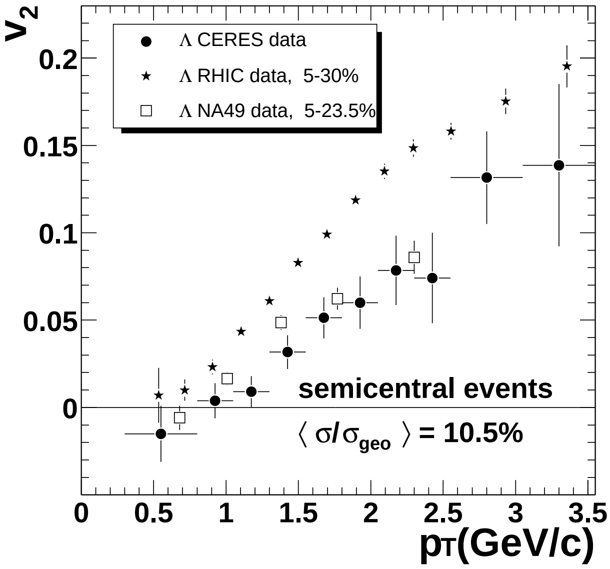

**Figure 9.2:** Comparison of $\Lambda$ elliptic flow measured by CERES, STAR and NA49.

The $v_2$ values measured at the RHIC energy are $30 - 50\%$ higher. Partly, this is due to an effectively higher centrality (i.e. smaller $\sigma/\sigma_{geo}$) in CERES as compared with the STAR experiment. From the other side it is expected that the $v_2$ values measured at the RHIC energy are higher than those at the SPS energy due to the energy dependence of the $v_2$. If one rescales STAR data to the centrality range close to CERES data ($5\% \leq$

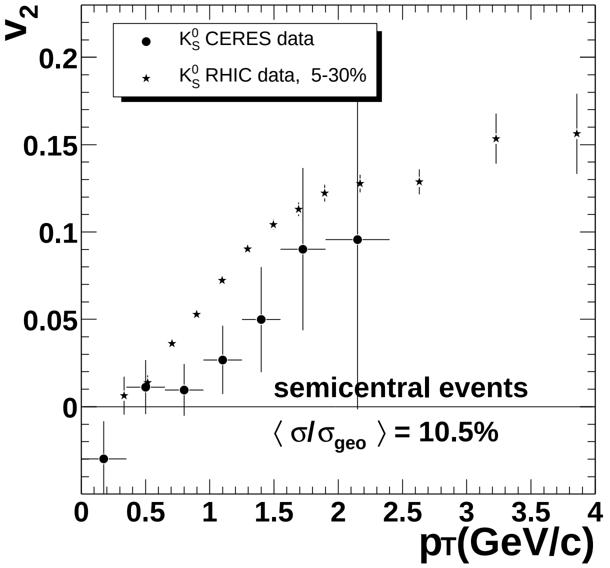

**Figure 9.3:** Comparison of $K^0_S$ elliptic flow measured by CERES and STAR.

$\sigma/\sigma_{geo} \leq 17\%$) they become for $\approx 25\%$ smaller with respect to one plotted in Fig. 9.2, but still they are higher than those measured by CERES and NA49 at the SPS energy.

Fig. 9.3 shows a comparison of the $K_S^0$ elliptic flow measured by CERES and STAR experiment. Similarly as in the case of the $v_2(\Lambda)$, the $v_2(K_S^0)$ measured at the RHIC energy is higher than the one measured at the top SPS energy. This is a consequence of the energy dependence of $v_2$ as well as of the fact the CERES experiment has a higher centrality as compared to the STAR.

## 9.3 Mass Ordering Effect

Fig. 9.4 shows the elliptic flow magnitude of the $\pi^{\pm}$, low momentum protons, $\Lambda$, and $K_S^0$ emitted in semicentral events. For $\Lambda$ hyperons as well as for $\pi^{\pm}$ and $K_S^0$ mesons, $v_2$ increases monotonically with $p_T$.

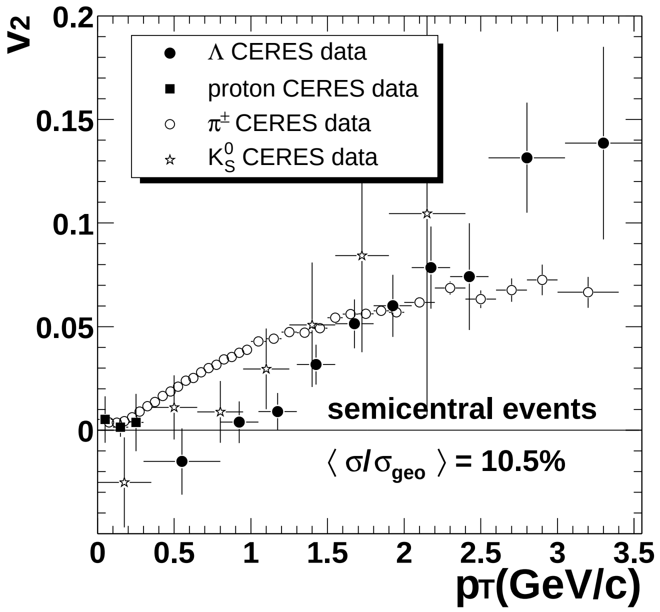

**Figure 9.4:** Comparison between the elliptic flow magnitude of the $\pi^{\pm}$, low momentum protons, $\Lambda$, and $K_S^0$ emitted in semicentral events.

At small $p_T$, up to $\approx 1$ GeV/c, heavier particle species have a smaller elliptic flow magnitude with respect to the lighter ones. In the region of high $p_T$, above $\approx 2$ GeV/c it is the opposite. A rather clear mass ordering effect is observed. It is not possible to give a clear statement about $v_2(K_S^0)$ at high $p_T$ due to poor statistics.

**Table 9.1:** The mass ordering effect between $v_2$ of $\Lambda$, $K_S^0$, and $\pi^{\pm}$ at the top SPS energy.

| small $p_T$ | high $p_T$ |
|---|---|
| $v_2(\Lambda) < v_2(K_S^0) < v_2(\pi^{\pm})$ | $v_2(\pi^{\pm}) < v_2(\Lambda)$ |

As proton and $\Lambda$ hyperon have similar masses, the $v_2$ of low momentum identified protons was used as a natural continuation of $\Lambda$ $v_2(p_T)$ dependence at region of small $p_T$.

## 9.4 Scaling to the Number of Constituent Quarks

Comparing the intensities of the meson and baryon elliptic flow gives the possibility to get some knowledge about the mechanisms responsible for the hadronization of the dense matter created in the heavy-ion collisions. Due to that two scaling scenarios were proposed. In the first one, scaling to the number of the constituent quarks ($n_q$) [105–107], one needs to scale both, $v_2$ and $p_T$.

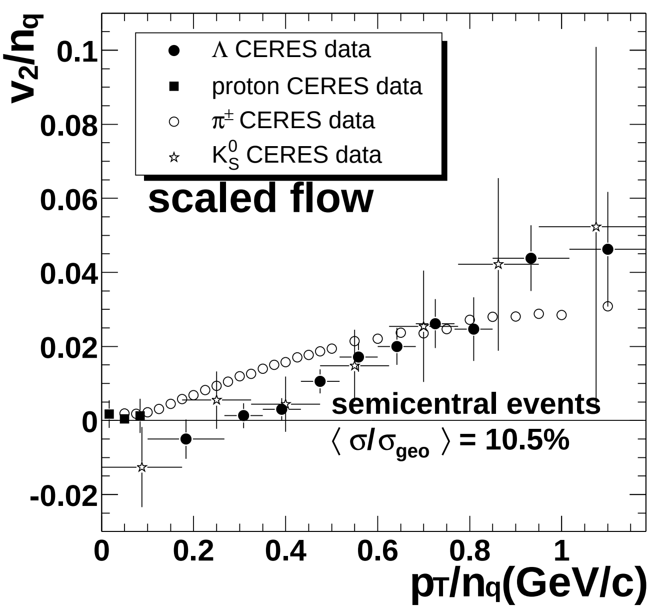

**Figure 9.5:** Comparison between elliptic flow magnitude scaled to the number of the constituent quarks for the $\pi^{\pm}$, low momentum protons, $\Lambda$, and $K^0_S$ emitted in semicentral events.

Fig. 9.5 shows the scaled elliptic flow magnitude $v_2/n_q$ for $\pi^{\pm}$, $\Lambda$, and $K^0_S$ against $p_T/n_q$. The results are obtained from the semicentral class of events. While the $v_2$ is significantly different for all three kinds of particles at any $p_T$, except at the intersecting region around $\approx 1.5$ GeV/c, within errors $v_2/n_q$ *vs* $p_T/n_q$ is the same in the case of $\Lambda$, and $K^0_S$ particles. There is an indication that high $p_T$ pions ($p_T > 1.1$ GeV/c) shows scaling behavior. A similar behavior is observed by the STAR experiment at RHIC [104].

Such a scenario is consistent with the coalescence mechanism where co-moving quarks with high $p_T$ forming hadrons. In this case scaling to the number of the constituent quarks shows the original momentum space azimuthal anisotropy formed at the early stage of the collision. This scenario also argue for the existence of a strongly interacting parton system formed at the early stage of the heavy-ion collision. The deviation from the scaling behavior in the case of the low momentum $\pi^{\pm}$ may reflect the break-down of the coalescence mechanism at low $p_T$. This deviation may be also caused by the contribution of pions from resonance decays [108, 109]. Alternatively, it may reflect the difficulty of a constituent quark coalescence model to describe the production of pions whose masses are significantly smaller than the assuemed constituent quark masses [105].

## 9.5 Scaling to the Flavor Transverse Rapidity $y_T^{fs}$

An important scaling prediction of the hydrodynamical theory is the so called flavor transverse rapidity $y_T^{fs}$ scaling [110–112]. In this scaling scenario, $v_2$ of different particle species should scale with $y_T^{fs} = k_m y_T^2 m$. Here $m$ is the mass of particle, $y_T$ is the transverse rapidity defined as $y_T = \sinh^{-1}(p_T/m)$ and $k_m$ is a mass dependent factor with a value approximately equal to 1. In Table 9.2 are given the $k_m$ values for $\pi^{\pm}$, $K_S^0$ and $\Lambda$ particle.

**Table 9.2:** The $k_m$ values for $\pi^{\pm}$, $K_S^0$ and $\Lambda$ particle.

| | $\pi^{\pm}$ | $K_S^0$ | $\Lambda$ |
|---|---|---|---|
| $k_m$ | 1.2965 | 1.0415 | 0.9980 |

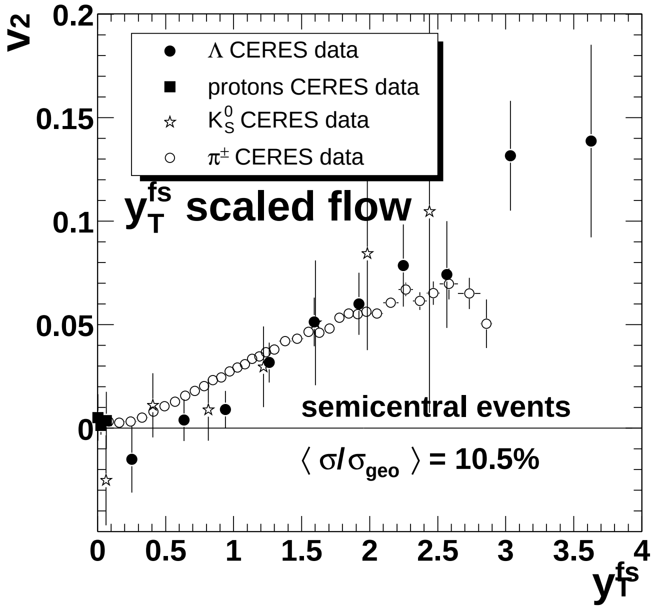

**Figure 9.6:** Comparison between elliptic flow magnitude scaled to the transverse rapidity $y_T^{fs}$ for the $\pi^{\pm}$, $\Lambda$, protons and $K_S^0$ emitted in semicentral events.

Fig. 9.6 shows the values of $v_2$ for $\pi^{\pm}$, $\Lambda$, protons and $K_S^0$ emitted in semicentral events scaled to the $y_T^{fs}$ variable. Within statistical errors a rather good scaling is observed for all particles. This can indicate a hydrodynamic behavior of matter created in heavy-ion collisions at the highest SPS energy.

# Chapter 10

# CONCLUSIONS

In this thesis the elliptic transverse flow of particles measured by the CERES experiment was investigated and discussed. A detailed investigation has been done for charged ($\pi^{\pm}$ and proton) and strange ($\Lambda$ and $K_S^0$) particles emitted in rather central Pb+Au collisions at the highest SPS energy. The data, collected by the CERES experiment which covers $\eta = 2.05 - 2.70$ with full $2\pi$ azimuthal acceptance and $p_T$ sensitivity up to 4 GeV/c, are very suitable for the elliptic flow investigations.

The huge statistics ($\approx 5 \cdot 10^9$) of detected pions allowed very precise measurements of their elliptic flow. After subtraction of the HBT correlation effect, the obtained $v_2(p_T)$ dependence achieved a proper shape. The $v_2$ grows quadratically with $p_T$ at low $p_T$ region. At the intermediate region it has a linear $p_T$ dependence and it saturates at the high $p_T$ region. The integrated pion elliptic flow smoothly decreases with the centrality. Only protons with very low momenta (below 1.2 GeV/c) could be identified unambiguously via the energy loss and the elliptic flow of these protons was reconstructed in order to have a continuation of the $\Lambda$ elliptic flow at the low-$p_T$ region due to the similar masses of protons and the $\Lambda$ hyperons.

The elliptic flow of $\Lambda$ particles emitted in the semicentral collisions shows a typical behavior. The $v_2$ value is close to zero up to $p_T = 1$ GeV/c and then it quickly rises up to more than 10% at the highest $p_T$. The integrated $\Lambda$ elliptic flow decreases with the centrality. The $v_2$ of the $K_S^0$ particles grows with $p_T$ in the semicentral collisions.

The elliptic flow of mesons ($\pi^{\pm}$ and $K_S^0$) and baryons (protons and $\Lambda$) has been compared. A mass ordering effect is observed. At small $p_T$, up to $\approx 1$ GeV/c, heavier particle species have a smaller elliptic flow magnitude with respect to the lighter ones. In the region of high $p_T$, above $\approx 2$ GeV/c it is opposite. Due to the poor $K_S^0$ statistics it is not possible to give a clear statement about $v_2(K_S^0)$ at high $p_T$.

In order to test the hydrodynamical models and the sensitivity to the EoS the measured $\Lambda$ elliptic flow was used. The hydrodynamical calculation was done in 2+1 dimensions assuming a boost-invariant longitudinal flow and the EoS with a 1-st order phase transition to QGP at a critical temperature of $T_c = 165$ MeV. The model prediction with a lower freeze-out temperature of $T_f = 120$ MeV overpredicts the data, while a better agreement between the theory and the data is achieved with a higher freeze-out temperature of $T_f = 160$ MeV. The same behaviour is observed comparing the pion flow from CERES to the same hydrodynamical model [98].

The measured $\Lambda$ elliptic flow was compared with $v_2$ values observed with the STAR experiment at RHIC and with the NA49 results. A very good agreement between two independent measurements of the $\Lambda$ elliptic flow at the top SPS energy was found. The $v_2$ values measured at the RHIC energy are higher than those at the SPS. Partly, this is due to an effectively higher centrality in the CERES experiment as compared with the STAR experiment. From the other side it is expected that $v_2$ values measured at the RHIC energy are higher than those at the SPS energy due to the energy dependence of the $v_2$.

The most interesting part of the results concern the scaling properties of the elliptic flow of different particle kinds. In order to get better insight into the origin of the collective flow a scaling to the number of the constituent quarks and the transverse rapidity $y_T^{fs}$ scaling predicted by hydrodynamics was performed. Within the errors the elliptic flow of $\Lambda$ and $K_S^0$ particles scales well. At small $p_T$, pions do not scale, but it seems that at high $p_T$ the elliptic flow of pions is scaled to the number of the constituent quarks. Concerning the other scaling scenario, so called $y_T^{fs}$ scaling shows that within the statistical errors all three particle kinds are scaled reasonably well. Here arise questions. If particles obeyed the $y_T^{fs}$ scaling, does the thermalization occurs at the top SPS energy? Even more, is the QGP formed already at this energy?

# Appendix A

# VARIABLES

## A.1 Rapidity and Pseudorapidity

A particle is characterized with the mass $m$ and the momentum $\mathbf{p} = \mathbf{p}_{||} + \mathbf{p}_T$ which could be decomposed into a longitudinal and transversal component with respect to the direction of its movement. Someone can try to find another inertial system in which $\mathbf{p}_{||} = 0$, i.e. $\mathbf{p}' = \mathbf{p}_T$. The velocity of that system (denoted with a ') is connected with rapidity. In order to find that connection one can write transformation formulae for energy and momentum as

$$E' = \gamma(E - \mathbf{V} \cdot \mathbf{p}) = \gamma(E - Vp_{||}) \tag{A.1}$$

$$\mathbf{p}'_{||} = \gamma(\mathbf{p}_{||} - \mathbf{V}E) \tag{A.2}$$

$$\mathbf{p}'_T = \mathbf{p}_T \tag{A.3}$$

As the system of the interest is a system in which $\mathbf{p}'_{||} = 0$, then $\mathbf{V} = \mathbf{p}_{||}/E$ with $-1 < \mathbf{V} < 1$ [1]. As the function $\tanh$ satisfies the inequality $-1 < \tanh y < 1$ one can write

$$V = \tanh y = \mathbf{p}_{||}/E \Rightarrow y = atanhV = atanh(p_{||}/E) \tag{A.4}$$

what is a definition of rapidity for a particular particle. From the following mathematical identities

$$atanhV = \frac{1}{2}\ln\frac{1+V}{1-V} = \frac{1}{2}\ln\frac{1+p_{||}/E}{1-p_{||}/E} \tag{A.5}$$

$$\frac{1}{2}\ln\frac{E+p_{||}}{E-p_{||}} = \frac{1}{2}\ln\frac{E+p_{||}}{E-p_{||}}\frac{E+p_{||}}{E+p_{||}} \tag{A.6}$$

$$\frac{1}{2}\ln(\frac{E+p_{||}}{m_T})^2 = \ln\frac{E+p_{||}}{m_T} \tag{A.7}$$

---

[1] Note that in the natural system of units $c$ is equal to 1

one obtains the geometrical definition of rapidity.

In the ultra-relativistic case ($p_T^2 \gg m^2$) the rapidity could be written as

$$y \approx -\ln \frac{p_T}{p + p_{||}} = -\ln(\tan \frac{\theta}{2}) \tag{A.8}$$

and with that one obtains the expression for the pseudorapidity.

# Appendix B

# FINITE GRANULARITY IN $dN_{\Lambda(K_S^0)}/d\phi$

## B.1 Correction for the Finite Granularity in $dN_{\Lambda(K_S^0)}/d\phi$ distributions

In order to increase the statistics of $\Lambda$ and $K_S^0$ particles in $dN_{\Lambda(K_S^0)}/d\phi$ distributions, these distributions are made in only 6 $\phi$ bins spanned from $0^\circ$ to $90^\circ$ measured with respect to the reaction plane. The problem of the finite granularity could appear in this case due to the fact that the center of the bin does not correspond to the gravity center due to the non-zero elliptic flow value. If that correction is large enough, the results have to be corrected.

As a positive elliptic flow of $\Lambda$ and $K_S^0$ particles was observed (see for example Fig. 7.8 bottom) one can call the left side of the $\phi$ bin as $\phi_{high}$ and the right side as $\phi_{low}$. Theoretically, in the case of $n$-th harmonic, one can write the following relations

$$N \propto \int_{\phi_{low}}^{\phi_{high}} (1 + 2v_n \cos[n(\phi - \Psi)])d\phi \qquad \text{(B.1)}$$

$$= \phi_{high} - \phi_{low} + \frac{2v_n}{n}\{\sin[n(\phi_{high} - \Psi)] - \sin[n(\phi_{low} - \Psi)]\} \qquad \text{(B.2)}$$

$$= \phi_{high} - \phi_{low} + \frac{2v_n}{n} 2\sin[\frac{n(\phi_{high} - \phi_{low})}{2}]\cos[\frac{n(\phi_{high} + \phi_{low}) - 2n\Psi}{2}] \qquad \text{(B.3)}$$

From the other side, one has the measured $\tilde{v}_n$ which is not corrected for the granularity effect. The value of $\tilde{v}_n$ can be expressed with

$$N \propto (1 + 2\tilde{v}_n \cos[n(\frac{\phi_{high} + \phi_{low}}{2} - \Psi)](\phi_{high} - \phi_{low}) \qquad \text{(B.4)}$$

Correlating Eq. (B.1) and Eq. (B.4), one gets[1]

---

[1] Note that in the case of small $\Delta\phi$, the measured value $\tilde{v}_n$ goes into its limit value $v_n$.

$$\frac{2v_n}{n}\sin[\frac{n(\phi_{high}-\phi_{low})}{2}] = \tilde{v}_n(\phi_{high}-\phi_{low}) \Rightarrow v_n = \frac{\frac{n}{2}\Delta\phi}{\sin(\frac{n}{2}\Delta\phi)}\tilde{v}_n \tag{B.5}$$

where $\Delta\phi = \phi_{high} - \phi_{low}$.

In the case of the elliptic flow ($n = 2$) the final equation becomes simplier:

$$v_n = \frac{\Delta\phi}{\sin(\Delta\phi)}\tilde{v}_n \tag{B.6}$$

In the case of $\Lambda$ elliptic flow, according to the Eq. (B.6) and the fact that bin size in the analysis was $\Delta\phi = 90°/6 = 15° = 0.2618$ rad it is easy to see that the correction factor $\Delta\phi/\sin(\Delta\phi)$ is equal to 1.0115152 what is negligible in this case.

# Bibliography

[1] Z. Fodor and S. D. Katz, JHEP **0404**, 050 (2004).

[2] P. Braun-Munzinger and J. Stachel, Nucl. Phys. **A606**, 320 (1996), nucl-th/9606017.

[3] P. F. Kolb, J. Sollfrank, U. W. Heinz, and H. Heiselberg, Phys. Rev. **C62**, 054909 (2000).

[4] CERES, D. Adamova *et al.*, Nucl. Phys. **A698**, 253 (2002).

[5] CERES, S. Yurevich, *Doctoral thesis* (University of Heidelberg, Germany, 2006).

[6] CERES, W. Ludolphs, *Doctoral thesis* (University of Heidelberg, Germany, 2006).

[7] F. Karsch, Nucl. Phys. **A698**, 199c (2002).

[8] K. A. Olive, Science **251**, 1194 (1991).

[9] E. Kolb and M. Turner, *The Early Universe* (Addison-Wesley, Redwood City, 1990).

[10] J. R. Ellis, J. I. Kapusta, and K. A. Olive, Phys. Lett. **B273**, 123 (1991).

[11] J. R. Ellis, J. I. Kapusta, and K. A. Olive, Nucl. Phys. **B348**, 345 (1991).

[12] N. K. Glendenning, Phys. Rev. Lett. **63**, 2629 (1989).

[13] C. Wong, *Introduction to High-Energy Heavy-Ion Collisions* (World Scientific, Singapure, 1994).

[14] CERES, G. Agakichiev *et al.*, Phys. Rev. Lett. **75**, 1272 (1995).

[15] CERES, J. P. Wurm, Nucl. Phys. **A590**, 103c (1995).

[16] CERES and TAPS, G. Agakichiev *et al.*, Eur. Phys. J. **C4**, 231 (1998).

[17] J.-Y. Ollitrault, Phys. Rev. **D46**, 229 (1992).

[18] D. H. Rischke, Prog. Part. Nucl. Phys. **52**, 197 (2004).

[19] F. Karsch and E. Lärmann, (*Quark-Gluon Plasma 3*, ed R.C. Hwa and X-N Wang, World Scientific, Singapure, 2004).

[20] O. Kaczmarek, F. Karsch, E. Lärmann, and M. Lutgemeier, Phys. Rev. **D62**, 034021 (2000).

[21] T. Matsui and H. Satz, Phys. Lett. **B178**, 416 (1986).

[22] F. Karsch, M. T. Mehr, and H. Satz, Z. Phys. **C37**, 617 (1988).

[23] F. Karsch, Lecture Notes in Physics **583**, 209 (2002).

[24] E. Lärmann and O. Philipsen, Ann. Rev. Nucl. Part. Sci. **53**, 163 (2003).

[25] J. D. Bjorken, Phys. Rev. **D27**, 140 (1983).

[26] H. Satz, Nucl. Phys. **A715**, 3 (2003).

[27] J. Stachel, Nucl. Phys. **A654**, 119c (1999), nucl-th/9903007.

[28] P. Braun-Munzinger, Nucl. Phys. **A663**, 183 (2000), nucl-th/9909014.

[29] L. D. Landau, Izv. Akad. Nauk Ser. Fiz **17**, 51 (1953).

[30] L. D. Landau and E. M. Lifshitz, *Fluid Mechanics* (Pergamon Press, Oxford, 1959).

[31] E. V. Shuryak, Prog. Part. Nucl. Phys. **53**, 273 (2004).

[32] K. Paech, H. Stöker, and A. Dumitru, Phys.Rev. **C68**, 044907 (2003).

[33] H. Sorge, Phys. Lett. **B402**, 251 (1997), nucl-th/9701012.

[34] H. Sorge, Phys. Rev. Lett. **82**, 2048 (1999), nucl-th/9812057.

[35] H. Sorge, Phys. Rev. **C52**, 3291 (1995), nucl-th/9509007.

[36] H. A. Gustafson *et al.*, Phys. Rev. Lett. **52**, 1590 (1984).

[37] P. Danielewicz and G. Odyniec, Phys. Lett. **B157**, 146 (1985).

[38] J.-Y. Ollitrault, Phys. Rev. **D48**, 1132 (1993), hep-ph/9303247.

[39] E877, J. Barrette *et al.*, Phys. Rev. Lett. **73**, 2532 (1994), hep-ex/9405003.

[40] S. A. Voloshin and Y. Zhang, Z. Phys. **C70**, 665 (1996), hep-ph/9407282.

[41] A. M. Poskanzer and S. A. Voloshin, Phys. Rev. **C58**, 1671 (1998), nucl-ex/9805001.

[42] J.-Y. Ollitrault, (1997), nucl-ex/9711003.

[43] S. Wang *et al.*, Phys. Rev. **C44**, 1091 (1991).

[44] N. Borghini, P. M. Dinh, and J.-Y. Ollitrault, Phys. Rev. **C63**, 054906 (2001), nucl-th/0007063.

[45] N. Borghini, P. M. Dinh, and J.-Y. Ollitrault, Phys. Rev. **C64**, 054901 (2001), nucl-th/0105040.

[46] R. S. Bhalerao, N. Borghini, and J.-Y. Ollitrault, nucl-th/0307018.

[47] N. Borghini, R. S. Bhalerao, and J.-Y. Ollitrault, nucl-th/0402053.

[48] FOPI, A. Andronic *et al.*, Nucl. Phys. **A679**, 765 (2001), nucl-ex/0008007.

[49] STAR, K. H. Ackermann *et al.*, Phys. Rev. Lett. **86**, 402 (2001), nucl-ex/0009011.

[50] C. A. Ogilvie *et al.*, Phys. Rev. **C40**, 2592 (1989).

[51] J. Milošević and L. Simić, (*Proceedings of the Conference: Bologna 2000, Structure of the Nucleus at the dawn of the Century*) , 145 (2000).

[52] E877, J. Barrette *et al.*, Phys. Rev. **C56**, 3254 (1997), nucl-ex/9707002.

[53] E877, J. Barrette *et al.*, Phys. Rev. **C55**, 1420 (1997).

[54] Streamer Chamber, P. Danielewicz, Phys. Rev. **C38**, 120 (1988).

[55] NA49, H. Appelshäuser *et al.*, Phys. Rev. Lett. **80**, 4136 (1998).

[56] R. A. Lacey *et al.*, Phys. Rev. Lett. **70**, 1224 (1993).

[57] N. Borghini, P. M. Dinh, and J.-Y. Ollitrault, Phys. Rev. **C62**, 034902 (2000), nucl-th/0004026.

[58] P. M. Dinh, N. Borghini, and J.-Y. Ollitrault, Phys. Lett. **B477**, 51 (2000), nucl-th/9912013.

[59] FOPI, N. Bastid *et al.*, Phys. Rev. **C72**, 011901 (2005), nucl-ex/0504002.

[60] CERES, T. Ullrich *et al.*, Nucl. Phys. **A610**, 317c (1996).

[61] CERES, D. Adamova *et al.*, (2005), nucl-ex/0512007.

[62] CERES, G. Agakichiev *et al.*, JINR Rapid. Comm. **3**, 83 (1997).

[63] E. Gatti and P. Rehak, Nucl. Instrum. Meth. **A225**, 608 (1984).

[64] O. Nix, *Diploma thesis* (University of Heidelberg, Germany, 1996).

[65] J. Seguinot and T. Ypsilantis, Nucl. Instr. and Meth. **142**, 377 (1977).

[66] CERES, I. Tserruya, Nucl. Phys. **A553**, 857c (1993).

[67] CERES, R. Baur *et al.*, Nucl. Instrum. Meth. **A343**, 87 (1994).

[68] CERES, R. Baur *et al.*, Nucl. Instrum. Meth. **A355**, 329 (1995).

[69] CERES, A. Marín, J. Phys. **G30**, S709 (2004), nucl-ex/0406007.

[70] (Particle Data Group), S. Eidelman *et al.*, Phys. Lett. **B592**, 1 (2004).

[71] A. Wörner, *Diploma thesis* (University of Heidelberg, Germany, 1990).

[72] W. Blum and W. Rolandi, *Particle Detection with Drift Chambers* (Springer-Verlag, Heidelberg, 1994).

[73] R. K. Bock *et al.*, *Data Analysis Techniques for High-Energy Physics Experiments* (Cambridge University Press, Cambridge, 1995).

[74] CERES, D. Miśkowiec, Private Communication (2005).

[75] L. Ray, Private Communication (2005).

[76] R. L. Ray and R. S. Longacre, STAR Note **419**.

[77] CERES, H. Appelshäuser *et al.*, Nucl. Phys. **A698**, 253c (2002).

[78] NA49, C. Alt *et al.*, nucl-ex/0303001.

[79] CERES, H. Tilsner, *Doctoral thesis* (University of Heidelberg, Germany, 2002).

[80] STAR, C. Adler *et al.*, Phys. Rev. Lett. **87**, 182301 (2001), nucl-ex/0107003.

[81] W. Reisdorf and H. G. Ritter, Ann. Rev. Nucl. Part. Sci. **47**, 663 (1997).

[82] N. Herrmann, J. P. Wessels, and T. Wienold, Ann. Rev. Nucl. Part. Sci. **49**, 581 (1999).

[83] EOS, S. Wang *et al.*, Phys. Rev. Lett. **76**, 3911 (1996).

[84] FOPI, J. L. Ritman *et al.*, Z. Phys. **A352**, 355 (1995), nucl-ex/9506002.

[85] FOPI, P. Crochet *et al.*, Phys. Lett. **B486**, 6 (2000), nucl-ex/0006004.

[86] KaoS, Y. Shin *et al.*, Phys. Rev. Lett. **81**, 1576 (1998), nucl-ex/9807003.

[87] E895, P. Chung *et al.*, Phys. Rev. Lett. **85**, 940 (2000), nucl-ex/0101003.

[88] P. Chung *et al.*, Phys. Rev. Lett. **86**, 2533 (2001), nucl-ex/0101002.

[89] STAR, J. Adams *et al.*, (2005), nucl-ex/0504022.

[90] NA44, I. G. Bearden *et al.*, Phys. Rev. Lett. **78**, 2080 (1997).

[91] E. Andersen *et al.*, Phys. Lett. **B433**, 209 (1998).

[92] STAR, K. H. Ackermann *et al.*, Nucl. Phys. **A661**, 681 (1999).

[93] G. E. Brown *et al.*, Phys. Lett. **B253**, 19 (1991).

[94] J. Podolanski and R. Armenteros, Phil. Mag. **45**, 13 (1954).

[95] P. F. Kolb, P. Huovinen, U. W. Heinz, and H. Heiselberg, Phys. Lett. **B500**, 232 (2001).

[96] P. Huovinen, Private Communication (2005).

[97] P. F. Kolb, J. Sollfrank, and U. W. Heinz, Phys. Let. **B459**, 667 (1999), nucl-th/9906003.

[98] CERES, G. Agakichiev *et al.*, Phys. Rev. Lett. **92**, 032301 (2004).

[99] CERES, J. Bielčíková, *Doctoral thesis* (Karls University, Prague, 2003).

[100] D. Teaney, J. Lauret, and E. V. Shuryak, (2001), nucl-th/0110037.

[101] D. Teaney, (2002), nucl-th/0204023.

[102] NA49, G. Stefanek, Nucl. Phys. **A**, in print (2005), nucl-ex/0510067.

[103] NA49, G. Stefanek, Private Communication (2005).

[104] STAR, M. Oldenburg, J. Phys. **G31**, S437 (2005), nucl-ex/0412001.

[105] D. Molnar and S. A. Voloshin, Phys. Rev. Lett. **91**, 092301 (2003).

[106] PHENIX, S. S. Adler *et al.*, Phys. Rev. Lett. **91**, 172301 (2003).

[107] STAR, J. Adams *et al.*, Phys. Rev. Lett. **92**, 052302 (2004).

[108] V. Greco and C. M. Ko, Phys. Rev. **C70**, 024901 (2004).

[109] X. Dong *et al.*, Phys. Lett. **B597**, 328 (2004).

[110] T. Csőrgő *et al.*, Phys. Rev. **C67**, 034904 (2003).

[111] M. Csanád, T. Csőrgő, and B. Lőrstad, Nucl. Phys. **A742**, 80 (2004).

[112] PHENIX, A. Taranenko, nucl-ex/050619.